Czech Technical University in Prague

Faculty of Mechanical Engineering

Department of Aerospace Engineering

Rudder Design of Racing Airplane

Master's Thesis

Bc. Michal Coufal

Programme: Aerospace Engineering

Specialization: Aircraft and UASs

Supervisor: Ing. Karel Barák

2024

ZADÁNÍ DIPLOMOVÉ PRÁCE

I. OSOBNÍ A STUDIJNÍ ÚDAJE

Příjmení: **Coufal** Jméno: **Michal** Osobní číslo: **483243**

Fakulta/ústav: **Fakulta strojní**

Zadávající katedra/ústav: **Ústav letadlové techniky**

Studijní program: **Dopravní a transportní technika**

Specializace: **Motorová vozidla**

II. ÚDAJE K DIPLOMOVÉ PRÁCI

Název diplomové práce:

Návrh směrového kormidla rychlostního letounu.

Název diplomové práce anglicky:

Rudder design of racing airplane.

Pokyny pro vypracování:

Tématem práce je konstrukční návrh směrového kormidla na základě dodané geometrie. Stanovení zatížení včetně ostruhového kolečka. Provedení pevnostní kontroly navržené konstrukce a návrhu výrobní technologie.

Seznam doporučené literatury:

Dle pokynů vedoucího.

Jméno a pracoviště vedoucí(ho) diplomové práce:

Ing. Karel Barák ústav letadlové techniky FS

Jméno a pracoviště druhé(ho) vedoucí(ho) nebo konzultanta(ky) diplomové práce:

Datum zadání diplomové práce: **26.04.2024** Termín odevzdání diplomové práce: **24.05.2024**

Platnost zadání diplomové práce: _____

Ing. Karel Barák podpis vedoucí(ho) práce	Ing. Milan Dvořák, Ph.D. podpis vedoucí(ho) ústavu/katedry	doc. Ing. Miroslav Španiel, CSc. podpis děkana(ky)

III. PŘEVZETÍ ZADÁNÍ

Diplomant bere na vědomí, že je povinen vypracovat diplomovou práci samostatně, bez cizí pomoci, s výjimkou poskytnutých konzultací. Seznam použité literatury, jiných pramenů a jmen konzultantů je třeba uvést v diplomové práci.

. _____ Datum převzetí zadání

_____ Podpis studenta

Declaration

I declare that I have independently prepared my diploma thesis and have used only the sources (literature, projects, software, etc.) listed in the attached bibliography.

I have no serious objection to the use of this academic work as per § 60 of Law no.121/2000 Sb., on Copyright, rights related to copyright, and on the amendment of certain laws (copyright law).

In Prague on: ....

Signature

Acknowledgment

I would like to express my deepest gratitude to my thesis advisor, Ing. Karel Barák, for his guidance and support throughout the entire process of this thesis. I am also thankful to Ing. Jiří Brabec, Ph.D., and Ing. Jakub Valenta, for providing invaluable advice when needed, and to the entire Department of Aerospace Engineering for providing the necessary resources and facilities for the successful completion of this thesis.

Special thanks to my family for their unwavering support and encouragement during this academic journey. Lastly, I thank all my friends for their encouragement and understanding over the past year.

Annotation sheet

Author:	Michal Coufal	
Title of master's thesis:	Rudder Design of Racing Airplane	
Academic year:	2024	
University:	Czech Technical University in Prague Faculty of Mechanical Engineering	
Department:	Department of Aerospace Engineering	
Study programme:	N0716A270010 - Aerospace Engineering	
Specialization:	N071TLBS - Aircraft and UASs	
Supervisor:	Ing. Karel Barák	
Extent:	Number of pages: Number of figures: Number of tables: Number of attachments:	111 93 22 2
Keywords:	Racing airplane, rudder, structural design, composite materials, CLT, FEA, production process	

Abstract

The objective of this thesis is to design a rudder for a racing airplane. The thesis begins with a brief overview of fiber-reinforced polymers. Subsequently, loads acting on the rudder are determined, and its structure is designed using analytical methods. The strength of the designed structure is then verified by finite element analysis, and a 3D model is created after implementing the necessary layup changes. The thesis concludes with a summary of the production process and a mass analysis.

Anotační list

Autor:	Michal Coufal	
Název diplomové práce:	Návrh směrového kormidla rychlostního letounu	
Rok vyhotovení:	2024	
Univerzita:	České vysoké učení technické v Praze Fakulta strojní	
Ústav:	Ústav letadlové techniky	
Studijní program:	N0716A270010 - Letectví a kosmonautika	
Specializace:	N071TLBS - Letadla a bezpilotní systémy	
Vedoucí diplomové práce:	Ing. Karel Barák	
Bibliografické údaje:	Počet stran: Počet obrázků a grafů: Počet tabulek: Počet příloh:	111 93 22 2
Klíčová slova	Rychlostní letoun, směrové kormidlo, konstrukční návrh, kompozitní materiály, CLT, MKP, výrobní technologie	

Anotace

Cílem této diplomové práce je návrh směrového kormidlo rychlostního letounu. Práce začíná stručným přehledem vláknových kompozitů s polymerní matricí. Následně jsou určena zatížení, která na směrové kormidlo působí, a jeho konstrukce je navržena pomocí analytických výpočtů. Pevnost navržené konstrukce je poté ověřena analýzou pomocí metody konečných prvků a po provedení nezbytných změn ve skladbě laminátů je vytvořen 3D model. Práce je zakončena popisem výrobního postupu a hmotnostní analýzou.

Contents

List of Figures

List of Tables

Used Software

Microsoft Excel
www.overleaf.com (LaTeX)
PyCharm Community Edition 2021.3.2
eLAMX^2 *version 2.6*
Autodesk Inventor Professional 2021
Siemens NX *version 2212*

Attachments

Attachment 1: 3D model and FEA files
Attachment 2: Python scripts

Abbreviations

AR	Aspect Ratio
CG	Center of Gravity
CFRP	Carbon Fiber Reinforced Polymer
CLT	Classical Laminate Theory
FAI	World Air Sports Federation (*Fédération Aéronautique Internationale*)
FEA	Finite Element Analysis
FRP	Fiber Reinforced Polymer
ISA	International Standard Atmosphere
LCM	Liquid Composite Molding
MAC	Mean Aerodynamic Chord
MTOM	Maximum Take-Off Mass
PMC	Polymer Matrix Composite
RTM	Resin Transfer Molding
UD	Unidirectional
VT	Vertical Tail

Nomenclature

a	$[m]$	Dimension, defined where applied
a_{VT}	$[rad^{-1}]$	Lift curve slope of VT
A	$[m^2]$	Wing area
A_C	$[m^2]$	Rudder's cell area
A_{VT}	$[m^2]$	VT area
$\mathbf{ABD}$	$[-]$	ABD matrix
b	$[m]$	Dimension, defined where applied
b_{ef}	$[m]$	Effective skin width
b_{VT}	$[m]$	Chord dimension of VT
b_{web}	$[m]$	Width of web
c	$[m]$	Distance between main landing gear and tail wheel
$c_{l\alpha}$	$[rad^{-1}]$	Airfoil lift curve slope
e	$[m]$	Location of shear center
E_1, E_2	$[GPa]$	Tensile modulus
F_T	$[N]$	Ground reaction acting on the tail wheel
g	$[m/s^{-2}]$	Gravitational acceleration ($9.81\ m/s^{-2}$)
G_{12}	$[GPa]$	Shear modulus
G_c	$[GPa]$	Shear modulus of core
G_s, G_w	$[GPa]$	Shear moduli of skin and web
h_{ef}	$[m]$	Effective spar height
h_s, h_w	$[m]$	Thickness of skin's and web's laminate
i_y	$[m]$	Radius of inertia of the airplane
k	$[-]$	Ratio of 2-dimensional lift curve slope to 2π
k_{VT}	$[-]$	Gust alleviation factor
l	$[m]$	Distance between hinges

M_t	$[Nm]$	Torsional moment
$M_T^{E.A.}$	$[Nm]$	Torsional moment around elastic axis
$M_T^{R.A.}$	$[Nm]$	Torsional moment around rotational axis
M_x, M_y, M_z	$[N]$	Moment resultants
n_k	$[-]$	Limit load factor on the airplane's wheels
n_{pr}	$[-]$	Limit load factor in the airplane's CG
N_{bc}	$[N/m]$	Compressive buckling load of simply supported plate
N_{bs}	$[N/m]$	Shear buckling load of long plate
N_{bs}^0	$[N/m]$	Shear buckling load of infinite plate
$N_{bs}^{0.5-2}$	$[N/m]$	Shear buckling load of rectangular plate
N_x, N_y, N_z	$[N/m]$	Force resultants
N_{xcrim}	$[N/m]$	Crimping load under compression
N_{xycrim}	$[N/m]$	Crimping load under shear
N_{xcrit}	$[N/m]$	Compressive buckling load with transverse shear effect
N_{xycrit}	$[N/m]$	Shear buckling load with transverse shear effect
N_{xwr}^a	$[N/m]$	Anti-symmetric wrinkling load
N_{xwr}^s	$[N/m]$	Symmetric wrinkling load
P	$[N]$	Reaction on the tail wheel
P_s^m	$[N]$	Bolt's ultimate shear load
P_{st}	$[N]$	Tail wheel static load
P_{tot}	$[N]$	Total reaction on the tail wheel for the side load case
P_{VT}	$[N]$	Total load on the VT for gust
q_g	$[N/m]$	Distributed load for the gust case
q_m	$[N/m]$	Distributed load for the maneuver case
$q_{M_T^{E.A.}}$	$[Nm]$	Shear flow from torsional moment
$\mathbf{Q}$	$[-]$	Stiffness matrix in principal coordinate system
$\mathbf{Q}'$	$[-]$	Stiffness matrix in global coordinate system
Q_{m_u}	$[N]$	Total force developed by the distributed load
r	$[J \cdot kg^{-1} \cdot K^{-1}]$	Specific gas constant for air $(287\ J \cdot kg^{-1} \cdot K^{-1})$
R_h	$[N]$	Reactions in hinges
R_t	$[N]$	Reaction in the rudder cable attachment
S	$[N]$	Shear force
S^f	$[MPa]$	Failure shear strength
S_A^{min}	$[mm^2]$	Minimum adhesive surface
t	$[mm]$	Ply thickness
t_c	$[mm]$	Core thickness
T	$[K]$	ISA sea level temperature $(288.15\ K)$
$\mathbf{T}_\sigma, \mathbf{T}_\varepsilon$	$[-]$	Transformational matrices
U	$[m/s]$	Gust velocity
v_f	$[\%]$	Fiber volume fraction
V	$[m/s]$	flight velocity
V_B	$[m/s]$	Design rough air speed
V_D	$[m/s]$	Design diving speed
V_s	$[N]$	Vertical load carried by skin
V_w	$[N]$	Vertical load carried by web
w_a	$[m/s]$	Areal weight of lamina
ws	$[m/s]$	Descent velocity
W_g	$[Pa]$	Pressure parameter for gust load chordwise distribution

W_m	$[Pa]$	Maneuvre load pressure parameter
$\overline{W_g}$	$[Pa]$	Gust average pressure load on VT
$\overline{W_m}$	$[Pa]$	Maneuvre average pressure load on VT
$\overline{x_{cg}}$	$[\%]$	Aircraft CG position in % of MAC
x_{q_g}	$[m]$	Gust point force chordwise location
x_{q_m}	$[m]$	Maneuvre point force chordwise location
$X^t,\ X^c$	$[MPa]$	Failure tensile and compressive stress along fibers
y_T	$[m]$	Total landing gear dampening path
y_{PN}	$[m]$	Tire deformation
y_{TL}	$[m]$	Dampening member deformation
$Y^t,\ Y^c$	$[MPa]$	Transverse failure tensile and compressive stress
x	$[m]$	Longitudinal axis coordinate
y	$[m]$	Transverse axis coordinate
z	$[m]$	Vertical axis coordinate
z_c	$[m]$	Active portion of core
β	$[-]$	Mach number parameter
γ_{xy}	$[-]$	Shear strain in xy plane
γ_{xyu}	$[-]$	Ultimate shear strain in xy plane
$\varepsilon_x,\ \varepsilon_y$	$[-]$	Strain in x and y directions
$\varepsilon_x^0, \varepsilon_y^0, \varepsilon_s^0$	$[-]$	Membrane strains
$\varepsilon_{xu}^t,\ \varepsilon_{xu}^c,\ \varepsilon_{yu}^t,\ \varepsilon_{yu}^c$	$[-]$	Ultimate tensile and compressive strain
θ	$[^\circ]$	Ply angle
κ	$[-]$	Isentropic expansion factor of air (1.4)
$\kappa_x, \kappa_y, \kappa_s$	$[-]$	Laminate curvatures
Λ_C	$[rad]$	Sweepback of VT mid-chord
μ	$[rad]$	Lateral mass ratio
ν_{12}	$[-]$	Poisson's ration
ρ	$[kg/m^3]$	Density
ρ_0	$[kg/m^3]$	Air density at sea level $(1.225\ kg/m^3)$
$\sigma_{bearing}$	$[MPa]$	Bearing stress
$\sigma_c^u,\ \sigma_S^u,\ \sigma_u^u$	$[MPa]$	Ultimate compressive, shear, and tensile strength
$\sigma_{net-tension}$	$[MPa]$	Net-tension stress
$\sigma_{shearout}$	$[MPa]$	Shearout stress
σ_t^y,	$[MPa]$	Yield tensile strength
$\sigma_{wtsplitt}$	$[MPa]$	Wedge-type splitting stress
$\sigma_x,\ \sigma_y,\ \sigma_z$	$[MPa]$	Stres in x, y, and z directions
τ_{xy}	$[MPa]$	Shear stress in xy plane

1 Introduction

In 2019, Ing. Jakub Valenta presented a conceptual design for a racing airplane in his master's thesis. It was soon decided to proceed with his design, leading to the development of numerous subsequent theses on various aspects of the airplane's design. This thesis contributes to advancing to the airplane's production stage.

The objective of this thesis is to design the airplane's rudder. This includes determining the loads the rudder is subjected to, performing the structural design, and verifying the structure's strength. Production technology must also be considered to ensure the rudder's manufacturability.

A brief description of the airplane and the current stage of its design, including the rudder, is provided in Section 2 to give context for this thesis. Section 3 offers an overview of fiber-reinforced polymers, their manufacturing technology, and some of the most widely used failure criteria. The selection of materials is detailed in Section 4, where carbon fiber reinforcements, Rohacell foam core, and AISI 4140 steel are chosen for the design. It was decided to design the rudder for both prepreg and hand-wetted composite materials, which differ in fiber volume content and required safety factor, to determine if significant weight savings can be achieved by using prepreg.

The rudder is subjected to aerodynamic, ground, and control loads. The exact load cases that must be considered for the design and the magnitudes of these loads are presented in Section 5. Preliminary design is performed using analytical calculations in Section 6. Classical laminate theory and equations specific to composite materials and sandwich structures are used to determine the shape of the rudder's components and their layup. The use of pre-impregnated carbon fiber reinforcements does not yield the expected weight savings; therefore, it is decided to proceed only with the hand-wetted design to keep manufacturing costs down. The layups are then used to provide a baseline for the finite element analysis conducted in Section 7. Two-dimensional thin shell elements are used for the rudder's discretization as they best capture the behavior of thin structures. After the design's verification by FEA and the implementation of necessary layup changes, the 3D model is presented in Section 8. A brief summary of the production process follows in Section 9, detailing the vacuum bag molding process used for all the composite parts. The thesis concludes with a mass analysis in Section 10 to determine the expected mass of the rudder.

2 Preceding works on the airplane's and rudder's design

The conceptual design of the airplane in question (in Figure 1) was done in the master's thesis of Jakub Valenta [1] in 2019. The airplane was designed to break speed records in FAI C-1a/o (under 300 kg take-off mass) and C-1a (under 500 kg take-off mass) categories and it will be built under the UL 2 regulation [2] by the Light Aircraft Association of the Czech Republic. The airplane is of mid-wing configuration with a conventional tail, and a full-composite structure is anticipated from the very beginning of the design, giving the expected maximum take-off mass of 345 kg. [1]

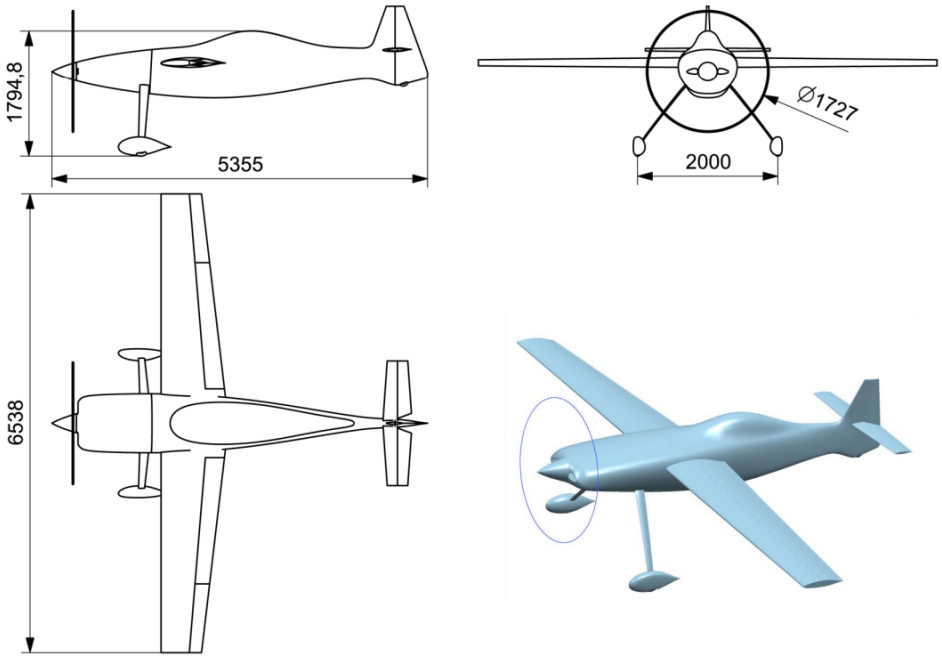

Figure 1: Drawing of the airplane [1]

Since the conceptual design, many other theses have been written concerning the mechanical design of major structures and systems, and the aerodynamic optimization using computer fluid dynamics. The structural design of the rudder was initially made by Jiří Němec in his bachelor's thesis [3], and it was slightly modified in the bachelor's thesis of Jan Procházka [4], the modified design is captured in Figure 2.

The modified design consists of a carbon fiber composite C-spar, root and tip ribs, skin, and an insert for the tail wheel. The flanges of the spar are made from unidirectional carbon fibers, whereas the web is made from a woven prepreg fabric with a plywood insert in place of the upper fitting. The ribs are made from the same prepreg fabric, the tip rib is integrated into the skin to save weight, and the lower fitting is connected to the root rib, which is strengthened by a plywood insert in the joint location. The ribs, the spar, and the skin stiffened by a foam core create a closed section that carries shear loads. In the root part of the rudder, the insert

for the tail wheel fitting is glued to the root rib and the spar, this design does not enable tail wheel change. [3, 4]

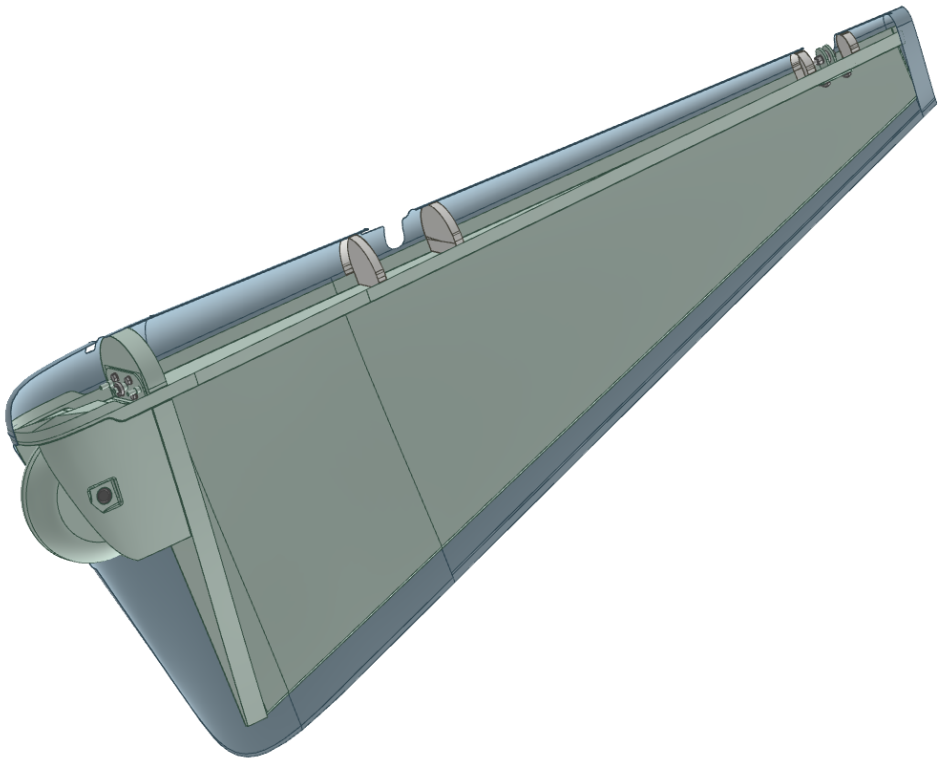

Figure 2: Modified rudder design

Very simplified calculations were used in the previous works to design the rudder. Therefore, the structural design may be changed to satisfy the regulation's requirements and to make the rudder as light as possible. Still, the outer geometry and position of the connecting elements to the vertical stabilizer will be preserved.

3 Composite Materials

As stated in the previous section, the airplane is expected to have a fully composite structure. Therefore, fiber-reinforced polymers (FRPs) are used for the design. Fiber-reinforced polymer is a compound material consisting of reinforcement in the form of fibers and a polymeric matrix. The high-strength and high-modulus fibers are dispersed in the polymeric matrix that helps to distribute the load between fibers by shear stress and also participates in load sharing with the fibers. The main advantage of FRPs is their high specific strength and moduli, which leads to weight saving, and therefore to fuel savings and an increase in payload. Other advantages over aluminum and titanium alloys include corrosion resistance, high dampening, good fatigue properties, and a reduction in the number of components and fasteners. Additionally, the nonisotropic nature of the material allows to tailor properties in various directions. The disadvantage of composites is their higher brittleness compared to wrought metals, meaning they are more susceptible to impact damage. Other drawbacks include the limited shelf life of resin, or entire prepreg systems which must be stored under specific conditions, and the need for special equipment and procedures for the repairs of composite parts. [5, 6, 7]

3.1 Fibers

Fibers are the principal load-carrying member in FRPs, the typical fiber volume fraction for high-performance continuous fiber composites is 45-65%. The filamentary form of material means there are statistically fewer surface flaws and their distance is greater than in the bulk form of material, leading to their high tensile strength. The strain is nearly linear until failure which, together with the high modulus of elasticity, leads to a very low failure strain. This brittleness means the fibers are prone to damage during handling, and their tensile strength exhibits a large amount of scatter. The most common fibers used in the aerospace industry are glass, carbon, and aramid fibers, these fibers are discussed in more detail. The properties of selected fibers are to be seen in Figure 3. [5, 7]

3.1.1 Glass Fibers

There are several types of glass fibers. The most common ones for structural applications are E-glass and S-glass, with an average density of 2.55 g/cm^3. E-glass fibers are the least expensive commercially available fibers, however, they still offer high strength, making them the most used fibers in polymer matrix composites. The S-glass fibers offer higher tensile modulus and strength, but are more expensive. Glass fibers are isotropic, and they have high elongation at break compared to other fiber types. Composites made from glass fibers are translucent, which enables easy defect and delamination detection during use. As shown in

Fiber	Filament Diameter (μm)	Density (g/cm³)	Tensile Modulus (GPa)	Tensile Strength (MPa)	Strain at Failure (%)
E-glass	10	2.54	72.4	3450	4.8
S-glass	10	2.49	86.9	4300	5
T-300 (PAN carbon)	7	1.76	230	3650	1.5
AS-4 (PAN carbon)	7.1	1.79	231	4410	1.7
IM-7 (PAN carbon)	5.2	1.78	276	5516	1.9
M-55J (PAN carbon)	–	1.91	540	4020	0.8
P120 (pitch carbon)	–	2.16	823	2200	0.3
Kevlar 49 (aramid)	11.9	1.45	131	3620	2.8

Figure 3: Properties of selected fibers used in FRPs [5]

Figure 4 the fibers have a low coefficient of thermal expansion and low electrical conductivity compared to metals, making them very good insulators. The disadvantages of glass fibers are their tendency to creep well below 200°C, decreased strength due to moisture absorption, and static fatigue, meaning that substantial crack growth can be observed under continuous load for an extended period of time. [5, 6, 7, 8]

Properties	Glass fibers	Steel	Aluminum
Tensile strength long. [MPa]	2400-4900	300-1300	200-530
Tensile strength trans.[MPa]	≈ 2000-4000	300-1300	200-530
Tensile modulus long. [GPa]	70-88	180-212	68-78
Tensile modulus trans. [GPa]	≈ 70-80	180-212	68-78
Elongation at break [%]	4,8-5,7	5-40	2-30
Density [g/cm³]	2,46-2,72	7,85-8,10	2,66-2,85
Coefficient of thermal expansion [K⁻¹]	$4{,}0\cdot10^{-6}$ - $6{,}5\cdot10^{-6}$	$9{,}4\cdot10^{-6}$ - $16{,}1\cdot10^{-6}$	$22{,}9\cdot10^{-6}$ - $24{,}2\cdot10^{-6}$
Electrical conductivity [S/m]	$\approx 10^{-13}$	$1{,}4\cdot10^{6}$ - $10\cdot10^{6}$	$12\cdot10^{6}$ - $37\cdot10^{6}$
Poisson ratio [-]	0,21-0,23	0,27-0,3	0,32-0,36
Effective heat capacity [J/gK]	0,72-0,8	0,456 - 0,472	0,9-1,0

Figure 4: Comparison of properties of glass fibers, steel, and aluminum [8]

3.1.2 Carbon Fibers

Carbon fibers are mostly manufactured from either polyacrylonitrile (PAN) or pitch precursors. The oxidation, carbonization, and eventually graphitization for high-modulus fibers, are processes needed for carbon fiber manufacturing which demand high energy input, making carbon fibers more expensive than glass fibers. As shown in Figure 5, depending on the fiber type, the tensile strength can be between 1000 and 7000 MPa, and the tensile modulus can be in the range of 150 to 950 GPa. Carbon fibers have a low density of 1.75 - 2 g/cm^3 and are not isotropic - they can be described as amorphous carbon with graphite crystal reinforcements.

The failure strain of the carbon fibers is lower than the failure strain of the glass fibers and their stiffness increases at higher stress. Carbon fibers have an extremely low creep tendency, they are good thermal insulators and are electrically conductive. The coefficient of thermal expansion is negative in the longitudinal direction of the fibers. The main disadvantages of carbon fibers are their high price, relatively low impact resistance, and their susceptibility to lightning damage and galvanic corrosion. [5, 6, 7, 8]

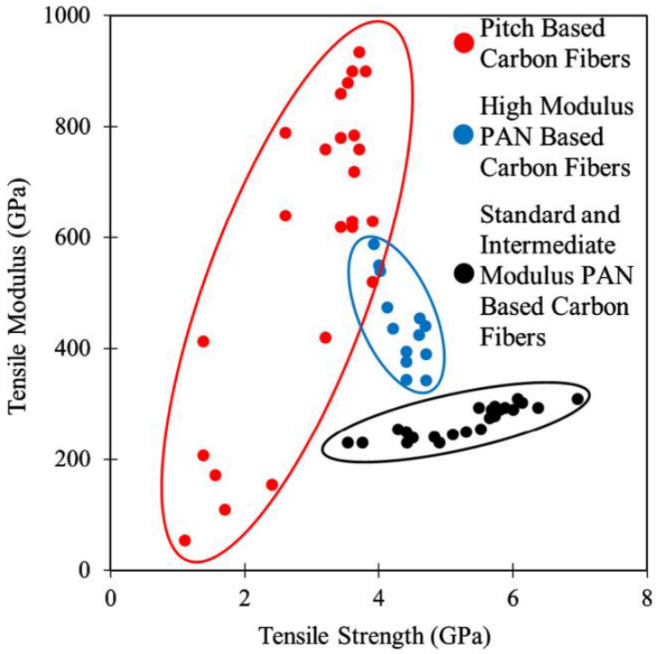

Figure 5: Tensile strength and modulus of carbon fibers [9]

3.1.3 Aramid Fibers

Aramid fibers are highly crystalline aromatic polyamide fibers. Depending on the positions carbon atoms are linked to on the aromatic ring, there are two main groups of aramids - para-aramids and meta-aramids. Meta-aramid fibers usually reach only one-fifth of the tensile strength and one-tenth of the tensile stiffness of para-aramid fibers as shown in Figure 6. Aramid fibers have the lowest density among the current reinforcing fibers and they have very high specific tensile strength. A major advantage of aramid fibers is their high energy absorption during fracture owing to their high failure strain and ability to undergo plastic deformation in compression. They also offer very high resistance to crack propagation, but the compressive strength of aramid fibers is low, and they tend to absorb moisture. Aramid fibers are also difficult to machine given their high cutting resistance and are prone to short-term creep, whereas their long-term creep is negligible. The aramid polymer-matrix composites are mostly used in fairings, skins, or face sheets for honeycomb panels. [5, 6, 7, 8, 10]

	Kevlar 49	Kevlar 129	Twaron HS-2000	Twaron HM-2200	Teijinconex
Aramid Type	para-Aramid	para-Aramid	para-Aramid	para-Aramid	meta-Aramid
Density [g/cm³]	1,45	1,45	1,44	1,45	1,37-1,38
Tensile strength [MPa]	2900	3400	3800	3200	620-690
Tensile modulus [GPa]	135	99	90	120	7,9-9,8
Tensile elongation at break [%]	2,8	3,3	3,5	2,7	35-45
Compression strength [MPa]	700	-	-	-	
Compressive stiffness [GPa]	135	-	-	-	
Compressive elongation at break [%]	0,5	-	-	-	

Figure 6: Properties of aramid fibers [8]

3.1.4 Fiber Architecture

Fiber architecture, in other words, an arrangement of fibers, has a strong impact on the properties, performance, and failure behavior of polymer matrix composites. From the manufacturing standpoint, the conformability of the fibers to the mold, fiber movement during resin infusion, and the permeability of the selected architecture play a vital role in the fiber architecture selection. The fiber architecture can be linear (tapes), 2D (various types of fabrics), or 3D (three-dimensional textile preforms). [5]

Strand, Roving, Tow, Yarn

A strand is a term used in the glass fiber industry and it's used to describe a bundle of parallel continuous filaments. Roving is also used in the glass fiber industry to describe a bundle of parallel continuous filaments or strands with little or no twist. In the carbon and aramid fiber industry, the term tow is used to describe a bundle of parallel continuous filaments. The number of filaments in the tow varies depending on the tow's further usage and it can range from 1000 to more than 50,000. The term yarn is used in all three fiber industries and describes a twisted bundle of filaments. The twist helps to hold the fibers together and to ensure an even tension during ensuing processes. The fiber forms are depicted in Figure 7. [5, 10]

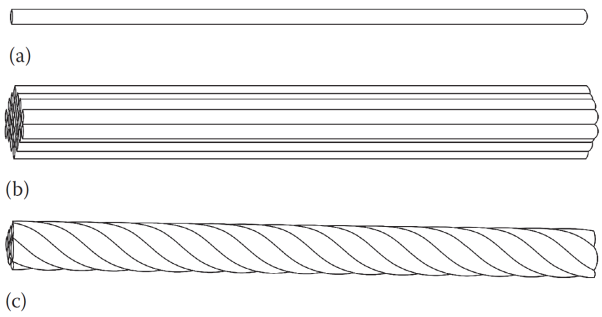

Figure 7: Fiber forms: (a) filament, (b) roving or tow, (c) yarn [5]

Linear Fibre Architecture

Linear fiber architecture means that all the fibers are oriented in the same direction. To ensure that the fibers hold together, they can be stitched, bonded by a matrix, or bonded to a supporting cloth. The advantages of unidirectional fibers are the maximal utilization of their tensile and compressive strengths and modulus as there are no undulations, and higher achievable fiber volume content than with 2D architecture. The unidirectional fibers also enable the highest degree of properties tailoring in desired directions when multiple layers are stacked together. The disadvantages of unidirectional fibers when compared to fabrics are their inferior transverse properties and more difficult handling during the fabrication process. [5, 10]

Woven Fabrics

Woven fabrics are made using conventional weaving looms. The fibers that run in the length direction are called warp fibers and the fibers running perpendicular to them are called weft or fill fibers. The hybrid woven fabrics where the warp and weft fibers are different (for example carbon fiber weft and aramid fiber warp) are also available. The basic weave styles are plain weave, satin weave, twill weave, and basket weave. The weave pattern determines the draping characteristics, stability, porosity, and crimp of the fabric. The basic weave patterns and the comparison of their properties are shown in Figure 8. The plain weave has the highest interlacing density which prevents yarn slippage during handling and processing and the fiber movement is then really low. The satin and twill weaves have lower interlacing density and therefore are less stable during production. On the other hand, the lower interlacing density helps with the fabric drapeability so these weaving patterns are more suitable for contoured or complex surfaces and they also allow easier resin penetration. The lower amount of undulations also means higher strengths and moduli than the plain weave fabrics, as the undulations are the main cause of significant reinforcing efficiency loss compared to the unidirectional fibers. The other cause for the reinforcing efficiency loss is the lower achievable fiber volume fraction. The strength difference between the mentioned weave styles is negligible and the exact determination of strength properties would require extensive tests, therefore the same strength properties, which are given in Section 4, are used for all the weaving patterns. [5, 10]

Non-woven Fabrics

Non-woven fabrics, often called mats, contain randomly oriented continuous or chopped fibers, and their in-plane properties are isotropic. The manufacturing cost of mats is lower since the production rate can be higher. The mechanical properties of non-woven fabrics are much inferior to other fabrics but their drapeability is better, so the mats are suitable for low-performance complexly-shaped parts. [5]

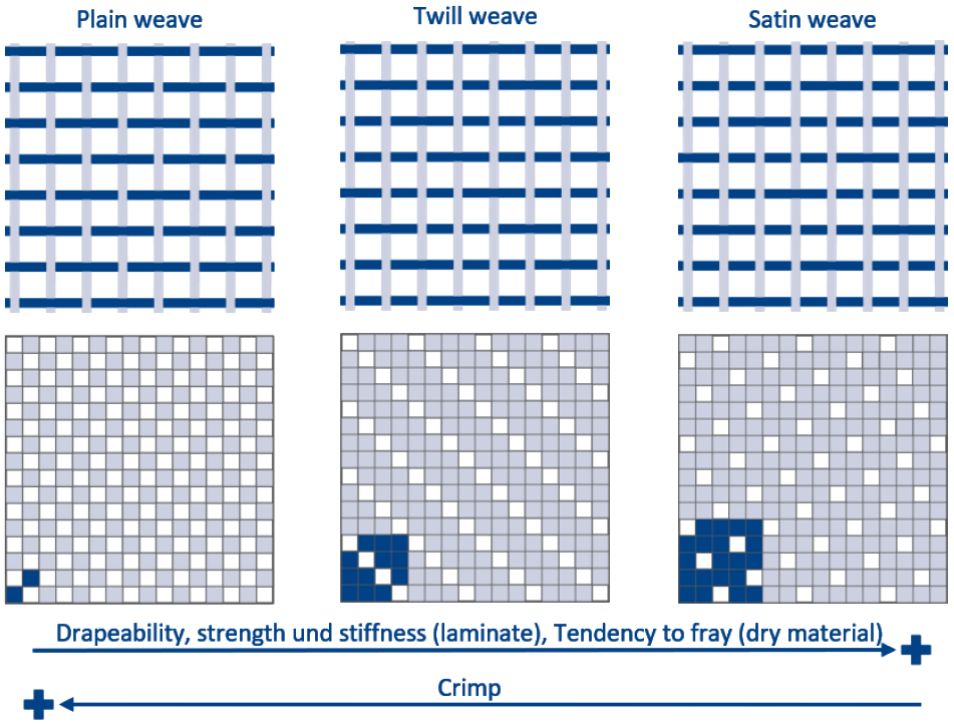

Figure 8: Basic types of woven fabrics [8]

Knitted and Braided Fabrics

Knitted fabrics (Figure 9 (a)) are made on a knitting machine similar to that used for making garments, where one or more yarns are interloped. Their drapeability is better than the drapeability of woven fabrics, but their strength is lower because of the high degree of yarn curvature. [5]

Braided fabrics (Figure 9 (b)) are made of two sets of continuous yarns which are symmetrically interwoven about the braiding axis. The manufacturing process is more complex, so they are generally more expensive than woven fabrics but their specific strength is usually higher and they are highly shear-resistant. Due to limitations in their production, the braided fabrics are much narrower than woven fabrics and are therefore used for local reinforcements or parts with small cross sections. [5, 10]

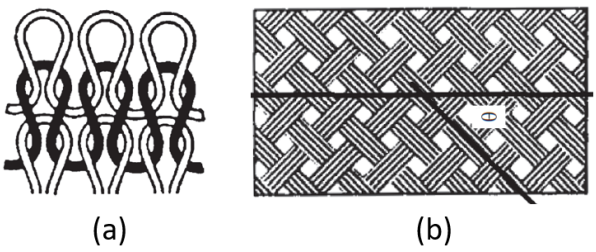

Figure 9: Knitted (a) and Braided (b) fabric [5]

Non-crimp Fabrics

Non-crimp fabrics are made of multiple layers of straight fibers that are either stitched together by no-load-carrying polymer fibers (Figure 10) or are held together by a network of thermoplastic binder. The fibers have nearly no undulations and crimp which makes the fabric's mechanical properties superior to the woven fabrics. The resin flow through the non-crimp fabric is also better than through the woven fabrics. The non-crimp fabrics are also very good for automation as the desired lay-up can be created during the fabric's manufacturing process, but their drapability significantly drops with increasing number of plies. [5, 10]

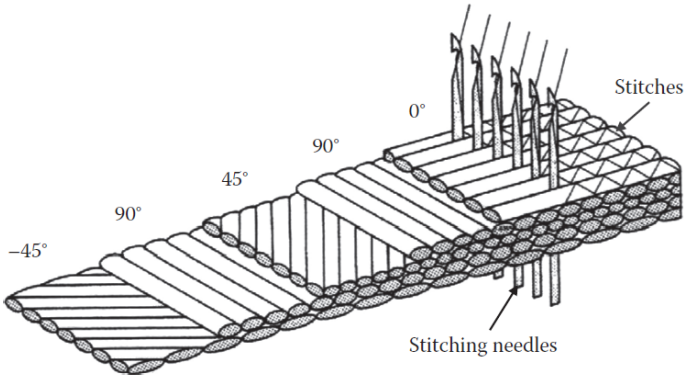

Figure 10: Stitched non-crimp fabric [5]

Three-dimensional Textile Preforms

In three-dimensional textile preforms, a portion of the fibers runs in the thickness direction of the fabric which improves the out-of-plane properties and reduces the possibility of failure by delamination. They can be manufactured using 5 methods - weaving, knitting, braiding, stitching, or z-pinning. In the z-pinning process, metal or composite pins are inserted through the fabric thickness. Generally, the in-plane properties of 3D preforms are lower compared to 2D preforms. [5]

3.2 Polymer Matrix

"A polymer is defined as a long-chain molecule containing one or more repeating units of atoms, joined together by strong covalent bonds. A polymeric material (commonly called a plastic) is a collection of a large number of polymer molecules of similar chemical structure (but not of equal length)." [7] Polymers are divided into two groups - thermosets and thermoplastics - depending on the chemical connection between molecules. The differences between the two and their properties are discussed in the following subsections. The purpose of the matrix is to transfer load between the fibers, keep them in place, and protect them from environmental effects such as moisture, UV light, or exposure to chemicals. The compressive and shear properties of a composite are hugely influenced by the matrix properties, which are dependent on the service temperature. The typical properties of selected polymers are summarized in

Figure 11. The selection of the matrix has a large influence on the manufacturing process of PMCs - its viscosity influences how well the fibers are wetted, and how well is the mold filled with resin expelling the air out of the mold so there are no voids in the finished part. The cure time, temperature, and pressure also have to be chosen with the specific resin in mind. [5, 7]

Polymer	Density (g/cm³)	Tensile Modulus (GPa)	Tensile Strength (MPa)	Strain at Failure (%)	Glass Transition Temperature, T_g (°C)	Maximum Service Temperature (°C)
			Thermosetting Polymers[a]			
Epoxies	1.2–1.3	2.75–4.1	55–130	1.5–8	150–260	125
Polyesters	1.1–1.4	2.1–3.5	35–104	1–7		60–150
Vinyl esters	1.12–1.32	3–3.5	73–81	3–8		60–150
Bismaleimides	1.2–1.32	3.2–3.5	48–110	1.5–3.3	230–290	232
Polyurethanes	1.21	0.7	30–40	400	120–167	
			Thermoplastic Polymers			
PEEK	1.30	3.7	110	25	143	260
PPS	1.35	3.45	93	15	85	218
Polyether-imide	1.28	3.45	117	60	210	171
Polyamide-imide	1.42	4.5	150	8	275	
PP	0.90	1.5	36	>100%	−10	50–75
Polyamide-6	1.13	3.10	80	50	60	

[a] Properties of thermosetting polymers are given in ranges, since they depend on the chemical structure of the polymer and the curing condition.

Figure 11: Properties of selected polymers [5]

3.2.1 Thermosets

In thermoset polymers, the molecules are chemically connected or cross-linked. Thermosets cannot be reprocessed using melting, but they soften and exhibit glass transition temperature, they cannot be directly recycled, and their shelf life is limited. Compared to thermoplastics, the processing time of thermosets is longer, therefore the production rate is lower than would be possible with thermoplastics. Thermosets are highly resistant to solvents and have higher heat resistance than thermoplastics. They also exhibit higher hardness and brittleness than thermoplastic polymers and are less prone to creep and stress relaxation. During production, very low viscosity can be achieved with thermoset polymers, resulting in good fiber wetting. They can be processed even at room temperature but at the price of a longer cure cycle and not optimal mechanical properties. To exploit the full potential of the thermoset matrix, a post-cure cycle at elevated temperature is needed. The most used

thermosets for PMCs are polyesters and epoxies. Epoxies are the most common matrix material for high-performance composites and their properties are discussed further. [5, 7, 10]

Epoxies

The molecular structure of epoxies is based on the epoxide group which creates a ring consisting of two atoms of carbon and one atom of oxygen. The epoxy matrix is a product of a chemical reaction of a low-molecular-weight prepolymer and a curing agent, also called a hardener. The function of the hardener is to co-react and join the epoxy molecules. The ratio of prepolymer and curing agent has to be measured accurately because the amount of hardener influences the properties of the cured matrix as opposed to the cure rate which is not affected. The curing reaction is usually initiated by heat application to the resin mix and the subsequent reaction is exothermic. With the continuation of the reaction, more epoxy molecules are cross-linked, forming a 3D network structure. The density of cross-links influences the properties of a cured resin; tensile modulus, glass transition temperature, and thermal and chemical stability increase with the increasing density while the failure strain and fracture toughness decrease. Other additives that can be used for epoxy matrix manufacturing are an accelerator which is used to speed up the reaction and reduce gel time, and a diluent that lowers the resin's viscosity which helps with the resin flow and fiber wetting. Elastomer particles or ductile thermoplastic polymer can be added to the resin mix to make the resin less brittle and therefore create a more damage-tolerant composite. [5, 7, 10, 11, 12]

Density (g/cm^3)	1.2–1.3
Tensile strength, MPa (psi)	55–130 (8,000–19,000)
Tensile modulus, GPa (10^6 psi)	2.75–4.10 (0.4–0.595)
Poisson's ratio	0.2–0.33
Coefficient of thermal expansion, 10^{-6} m/m per °C (10^{-6} in./in. per °F)	50–80 (28–44)
Cure shrinkage, %	1–5

Figure 12: Typical properties of epoxy resin at 23°C [7]

A broad variety of properties can be achieved with epoxy matrices since there is a wide range of prepolymers, hardeners, and modifiers available. Generally, the epoxy matrix has high strength and durability, excellent adhesion to fibers, and good electrical, thermal, corrosion, and moisture resistance. Epoxies also exhibit a low shrinking rate during curing and do not produce volatiles during curing. The downsides of epoxy resin are high cost compared to polyesters and long curing time. The typical ranges of selected properties are shown in Figure 12. [5, 7, 10, 11, 12]

3.2.2 Thermoplastics

Molecules of thermoplastic polymers have no chemical connections and are only entangled with each other. They can be processed by heat softening or melting and they can be directly recycled. The shelf life of thermoplastics is virtually unlimited and very short processing times can be achieved. Thermoplastic polymers have lower heat and chemical resistance and have lower hardness than thermosets, but they are more ductile. Thermoplastics have higher fracture toughness and resistance to crack propagation and also higher impact energy absorption. Thermoplastics have very high viscosity in liquid state, meaning the wetting of fibers is more difficult and requires more expensive processes. The processing temperature of the thermoplastic polymers is also high, driving the cost upwards. The advantages of thermoplastics are the possibility of joining and repairs by welding, the ability to post-form and post-shape the products, and also their non-tackiness which makes the handling easier. [5, 10]

3.3 Sandwich Materials

A sandwich structure is a special type of laminated structure that typically consists of two facesheets that are bonded to a core using an adhesive (Figure 13). The core increases the distance of the facesheets from the cross section's neutral axis which leads to a tremendous increase in bending stiffness and strength compared to a non-sandwich structure while the increase in the structure's weight is usually minimal. The increase of bending stiffness with increasing core thickness is shown in Figure 14 (note that the typically used core thickness mentioned in the figure applies to large airplanes and it is usually between 1-10 mm for ultralight airplanes). The core should have at least a hundred times lower elastic modulus than the facesheets, but it still has to have sufficient stiffness and strength to transfer the loads to the factsheets, to bear shear and compression stress, and to not collapse during manufacturing. The sandwich structure is ideal for applications where a high buckling load is important or where good impact absorption and fatigue life are necessary. The sandwich structures are cost-effective but their usage introduces new failure modes which have to be taken into account during design. [13, 14, 15, 16]

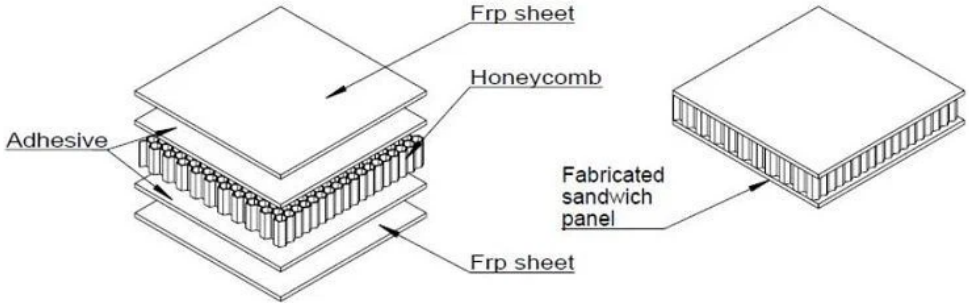

Figure 13: Honeycomb sandwich panel [17]

The three types of typically used sandwich cores are foam or solid cores, corrugated or truss cores, and honeycomb cores. The foam or solid cores are usually used in lower-cost applications but they still show good out-of-plane compression and shear performance, however, their performance is usually lower compared to honeycomb cores. Typical materials used as foam or solid cores are polyurethane foams, polystyrene foams, polyvinylchloride foams, polymethacrylimide foams, and balsa wood. Corrugated cores, usually metallic or from polymer composites, are used in applications where strong anisotropy of stiffness is required - aircraft morphing wings are an example. The sandwich structures with corrugated cores possess good fatigue resistance and energy absorption properties. Honeycomb cores have good energy absorption capabilities and good mechanical strength. Nomex, aluminum, and fiberglass are typical materials used for honeycomb manufacturing and a wide variety of cell shapes and sizes is available to satisfy design requirements, making honeycomb cores the second most used core type after the foam cores. [13]

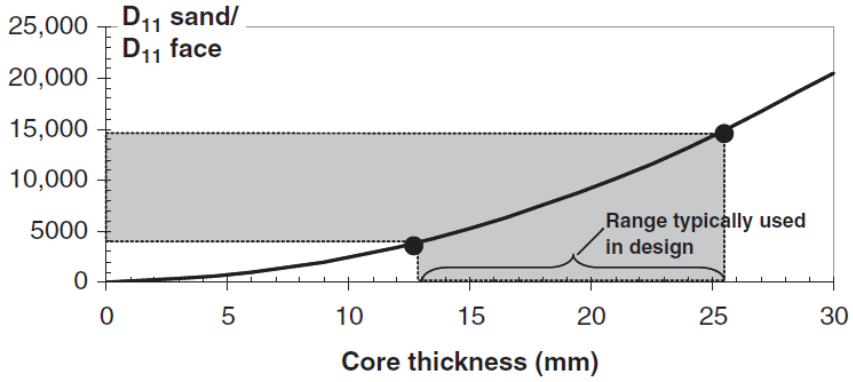

Figure 14: Sandwich stiffness as a function of core thickness [16]

3.4 Thermoset Polymers Composite Manufacturing

The goal of fiber-reinforced polymer manufacturing is to orientate fibers in the appropriate direction in the matrix to achieve the desired properties. The production process must be designed so there is no damage introduced to the fibers, the fibers are evenly distributed in the matrix, and there are no significant voids present. The thermoset polymer matrix is used for the design as the manufacturing processes are cheaper, extensively tried and tested, and the use of thermoset matrices is an industry standard for aerospace applications. Several processes used for the fabrication of fiber reinforced thermoset polymer composites are briefly described but the major part of this subsection is devoted to bag molding as it is the most used process in the aerospace industry and it's also the only technology available at the university for producing parts of the rudder's dimensions. [10]

3.4.1 Bag Molding

Bag molding is a labor-intensive, open-mold process that creates high-quality parts with low void content. The input material can be either in the form of prepreg sheets or dry fabrics or unidirectional continuous fibers can be hand-wetted with thermoset resin. The prepreg is a fabric or tape of unidirectional fibers that is coated with partially cured thermoset resin. The advantages of using prepreg are higher achievable fiber volume fraction, easier manipulation and layup of plies, and low variability in the fiber volume content. There are two prepreg systems, the "bleed" and "zero-bleed" where the former is impregnated with a higher volume of matrix and is expected to achieve the desired fiber volume fraction during the curing process, and the latter is impregnated with the volume corresponding to the target volume after curing. The drawbacks of prepregs are their limited shelf-life which is only days at room temperature, or up to a year when kept in a freezer, and their higher price. [5]

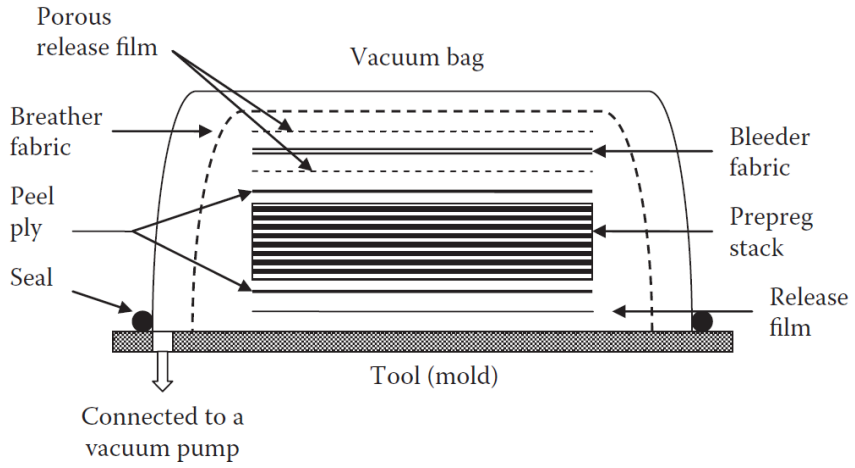

Figure 15: Bag molding setup [5]

The manufacturing process starts with mold cleaning. After the mold is thoroughly cleaned, it is coated with a mold release agent to ensure the part doesn't stick to the mold. The mold can then be covered with a release film to ensure even easier part extraction, and with a peel ply to make the part's surface coarse to help with adhesion when parts are glued together. Subsequently, the layup of the prepreg or hand-wetted plies takes place. The plies are laid in the fiber orientation angles to achieve the desired properties. The layup can be automated by using advanced machines or robots, or it can be made manually which takes longer times, is labor intensive, and a human error can easily lead to an improper layup. After the layup is finished, the peel ply is placed over the part followed by a porous release film and bleeder fabric which absorbs the excess matrix. Breather fabric is then placed over the part to allow gas flow from all over the part to the vacuum fitting. The whole layup is then covered with the vacuum bag which is sealed to the mold to ensure there are no leaks. The cross section of the layup is shown in Figure 15. For thick plies with many plies, a process called debulking is usually used to ensure there are no big voids and gaps between the plies and that

there is sufficient compaction. After several plies are laid, the stack is debulked by applying pressure to its top or by vacuum-bagging the partial stack and this process is repeated until a complete layup is made. [5, 10]

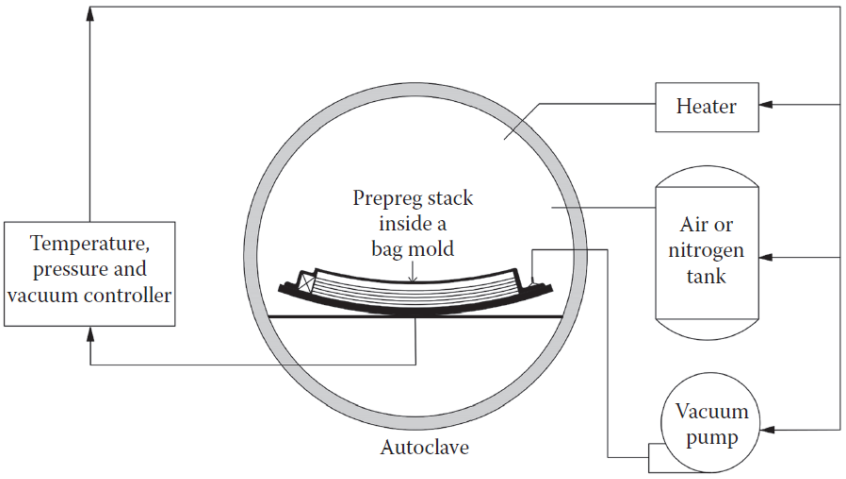

Figure 16: Autoclave bag molding [5]

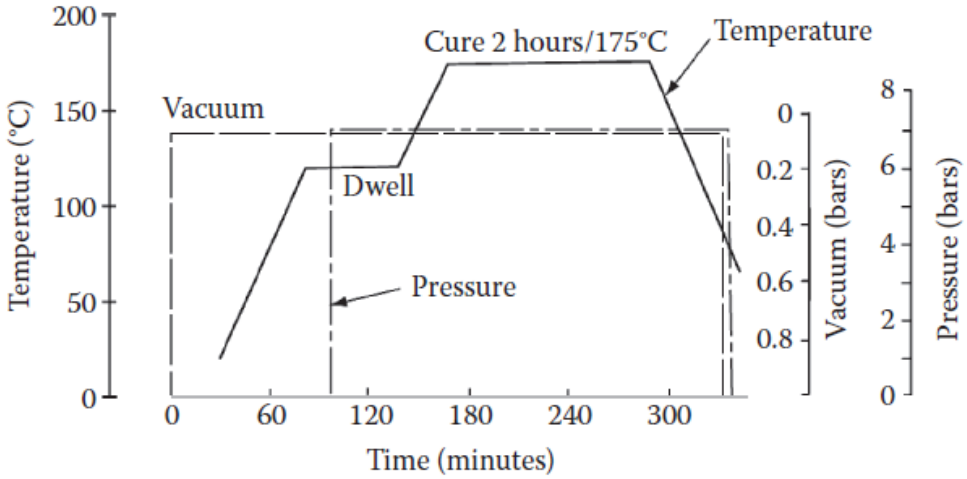

Figure 17: Typical epoxy cure process [5]

Afterwards, the complete assembly is cured, either in the autoclave (Figure 16) or in an oven. In the autoclave external pressure, vacuum, and heat are applied to cure the laminate. The temperature and pressure are varied throughout the cure cycle depending on the used resin and the desired degree of cure. The typical autoclave curing cycle for epoxy composite is shown in Figure 17. Recently prepregs for out-of-autoclave curing were introduced and they are specifically made to be cured only using an unpressurized oven which brings the manufacturing cost down, but the achievable fiber volume content is lower, as voids can be expected in the laminate when fiber volume content is high and consolidating pressure is not applied as shown in Figure 18. When the part cools down after the cure cycle it can be trimmed, holes can be drilled in it, and paint can be applied if it wasn't applied to mold beforehand. [5, 10]

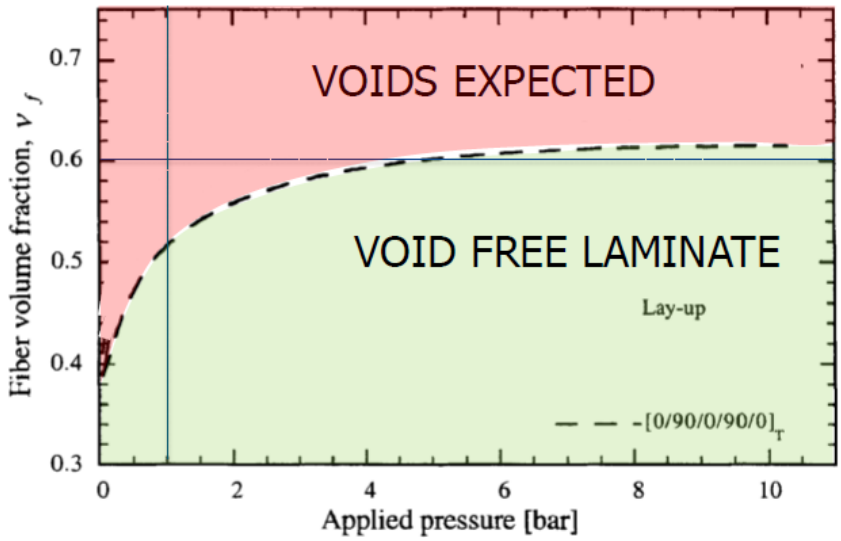

Figure 18: Achievable fiber volume fraction as a function of consolidating pressure [18]

3.4.2 Liquid Composite Molding

Liquid composite molding is a closed-mold process where premixed thermoset resin is injected into a dry fiber preform. The most common LCM process is resin transfer molding (Figure 19). In resin transfer molding a dry preform is placed into a mold, the mold is closed with a press and then the resin is injected under pressure to wet the fibers and displace air from the mold. Parts manufactured with the RTM process have high quality with a fiber volume content of 55-65%. The RTM process is particularly suitable for medium series of small to medium-sized parts as the tooling is not too expensive, time is saved compared to labor-intensive bag molding, and the process can be highly automated. [5, 7, 18]

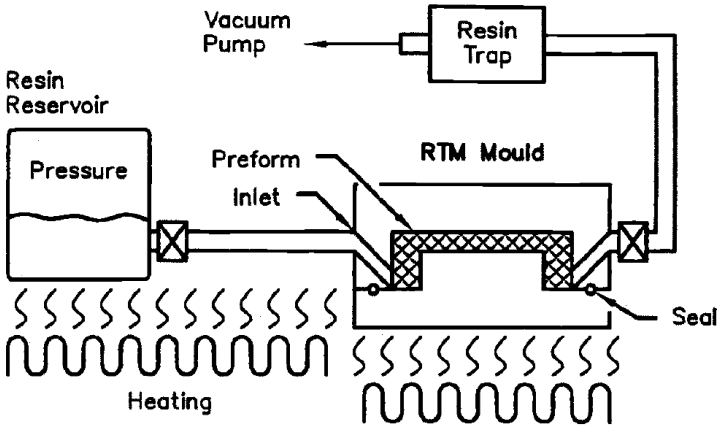

Figure 19: Resin transfer molding [10]

3.4.3 Filament Winding

Filament winding (Figure 20) is a semi-continuous technique for crafting hollow structural elements from continuous fibers. The band of continuous fibers is pulled through a resin

bath and then wound around a rotating mandrel. It allows rapid and precise deposition of the continuous fiber along a predetermined path. The winding tension, winding angle, and resin content can be adjusted to attain the desired characteristics. The mandrel can either stay inside the finished part, which is the case for pressure tanks, or it can be removed or dissolved. Filament winding is best suited for rotational parts without intricate shapes and with constant thickness, however, modern multi-axial machines and advanced control software allow for the production of more complex non-axisymmetric parts. The mechanical properties of filament-wound structures are inferior to the properties of conventionally made composites due to high void content and fiber waviness. [5, 10]

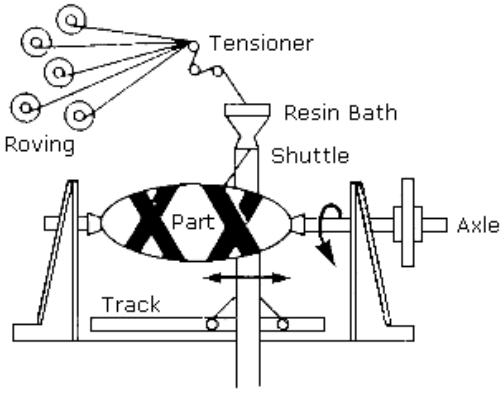

Figure 20: Filament winding [19]

3.4.4 Pultrusion

Pultrusion (Figure 21) is a highly automated continuous process for constant cross sectional profile manufacturing. Tows or rowings are impregnated with thermosetting resin and are drawn through a heated die, where shaping and curing take place. The heat in the die initiates the curing reaction and the product can be either fully cured inside the die or it can be post-cured. The pultrusion isn't widely used within the aerospace market due to the limited production runs for aerospace products and also due to the difficulty in reaching the quality of parts manufactured using other aircraft-molding techniques. [5, 10]

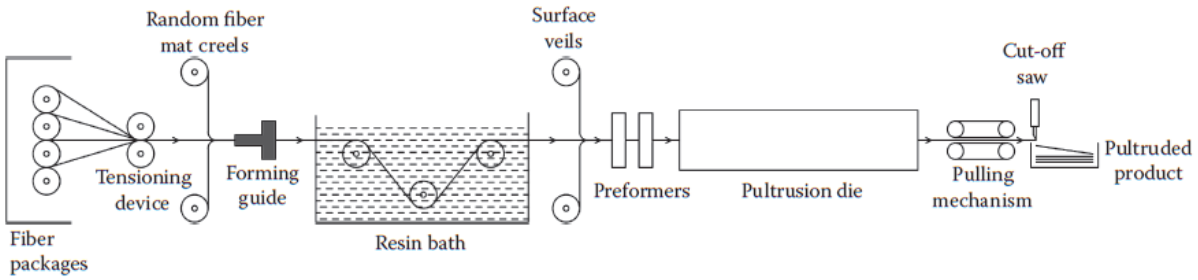

Figure 21: Pultrusion [5]

3.5 Failure Criteria for Composite Materials

The failure mechanics of composite materials are different from isotropic materials. The damage of composite material can start far before the failure stress is achieved, usually in the form of matrix cracks perpendicular to the primary load direction. Micromechanics, which accounts for the individual constituents of the ply, can be used to predict the damage start and evolution in composites, but the use of micromechanics failure criteria significantly increases the complexity and computational cost of the calculations. Therefore, simplified methods that assume the ply is homogeneous and is characterized by its failure modes are introduced. For a unidirectional ply five failure modes are usually acknowledged:

X^t - failure tensile strength along the fibers
X^c - failure compression strength along the fibers
Y^t - failure tensile strength perpendicular to the fibers
Y^c - failure compression strength perpendicular to the fibers
S^f - failure shear strength of a ply

For fabrics, the same denotations can be used where X applies to the fabric's primary direction and Y to the secondary direction. For balanced fabrics, the X and Y are interchangeable. Some of the most commonly used failure theories are described in subsequent sections. [16]

3.5.1 Maximum Stress Failure Theory

In this theory, the principal stresses in a ply are compared to corresponding allowable (failure strength). The maximum stress criterion is non-conservative because it doesn't account for a combination of loads and therefore has to be used with caution. It can be described using the following equations:

$$\begin{aligned} &\sigma_x < X^t \text{ for tensile load or } X^c \text{ for compressive load,} \\ &\sigma_y < Y^t \text{ for tensile load or } Y^c \text{ for compressive load,} \\ &|\tau_{xy}| < S^f \ . \end{aligned} \tag{3.1}$$

If the left side equals or is higher than the right side, failure occurs. [16]

3.5.2 Maximum Strain Failure Theory

The maximum strain theory is analogous to the maximum stress theory: [16]

$$\begin{aligned} &\varepsilon_x < \varepsilon_{xu}^t \text{ for tensile strain or } \varepsilon_{xu}^c \text{ for compressive strain ,} \\ &\varepsilon_y < \varepsilon_{yu}^t \text{ for tensile strain or } \varepsilon_{yu}^c \text{ for compressive strain,} \\ &|\gamma_{xy}| < \gamma_{xyu} \ . \end{aligned} \tag{3.2}$$

3.5.3 Tsai-Hill Failure Theory

The Tsai-Hill theory is a quadratic stress failure criterion that includes the effects of multiaxial loads and was derived from the von Mises yield criterion. The failure envelope is defined by the following equation:

$$\frac{\sigma_x^2}{X^2} - \frac{\sigma_x \sigma_y}{X^2} + \frac{\sigma_y^2}{Y^2} + \frac{\tau_{xy}^2}{Sf^2} = 1 \, . \tag{3.3}$$

If $\sigma_x > 0, X = X^t$ and if $\sigma_x < 0, X = X^c$. If $\sigma_y > 0, Y = Y^t$ and if $\sigma_y < 0, Y = Y^c$. If the left side of the equations stays below one, failure will not occur. The Tsai-Hill criterion should not be used for fabrics and should be used for transversally isotropic materials only. [10, 16, 20]

3.5.4 Tsai-Wu Failure Theory

The Tsai-Wu criterion (Equation 3.4) is a curve fit-based model of failure, developed as an attempt to generalize the Tsai-Hill failure criterion. The Tsai-Wu criterion provides acceptable to excellent results and can be reliably applied to fabrics, except in cases of biaxial compression, where the predictions are unrealistic. [16]

$$\frac{\sigma_x^2}{X^t X^c} + \frac{\sigma_y^2}{Y^t Y^c} - \sqrt{\frac{1}{X^t X^c}\frac{1}{Y^t Y^c}}\sigma_x \sigma_y + \left(\frac{1}{X^t} - \frac{1}{X^c}\right)\sigma_x + \left(\frac{1}{Y^t} - \frac{1}{Y^c}\right)\sigma_y + \frac{\tau_{xy}^2}{Sf^2} = 1 \tag{3.4}$$

3.5.5 Puck Failure Theory

The Puck criterion is, as opposed to the criteria mentioned above, based on the failure behavior of brittle materials which is more appropriate for composite materials as their failure is primarily governed by brittle fracture. It is strongly physic-based and it accounts for fiber and matrix properties separately. *"Despite its appeal, the Puck criterion involves parameters that require significant extra effort to determine such as the slopes of the failure surfaces, the transverse stress magnification factors, and the location and inclination of the fracture plane."* [16] Therefore, the expressions of the failure criteria will not be mentioned as the use of this criterion would require extensive material tests which are out of the scope of this thesis. [16]

3.5.6 Hashin-Rotem Failure Theory

The Hashin-Rotem failure theory is a criterion specialized for unidirectional plies, taking individual failure modes into account. It is non-conservative for fiber mode failures but provides accurate results for complex stress states. The expressions for the failure envelope are as follows: [16, 20]

For fiber failure:

$$\frac{\sigma_x}{X^t} = 1 \text{ when } \sigma_x \text{ is tensile,}$$
$$\frac{\sigma_x}{X^c} = 1 \text{ when } \sigma_x \text{ is compressive.}$$

For matrix failure: (3.5)

$$\frac{\sigma_y^2}{(Y^t)^2} + \frac{\tau_{xy}^2}{S^{f2}} = 1 \text{ when } \sigma_y \text{ is tensile,}$$
$$\frac{\sigma_y^2}{(Y^c)^2} + \frac{\tau_{xy}^2}{S^{f2}} = 1 \text{ when } \sigma_y \text{ is compressive.}$$

In Figure 22 comparison of failure envelopes of the Maximum stress, Tsai-Hill, Tsai-Wu, and Hashin-Rotem criteria applied to unidirectional plies (***(a)-(c)***) and fabric plies (***(d)-(f)***) is shown. For further calculations, the Tsai-Hill failure criterion is used for unidirectional plies as it's the most conservative of the discussed ones, and the Tsai-Wu criterion is used for fabrics as it can be reliably used for fabrics and appears as the most conservative for them.

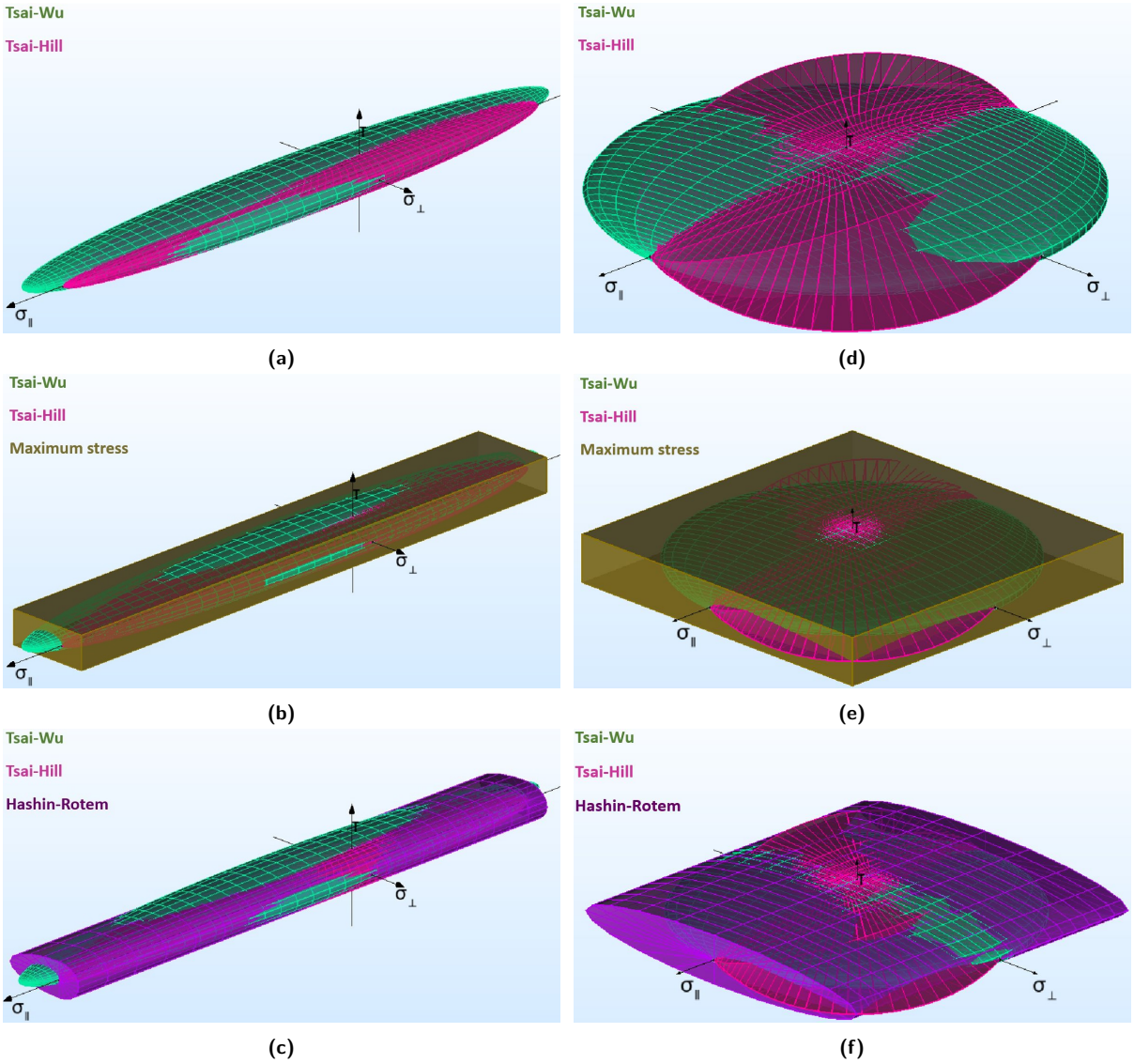

Figure 22: Comparison of selected failure theories

4 Selection of Materials for the Design

Parts of the rudder's structure are designed for two manufacturing processes - the vacuum bag molding process using hand-wetted fibers and the bag molding process using prepreg sheets. The weight of the two designs is compared to determine if the weight saving that comes with the prepreg usage justifies the added cost. The design using prepreg sheets should be lighter thanks to the higher achievable fiber volume content and the lower required load safety factor as there is a lower variability in the properties of prepreg layups compared to the hand-wetted layups.

The epoxy matrix is used for both designs owing to its favorable properties mentioned in Section 3.2.1 together with carbon fibers, which offer high specific strength and stiffness that is needed for a lightweight design. Their higher price is justified as the airplane's designation is to set new world records and the disadvantages of low impact resistance and susceptibility to lightning damage are not significant since the rudder is usually not prone to impact damage and ultralight airplanes shouldn't fly in stormy weather. Carbon fibers are used in the forms of unidirectional tapes and woven fabrics as woven fabrics are the most common type of fabrics, there are therefore many variations with different areal weights (thus different ply thicknesses) available, and they offer good drapeability and handling during manufacturing. A sandwich structure is used for skin and web to ensure sufficient stability.

4.1 Prepreg Materials

It is planned to manufacture the rudder sooner than the whole aircraft which is a complication as only the whole rolls (at least 50 m^2) of prepreg materials are usually available for purchase. Numerous prepregs with different areal weights of reinforcements must be used for effective design so more rolls would have to be purchased and the material would most likely not be used within the shelf-life (30 days at 20°C or 12 months at -18°C). One e-shop was found (*www.easycomposites.eu*) where as little as 1 m^2 of prepreg can be purchased. They offer both out-of-autoclave and autoclave prepregs, but the range of out-of-autoclave prepregs is limited to only two different fabric reinforcements which would not be sufficient for the design and therefore the epoxy autoclave system XPREG XC130 is used. The recommended cure temperature is between 80°C and 120°C with a possibility of post-cure at 130°C. To ensure reliable bonding of core materials to the prepreg sheets, prepreg adhesive film with the areal weight of 150 g/m^2 is available. [21, 22]

Material properties are shown in Table 1. The mechanical properties given in the material's technical datasheet [22] are valid for laminate with 210 g/m^2 2x2 twill fabric and the properties of the other variants were re-calculated based on the fiber volume content, except for the shear properties, which are not so dependent on the fiber volume fraction. [23]

Reinforcement type			**Spread-Tow Fabric 1x1 Plain**	**Fabric 2x2 Twill**	**Fabric 2x2 Twill**	**UD**	**UD**
Reinforcement areal weight		**[g/m^2]**	**88**	**210**	**450**	**150**	**300**
Consolidated ply thickness	t	**[mm]**	0.12	0.25	0.45	0.15	0.3
Fiber volume content	v_f	**[%]**	41.20	47.19	56.18	56.18	56.18
Areal weight of lamina	w_A	**[g/m^2]**	171.97	367.11	684.66	228.22	456.44
Tensile strengths	X^t/Y^t	**[MPa]**	563 / 563	645 / 645	768 / 768	1536 / 46	1536 / 46
Compressive strengths	X^c/Y^c	**[MPa]**	537 / 537	615 / 615	732 / 732	1000 / 120	1000 / 120
Shear strength	S^f	**[MPa]**	69.8	69.8	69.8	77	77
Tensile modulus	E_1/E_2	**[GPa]**	48.2 / 48.2	55.2 / 55.2	65.7 / 65.7	131.4 / 7.3	131.4 / 7.3
Shear modulus	G_{12}	**[GPa]**	4.2	4.2	4.2	4.2	4.2
Poisson ratio	ν_{12}	**[-]**	0.06	0.06	0.06	0.32	0.32

Table 1: Properties of XPREG XC130 system [22, 24]

For unidirectional reinforcements, the tensile strength in the direction of the fibers was calculated by doubling the tensile strength of the fabric, which is a conservative method. The compressive strength of the unidirectional prepreg ply stated in the thesis of Vojtěch Malý [24] is 1200 MPa, but 1000 MPa is used to be on the conservative side as a small manufacturing error can cause a significant drop in compressive properties. The in-plane shear strength is not stated in the datasheet and interlaminar shear strength is stated instead. The in-plane shear strength should be higher than the interlaminar shear strength [25] so the interlaminar shear strength is used to keep the calculations conservative. The transverse properties of the unidirectional ply are assumed to coincide with the properties of the epoxy matrix. Properties that weren't given in the datasheet or discussed above are taken from the master's thesis of Vojtěch Malý [24].

4.2 Materials for "Hand-Wetted Design"

The fabrics and tapes for hand-wetted design are chosen from the e-shop of Havel Composites [26] as they offer a wide range of materials and it is possible to order quantities starting from one square meter. The expected fiber volume content of hand-wetted fabrics subsequently cured in a vacuum bag is 40% and 45% for unidirectional tapes. [27] The properties that are strongly affected by the fiber volume content will be recalculated from the prepreg properties shown in Table 1 and the shear strength and transverse properties of UD tapes from the resin's (choice of resin is described further) datasheet [28] are used. The chosen reinforcing fabrics are shown in Table 2 with their properties in Table 3 and the chosen UD tapes are shown in Table 4 and their properties are in Table 5. The maximum compressive strength of hand-wetted UD tapes is lowered to 800 MPa due to the more difficult handling of dry tape during which the tape can fray or the fibers can buckle resulting in significantly reduced strength.

The EPIKOTE™ MGS® LR285 resin with EPIKURE™ MGS® LH287 curing agent is expected to be used as a matrix for hand-wetted design. This resin is approved by the German Federal Aviation Authority for manufacturing of gliders, motor gliders, and general aviation airplanes. After heat treatment at 80°C the safe operational temperatures are between -60°C and $+72$°C. If the heat resistance is not necessary, the heat treatment can be done using lower temperatures, or it doesn't have to be done altogether but at least 50°C is recommended to obtain the properties stated in the datasheet. The LR285 resin and the LH287 curing agent have to be mixed in a $100 : 40 \pm 2$ weight ratio or $100 : 51 \pm 2$ volume ratio, close attention must be paid to the mixing ratio as any deviation from the stated ratios will cause incomplete curing and therefore inferior properties. The potlife of the mix is approximately 140 minutes and a gel time is 5-6 hours at 20-25°C or 80-120 minutes at 40-45°C. [28]

Fabric type		1x1 Plain	1x1 Plain	2x2 Twill	2x2 Twill	4x4 Twill
Reinforcement areal weight	[g/m^2]	93	120	160	200	280
Consolidated ply thickness	[mm]	0.13	0.17	0.22	0.28	0.39
Areal weight of lamina	[g/m^2]	186.26	240.34	320.45	400.56	560.79

Table 2: Selected reinforcing fabrics [26]

Fiber volume content	v_f	40	%
Tensile strength	$X^t = Y^t$	546	MPa
Compressive strengths	$X^c = Y^c$	521	MPa
Shear strength	S^f	55	MPa
Tensile modulus	$E_1 = E_2$	46.8	GPa
Shear modulus	G_{12}	4.2	GPa
Poisson ratio	ν_{12}	0.06	[-]

Table 3: Properties of hand-wetted fabrics

Reinforcement areal weight	[g/m^2]	80	125	200	300
Consolidated ply thickness	[mm]	0.10	0.16	0.25	0.37
Areal weight of lamina	[g/m^2]	145.37	227.14	363.42	545.13

Table 4: Selected reinforcing UD tapes [26]

Fiber volume content	v_f	45	%
Tensile strength	X^t/Y^t	1230 / 46	MPa
Compressive strengths	X^c/Y^c	800 / 120	MPa
Shear strength	S^f	70	MPa
Tensile modulus	E_1/E_2	105.3 / 7.3	GPa
Shear modulus	G_{12}	4.2	GPa
Poisson ratio	ν_{12}	0.32	[-]

Table 5: Properties of hand-wetted UD tapes

4.3 Core Material

Several core materials were considered to be used. The choice was made to use ROHACELL® 51 IG-F foam as the core material thanks to its high specific properties, thermoformability, and ease of machining. It is also particularly suitable for prepreg processing up to temperatures of 130°C. The foam is available in the form of sheets with 1, 3, 6, 7, and 8 mm thickness, thicker sheets are also available but the necessity of more than 8 mm is not probable. Properties of this foam are summarized in Table 6. [29]

4.4 Steel

AISI 4140 (also known as 42CrMo4) is a chromium-molybdenum alloy steel that offers good toughness, ductility, and wear resistance. It can be easily machined, but welding can be challenging, although it is possible using common welding techniques. This steel is used

for parts of the hinges and the tail wheel attachment. Mechanical properties of AISI 4140 in quenched and tempered form, with diameters ranging from 16 to 40 mm, are detailed in Table 7. [30]

Density	ρ	52	kg/m^3
Poisson ratio	ν	0.25	[-]
Compressive strength	σ_c^u	0.9	MPa
Compressive modulus	E_c	43	MPa
Tensile strength	σ_t^u	1.9	MPa
Tensile modulus	E_t	70	MPa
Shear strength	σ_S^u	0.8	MPa
Shear modulus	G	19	MPa

Table 6: Properties of ROHACELL® 51 IG-F [29]

Density	ρ	7800	kg/m^3
Poisson ratio	ν	0.3	[-]
Young's modulus	E	210	GPa
Shear modulus	G	80	GPa
Ultimate tensile strength	σ_t^u	1000	MPa
Yield tensile strength	σ_t^y	750	MPa

Table 7: Properties of AISI 4140 [31, 32]

5 Rudder Loads

In most aircraft, the rudder is subject only to aerodynamic and inertia loads. However, in our case, the tail wheel is incorporated into the rudder, meaning the ground loads must also be considered. The inertia loads will be neglected in the calculations, as the loads shouldn't be significant, given the anticipated low weight of the rudder and the magnitude of the ground and aerodynamic loads. In addition to the aerodynamic and ground loads, control loads that are transferred from the rudder pedals to the rudder control horn by cables have to be taken into account. All the loads calculated in this section are limit loads.

5.1 Aerodynamic Loads

The loads acting on the rudder caused by its deflection (manoeuvring loads) and loads caused by a change in the angle of attack of the vertical tail (gust loads) are calculated in this subsection.

5.1.1 Vertical Tail Geometry

The vertical tail geometry is needed for aerodynamic loads calculations. The slightly simplified geometry which is used for the calculations can be seen in Figure 23. The blue lines outline the shape of the rudder and the orange lines outline the shape of the vertical stabilizer. The red chain line represents the rudder's axis of rotation. All the dimensions except for the total VT height L are changing with the z coordinate, which is also shown in the figure.

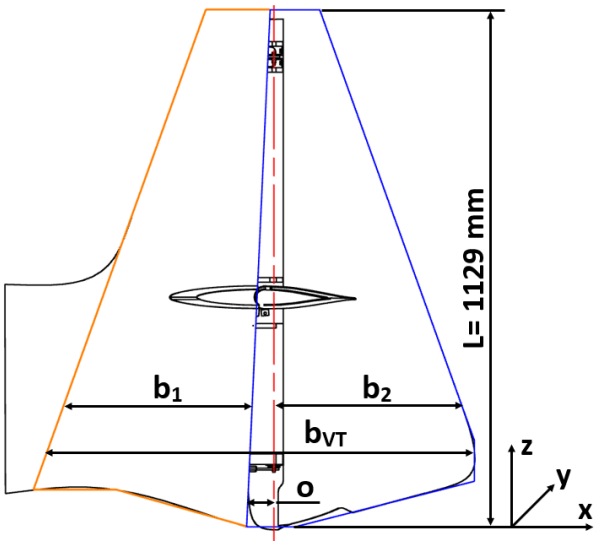

Figure 23: Vertical tail geometry

5.1.2 Manoeuvring Loads

When no more precise ways to calculate the loads are available, the chordwise distribution shown in Figure 24 may be used. The b_{OP} in Figure 24 corresponds to the b_{VT} in Figure 23. The average pressure load acting on the vertical tail during maouevre $\overline{W_m}$ may be calculated using Equation 5.1, where the minimum permissible average pressure for the design is $\overline{W_m} = 575\ Pa.$ [2]

$$\overline{W_m} = 220 + 20.5 \cdot \frac{MTOM}{A} \quad [Pa] \tag{5.1}$$

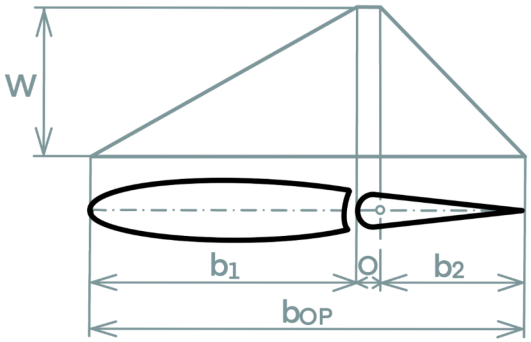

Figure 24: Chordwise load distribution for manoeuvring load [3]

The average pressure load acting on the vertical tail during manoeuvre is:

$$\overline{W_m} = 220 + 20.5 \cdot \frac{345}{5.029} = 1626.343\ Pa\ . \tag{5.2}$$

The pressure is greater than the minimum permissible pressure mentioned previously and therefore can be used for the design. The equation for the pressure parameter W_m used to determine the load distribution is derived using the equivalent area assumption:

$$\overline{W_m} \cdot b_{VT} = \frac{1}{2} \cdot W_m \cdot b_1 + \frac{1}{2} \cdot W_m \cdot b_2 + W_m \cdot o\ , \tag{5.3}$$

$$W_m = \frac{\overline{W_m} \cdot b_{VT}}{\frac{1}{2} \cdot (b_1 + b_2) + o}\ . \tag{5.4}$$

W_m is not constant in the spanwise direction as it's dependent on b_1, b_2, b_{VT}, and o that all change spanwise. The spanwise distribution of W_m is shown in Figure 25.

The distributed load acting on the rudder in the spanwise direction q_m can be calculated using Equation 5.5. The distributed load spanwise distribution is then shown in Figure 26.

$$q_m = W_m \cdot \left(o + \frac{b_2}{2} \right) \quad [N/m] \tag{5.5}$$

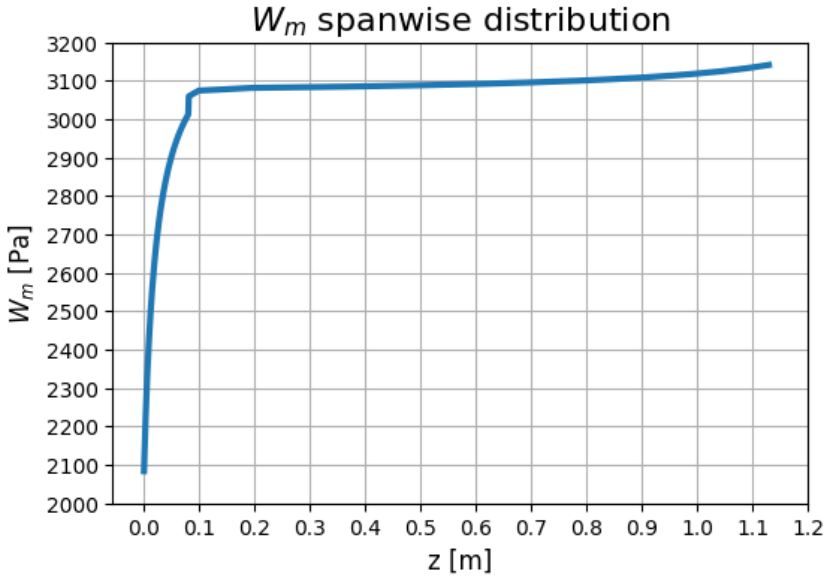

Figure 25: Spanwise distribution of W_m

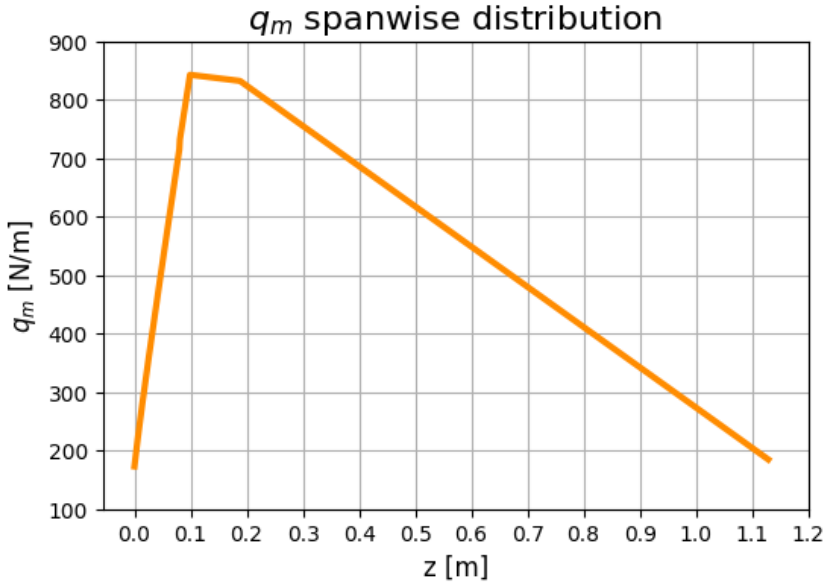

Figure 26: Spanwise distribution of q_m

In the chordwise dimension, the load is concentrated to one point for the calculations, the position of which is calculated. The torsion moment caused by the concentrated force must be the same as the moment caused by the chordwise distributed load. The distance of the point from the rudder's axis of rotation can be calculated using Equation 5.6 and the distances along the span are graphed in Figure 27.

$$x_{q_m} = \frac{W_m \cdot \left(-\frac{o^2}{2} + \frac{b_2^2}{6}\right)}{W_m \cdot \left(o + \frac{b_2}{2}\right)} = \frac{\left(-\frac{o^2}{2} + \frac{b_2^2}{6}\right)}{\left(o + \frac{b_2}{2}\right)} \quad [m] \tag{5.6}$$

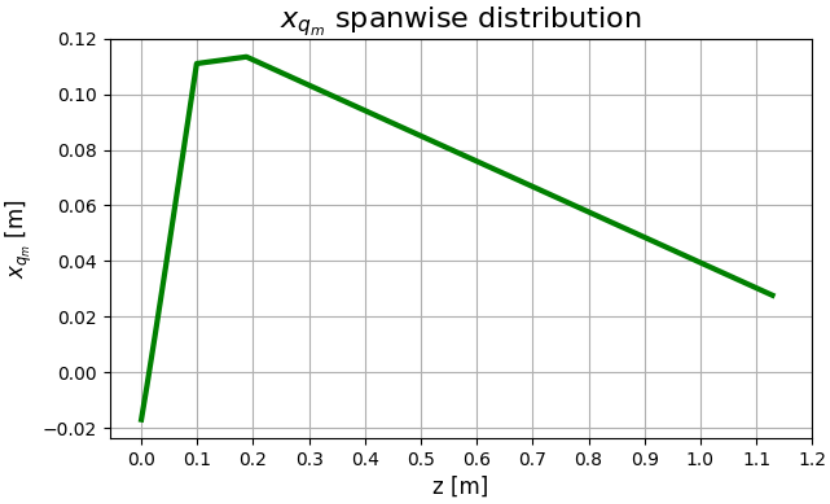

Figure 27: Spanwise distribution of x_{q_m}

5.1.3 Gust Loads

The equation from UL 2 regulation [2] is applied to calculate the total load on the vertical tail caused by gust P_{VT} because no more precise calculation method is available.

$$P_{VT} = 0.5 \cdot \rho_0 \cdot a_{VT} \cdot A_{VT} \cdot U \cdot k_{VT} \cdot V \quad [N] \,, \tag{5.7}$$

where:

$\rho_0 =$ *air density at sea level* $(1.225\ kg/m^3)$,
$V =$ *flight velocity* $[m/s]$,
$A_{VT} =$ *surface of the vertical tail* $[m^2]$,
$a_{VT} =$ *lift curve slope of vertical tail* $[1/rad]$,
$U =$ *gust velocity* $[m/s]$,
$k_{VT} =$ *gust alleviation factor* $[-]$,

$$k_{VT} = \frac{0.88 \cdot \mu}{5.3 + \mu} \quad [-] \,, \tag{5.8}$$

and:

$$\mu = \frac{2 \cdot MTOM}{A_{VT} \cdot \rho_0 \cdot lm_V \cdot a_{VT}} \quad [rad] \,, \tag{5.9}$$

where:

lm_V = *mean geometric chord of vertical surface*.

P_{VT} must be calculated for two cases. The airplane must withstand a lateral gust of 15 m/s in unaccelerated flight at speed V_B (design rough air speed) and a lateral gust of 7.5 m/s in unaccelerated flight at speed V_D (design diving speed). [2]

The numerical values needed for gust load determination, except for the a_{VT} that needs to be calculated, are summarized below:

$$\begin{aligned} V_D &= 510 \quad km/h\ , \quad [33] \\ V_D &= 141.667 \quad m/s\ , \\ V_B &= 273 \quad km/h\ , \quad [33] \\ V_B &= 75.833 \quad m/s\ , \\ A_{VT} &= 0.6833 \quad m^2\ , \\ U_{V_D} &= 7.5 \quad m/s\ , \\ U_{V_B} &= 15 \quad m/s\ , \\ lm_V &= 0.564 \quad m\ . \end{aligned}$$

To determine the lift curve slope of the vertical tail, the lift slope of the NACA $66_1 - 012$ airfoil was found in NACA Report No. 824 [34] to be $c_{l\alpha} = 5.984\ rad^{-1}$. The lift slope of the VT depends on the airplane's velocity, so there are two different values for the two cases. The *Polhamus equation* for the lift slope which is valid for noncurved planform shapes and $M \leq 0.8$ [35] is used:

$$c_{L\alpha_{VT}} = a_{VT} = \frac{2 \cdot \pi \cdot AR}{2 + \sqrt{\left(\frac{AR \cdot \beta}{k}\right)^2 \cdot (1 + \frac{tan^2 \Lambda_C}{\beta^2}) + 4}}\ . \tag{5.10}$$

The coefficient β is the Mach number parameter:

$$\beta = \sqrt{1 - M^2} = \sqrt{1 - \left(\frac{v}{\sqrt{\kappa \cdot r \cdot T}}\right)^2}\ , \tag{5.11}$$

k is a ratio of 2-dimensional lift curve slope to 2π:

$$k = \frac{\frac{c_{l\alpha}}{\beta}}{2\pi}\ . \tag{5.12}$$

AR is the aspect ratio of VT that can be calculated using the following equation:

$$AR = \frac{L^2}{A_{VT}}\ , \tag{5.13}$$

and Λ_C is the sweepback of the vertical tail's mid-chord, for our airplane, there is no sweepback, therefore $\Lambda_C = 0$.

The numerical calculation of $c_{L\alpha_{VT}}$ and then of P_{VT} is shown for the design diving speed V_D case:

$$AR = \frac{1.129^2}{0.6833} = 1.86542 \ , \tag{5.14}$$

$$\beta = \sqrt{1 - \left(\frac{141.667}{\sqrt{1.4 \cdot 287 \cdot 288.15}}\right)^2} = 0.9092 \ , \tag{5.15}$$

$$k = \frac{\frac{5.984}{0.902}}{2\pi} = 1.04749 \ . \tag{5.16}$$

Now all the variables for a_{VT} calculation are known:

$$a_{VT} = \frac{2 \cdot \pi \cdot 1.865}{2 + \sqrt{\left(\frac{1.865 \cdot 0.9092}{1.04749}\right)^2 \cdot (1+0) + 4}} = 2.5629 \ rad^{-1} \ , \tag{5.17}$$

$$\mu = \frac{2 \cdot 345}{0.6833 \cdot 1.225 \cdot 0.564 \cdot 2.5629} = 570.285 \ rad \ , \tag{5.18}$$

$$k_{VT} = \frac{0.88 \cdot 570.285}{5.3 + 570.285} = 0.8719 \ , \tag{5.19}$$

$$P_{VT} = 0.5 \cdot 1.225 \cdot 2.5629 \cdot 0.6833 \cdot 7.5 \cdot 0.8719 \cdot 141.667 = 993.67 \ N \ . \tag{5.20}$$

The calculated values for both cases are to be seen in Table 8.

Case	**V [m/s]**	**U [m/s]**	β **[-]**	**k [-]**	$\mathbf{a_{VT}}$ **[rad^{-1}]**	μ **[rad]**	$\mathbf{k_{VT}}$ **[-]**	$\mathbf{P_{VT}}$ **[N]**
V_D	141.667	7.5	0.9092	1.04749	2.563	570.285	0.8719	993.7
V_B	75.833	15	0.9748	0.97695	2.477	590.102	0.8722	1028.4

Table 8: Gust load on the vertical tail

The average pressure acting on the VT during gust $\overline{W_g}$ is calculated by dividing the load P_{VT} by the tail's surface:

$$\overline{W_g} = \frac{P_{VT}}{A_{VT}} \quad [Pa] \ . \tag{5.21}$$

The chordwise load distribution for gust load is pictured in Figure 28. The parameter W must be calculated to determine the numerical pressure distribution, it will be further denoted as W_g.

W_g is calculated using the equivalent area assumption analogically as for the maneuvering load:

$$\overline{W_g} \cdot b_{VT} = \frac{1}{4} \cdot b_{VT} \cdot W_g + \frac{3}{8} \cdot b_{VT} \cdot W_g + \frac{3}{8} \cdot b_{VT} \cdot W_g \ . \tag{5.22}$$

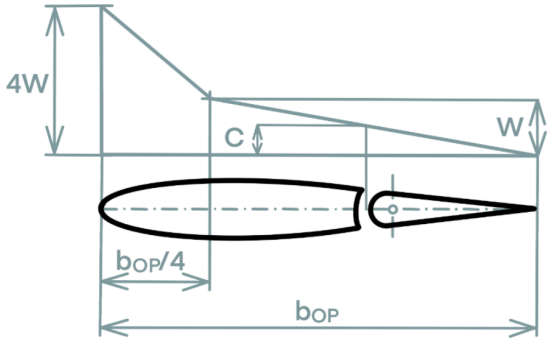

Figure 28: Chordwise load distribution for gust load [3]

Cancelling and collecting terms:

$$\overline{W_g} = W_g \ . \tag{5.23}$$

As evident from Table 8, the load is higher for the V_B case, therefore W_g may be calculated only for this case:

$$\overline{W_g} = W_g = \frac{1028.4}{0.6833} = 1505.054 \ Pa \ . \tag{5.24}$$

The distributed load acting on the rudder in the spanwise direction for the gust load q_g can be calculated using Equation 5.25 and the point at which the load acts in the chordwise direction can be found using Equation 5.26, where the result is the distance from the rudder's axis of rotation. The distributions of q_g and x_{q_g} are graphed in Figure 29 and Figure 30, respectively.

$$q_g = \frac{W_g \cdot (b_2 + o)^2}{\frac{3}{2} \cdot b_{VT}} \quad [N/m] \tag{5.25}$$

$$x_{q_g} = \frac{1}{3} \cdot (b_2 + o) - o \quad [m] \tag{5.26}$$

When comparing Figures 29 and 26, it's apparent the maneuvre case is the critical case for the rudder design, as the distributed load is approximately three times higher than for the gust case.

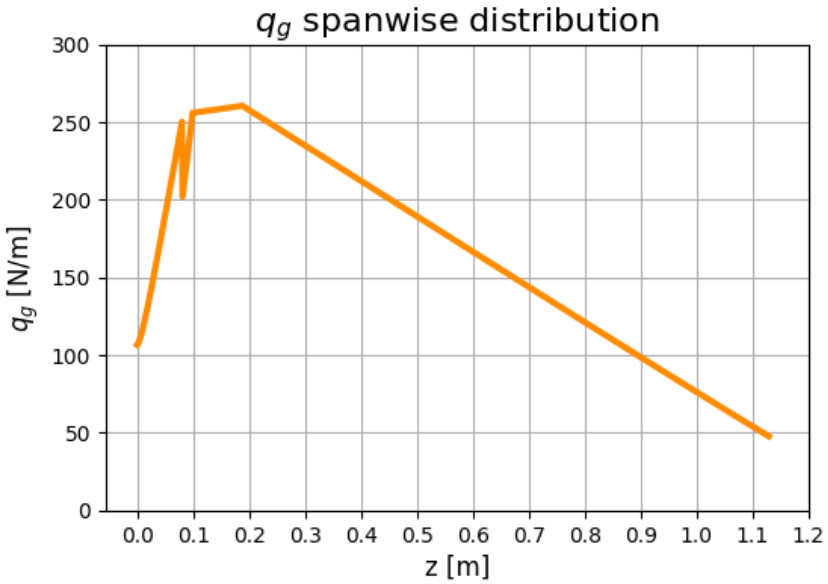

Figure 29: Spanwise distribution of q_g

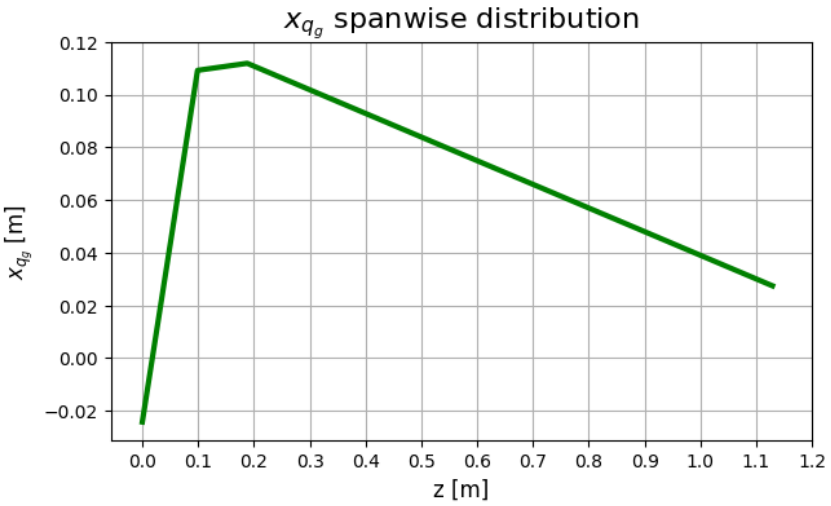

Figure 30: Spanwise distribution of x_{q_g}

5.2 Ground Loads

The ground loads acting on the tail wheel are calculated in this subsection. The critical configurations for ground loads calculations are configurations with aft CG and high take-off mass. Three possibly critical configurations were identified from the thesis of Jakub Valenta [1]. The masses and CG positions of the configurations can be found in Table 9. The numerical solution for the equations in this section is shown for configuration 1. Numerical values for the other configurations are shown in tables.

Configuration	m [kg]	$\overline{x_{cg}}$ [% MAC]
1	345	36
2	302.3	37
3	300.3	37.5

Table 9: Critical ground loads configurations [1]

5.2.1 Tail-down landing condition

For this condition, the main and tail wheels are assumed to contact the ground simultaneously. The descent velocity *ws* used for calculations can't be lower than 1.5 m/s and doesn't have to be higher than 3 m/s. Equation 5.27 is used to check if the descent velocity is within the mentioned bounds. [2]

$$ws = 0.51 \cdot \sqrt[4]{m \cdot \frac{g}{A}} \tag{5.27}$$

$$ws^1 = 0.51 \cdot \sqrt[4]{345 \cdot \frac{9.81}{5.029}} = 2.598 m/s \tag{5.28}$$

As shown in Table 10, all the descent velocities are within the given bounds, and we can proceed with the landing limit load factor calculation.

Configuration	ws [m/s]
1	2.598
2	2.513
3	2.509

Table 10: Descent velocities

According to UL 2 [2], the limit load factor in the airplane's center of gravity can be calculated using the following equation:

$$n_{pr} = n_k + 0.67 \ , \tag{5.29}$$

where:

$$n_k = \frac{0.0132 \cdot \sqrt{m \cdot \frac{g}{A}} + \frac{y_T}{3}}{y_{ef}} , \tag{5.30}$$

where:

$y_T = y_{PN} + y_{TL} = 0.072 + 0.188 = 0.26\,m$ [36] ,

and:

$y_{ef} = 0.5 \cdot y = 0.13\,m$ *for spring-dampened landing gear* [2] ,

$$n_k^1 = \frac{0.0132 \cdot \sqrt{345 \cdot \frac{9.81}{5.029}} + \frac{0.26}{3}}{0.13} = 3.301 , \tag{5.31}$$

$$n_{pr}^1 = 3.301 + 0.67 = 3.971 . \tag{5.32}$$

The limit load factors for landing are shown in Table 11.

Configuration	n_k [-]	n_{pr} [-]
1	3.301	3.971
2	3.132	3.802
3	3.124	3.794

Table 11: Landing limit load factors

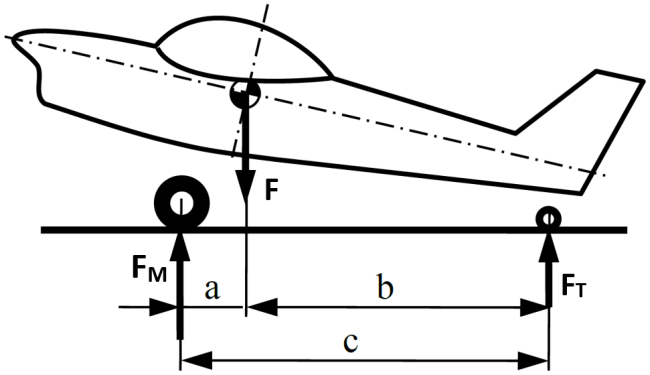

Figure 31: Tail-down landing schematic [2]

When the limit load factors are known, the ground reaction acting on the tail wheel for tail-down landing F_T can be calculated using Equation 5.33 taken from UL 2 regulation [2].

$$F_T = (n_{pr} - 0.667) \cdot M \cdot g \cdot \frac{a}{c} \tag{5.33}$$

$$F_T^1 = (3.971 - 0.667) \cdot 345 \cdot 9.81 \cdot \frac{836}{3856} = 2424.197\ N \tag{5.34}$$

Configuration	a [mm]	b [mm]	c [mm]	$\mathbf{F_T}$ [N]
1	836	3020	3856	2424.197
2	840	3016	3856	2025.537
3	844	3012	3856	2016.45

Table 12: Ground reaction acting on the tail wheel for tail-down landing

5.2.2 Supplementary conditions for tail wheels

There are two supplementary conditions that must not be omitted from the ground load analysis: [2, 37]

1. *"For the obstruction load, the limit ground reaction obtained in the tail-down landing condition is assumed to act up and aft through the axle at 45°."* [37]
2. *"For the side load, a limit vertical ground reaction equal to the static load on the tail wheel, in combination with a side component of equal magnitude, is assumed."* [37]

For the tail-wheel design and its attachment to the surrounding supporting structure Equation 5.35 may be used to determine the reaction acting on the tail wheel P for landing when the tail wheel touches the ground before the main wheels. [2]

$$P = 4 \cdot m \cdot g \cdot \frac{i_y^2}{i_y^2 + b^2} \ , \tag{5.35}$$

where:

$i_y =$ *radius of inertia of the airplane* ,
$b =$ *distance from airplane's CG to the tail wheel* .

The radius of inertia can be calculated using the following equation: [2]

$$i_y = 0.225 \cdot L_{fu} \ , \tag{5.36}$$

where:

$L_{fu} =$ *total length of airplane's fuselage without rudder* ,

$$i_y = 0.225 \cdot 4.57 = 1.0283 \ m \ , \tag{5.37}$$

$$P^1 = 4 \cdot 345 \cdot 9.81 \cdot \frac{1.0283^2}{1.0283^2 + 3.02^2} = 1406.358 \ N \ . \tag{5.38}$$

As we can see when comparing Table 13 and Table 12, the reaction P is in all cases lower than the ground reaction acting on the tail wheel for tail-down landing F_T. Therefore, the ground reaction F_T is used for the obstruction load.

Configuration	P [N]
1	1406.358
2	1235.226
3	1229.975

Table 13: Reaction acting on the tail wheel P

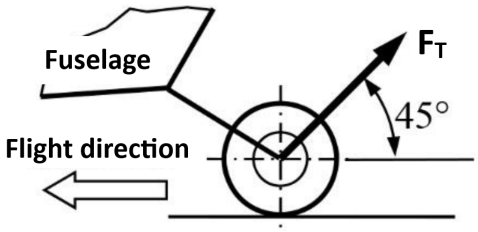

Figure 32: Obstruction load schematic [2]

Equation 5.33 can be used to determine the tail wheel static load after setting the parentheses equal to 1:

$$P_{st} = m \cdot g \cdot \frac{a}{c} \,, \tag{5.39}$$

$$P_{st}^{1} = 345 \cdot 9.81 \cdot \frac{836}{3856} = 733.766 \; N \,. \tag{5.40}$$

The total reaction for the side load case P_{tot} can be calculated using the Pythagorean theorem as apparent from Figure 33:

$$P_{tot} = \sqrt{2 \cdot {P_{st}}^2} \,, \tag{5.41}$$

$$P_{tot}^{1} = \sqrt{2 \cdot 733.766^2} = 1037.701 \; N \,. \tag{5.42}$$

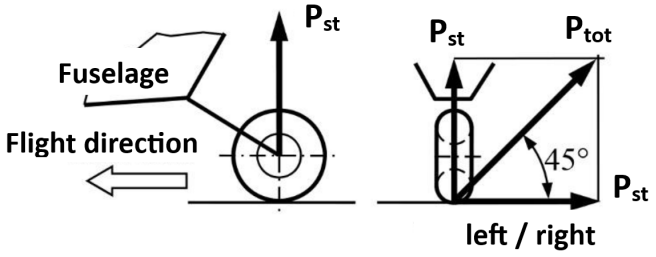

Figure 33: Side load schematic [2]

The reactions for the side load case for all configurations are summarized in Table 14.

Configuration	$\mathbf{P_{st}}$ [N]	$\mathbf{P_{tot}}$ [N]
1	733.766	1037.701
2	646.025	913.618
3	644.807	911.895

Table 14: Side load case reactions

5.3 Control Loads

The control system loads that have to be taken into account are the following:

1. UL 2 § 395: *"Each flight control system and its supporting structure must be designed for loads corresponding to at least 125% of the computed hinge moments of the movable control surface in the conditions prescribed in UL 2 § 423, UL 2 § 441 and UL 2 § 455."* [2, 37]

2. UL 2 § 397: *The rudder control system must be designed for a limit load of 90 daN acting forward on both the rudder pedals simultaneously.* [2]

The hinge moment is calculated in the subsequent sections. For the second case, the load acting on the rudder's control horn equals the load transferred by control cables from the rudder pedals. The load in the control cable was determined in Daniel Vysocký's thesis [38]. The limit load transferred by a cable when a 90 daN force is applied by the pilot is $F_c = 3222.2\ N$. [38]

6 Preliminary Design Using Analytical Methods

The calculations are performed for the two manufacturing methods mentioned in Section 4. The designs will differ in the safety factors used for the calculations. The additional safety factor for composite structures, beyond the standard safety factor of 1.5, ranges between 1 and 1.5. To be able to use the additional safety factor of 1, extensive material tests would have to be done and strict quality control would have to be employed during manufacturing. Usually, the additional safety factor of 1.25 is used for prepreg-based structures and 1.5 for hand-wetted structures. Therefore, a total safety factor of 1.875 is used for the design that uses prepreg materials (superscript 1 is used to mark related properties and physical quantities), and 2.25 is used for the design made of hand-wetted plies (superscript 2).

To calculate the inner stress resultants, the rudder is idealized as a beam whose length equals the rudder's span. The supports are located at the positions of the rudder's hinges (shown in Figure 34). Hinge 1 is idealized as a pin support because it transfers both vertical and horizontal loads, while hinge 2 is idealized as a roller support to maintain the structure's static determinacy.

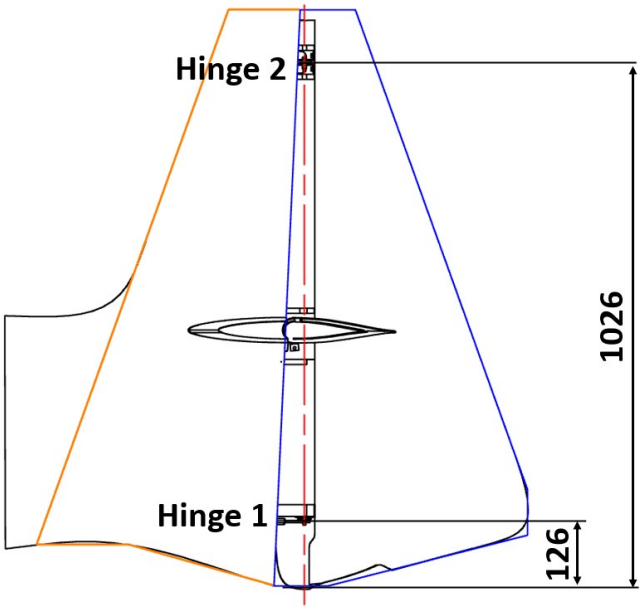

Figure 34: Location of hinges

6.1 Stress Resultants from Aerodynamic Loads

The maneuvering load is the critical aerodynamic load for the rudder design, as mentioned previously. Therefore, the stress resultants are calculated for this case. The stress resultants are determined directly for the ultimate load due to the linear stress-strain behavior of composite materials, which do not exhibit significant yielding characteristics.

The distributed ultimate load is calculated using the following formula:

$$\begin{aligned} q^1_{m_u} &= 1.875 \cdot q_m \ , \\ q^2_{m_u} &= 2.25 \cdot q_m \ . \end{aligned} \tag{6.1}$$

The reactions in the hinges have to be calculated. The total force developed by the distributed load is:

$$Q^{1,2}_{m_u} = \int_0^L q^{1,2}_{m_u}(z)\, dz \ . \tag{6.2}$$

Subsequently the location of point of action POA_Q of $Q^{1,2}_{m_u}$ was calculated. The reactions in the hinges may be calculated as the positions of the hinges are known ($hinge1 = 126\ mm$ and $hinge2 = 1026\ mm$):

$$\begin{aligned} R^{1,2}_{h1} &= Q^{1,2}_{m_u} \cdot \frac{b}{l} \ , \\ R^{1,2}_{h2} &= Q^{1,2}_{m_u} \cdot \frac{a}{l} \ , \end{aligned} \tag{6.3}$$

where:

$a = POA_Q - hinge1 = 0.465 - 0.126 = 0.339\ m$,
$b = hinge2 - POA_Q = 1.026 - 0.465 = 0.561\ m$,
$l = a + b = 0.339 + 0.561 = 0.9\ m$.

The reactions are:

$$\begin{aligned} R^1_{h1} = 706.47\ N\ ;\ R^1_{h2} = 426.90\ N \ , \\ R^2_{h1} = 847.76\ N\ ;\ R^2_{h2} = 512.29\ N \ . \end{aligned}$$

The shear force can now be calculated. The beam is divided into three sections and the shear force distribution in these sections is calculated:

$$
\begin{aligned}
&for\ z \in \langle 0; hinge1 \rangle :\\
&\qquad S^{1,2}(z) = \int_0^z q_{m_u}^{1,2}(z)\, dz\ ,\\
&for\ z \in \langle hinge1; hinge2 \rangle :\\
&\qquad S^{1,2}(z) = \int_0^z q_{m_u}^{1,2}(z)\, dz - R_{h1}^{1,2}\ ,\\
&for\ z \in \langle hinge2; end \rangle :\\
&\qquad S^{1,2}(z) = \int_0^z q_{m_u}^{1,2}(z)\, dz - R_{h1}^{1,2} - R_{h2}^{1,2}\ .
\end{aligned}
\tag{6.4}
$$

The shear force distribution for both designs is depicted in Figure 35.

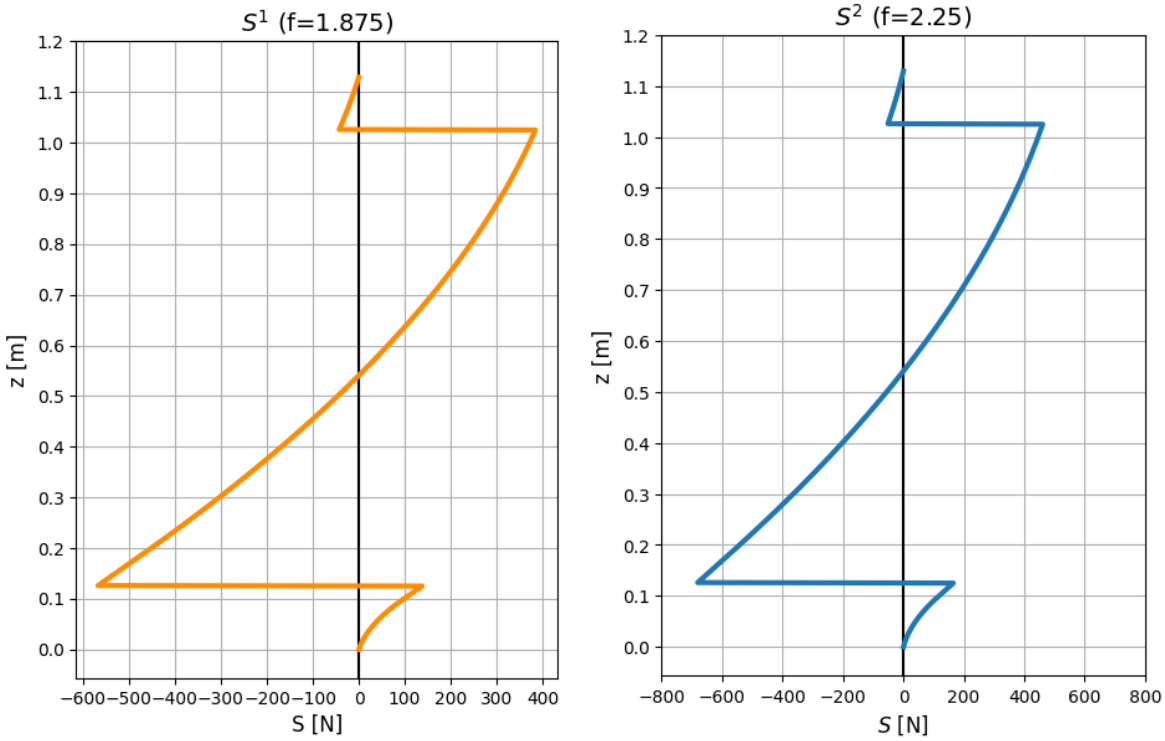

Figure 35: Shear force distribution

The bending moment distribution is assessed by integrating the shear force distribution as presented in Equation 6.5. The distribution is plotted in Figure 36.

$$
M_b^{1,2}(z) = \int_0^z S^{1,2}(z)\, dz \tag{6.5}
$$

To calculate the distribution of torsional moment relative to the rudder's axis of rotation, we begin by determining the total torsional moment that must be transferred by the control

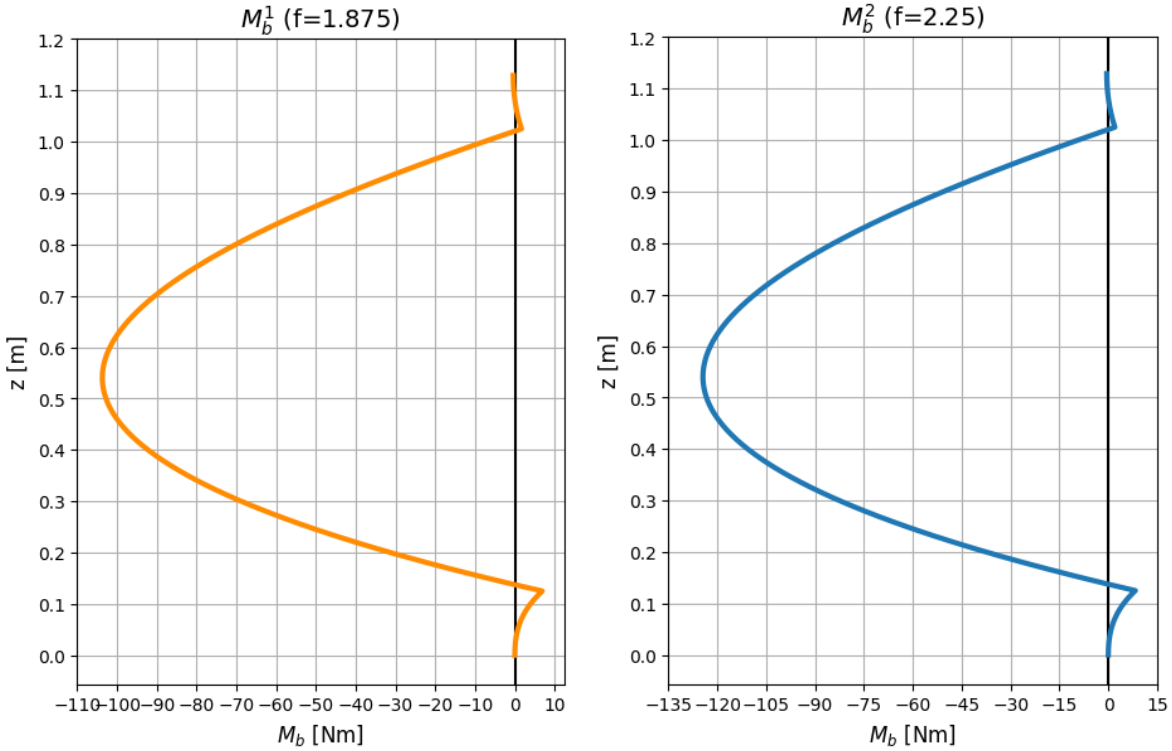

Figure 36: Bending moment distribution

horn to the rudder control cable using Equation 6.6. Since the control horn is part of hinge 1, the reaction necessary to counteract this torsional moment is present at this location. The distance of the cable attachment from the axis of rotation is 35 mm, but the maximum force occurs during full deflection of the rudder, as the lever arm decreases. The maximum deflection of the rudder is 23° [38], and the reaction force acting on the cable attachment is calculated using Equation 6.7.

To determine the torsional moment distribution, the beam is divided into two sections, and the torsional moment is calculated using Equation 6.8. The resulting distribution is plotted in Figure 37

$$\begin{aligned} M_{t_{total}}^{1,2} &= \int_0^L q_{m_u}^{1,2}(z) \cdot x_{q_m}(z)\, dz \\ M_{t_{total}}^{1} &= 92.898\ Nm \\ M_{t_{total}}^{2} &= 111.478\ Nm \end{aligned} \tag{6.6}$$

$$\begin{aligned} R_t^1 &= \frac{92.898}{0.035 \cdot \cos 23^\circ} = 2883.447\ N \\ R_t^2 &= \frac{111.478}{0.035 \cdot \cos 23^\circ} = 3460.136\ N \end{aligned} \tag{6.7}$$

$$
\begin{aligned}
&for\ z \in \langle 0; hinge1 \rangle : \\
&\qquad M_t^{1,2}(z) = \int_0^z q_{m_u}^{1,2}(z) \cdot x_{q_m}(z)\, dz\ , \\
&for\ z \in \langle hinge1; end \rangle : \\
&\qquad M_t^{1,2}(z) = \int_0^z q_{m_u}^{1,2}(z) \cdot x_{q_m}(z)\, dz - M_{t_{total}}^{1,2}\ .
\end{aligned}
\tag{6.8}
$$

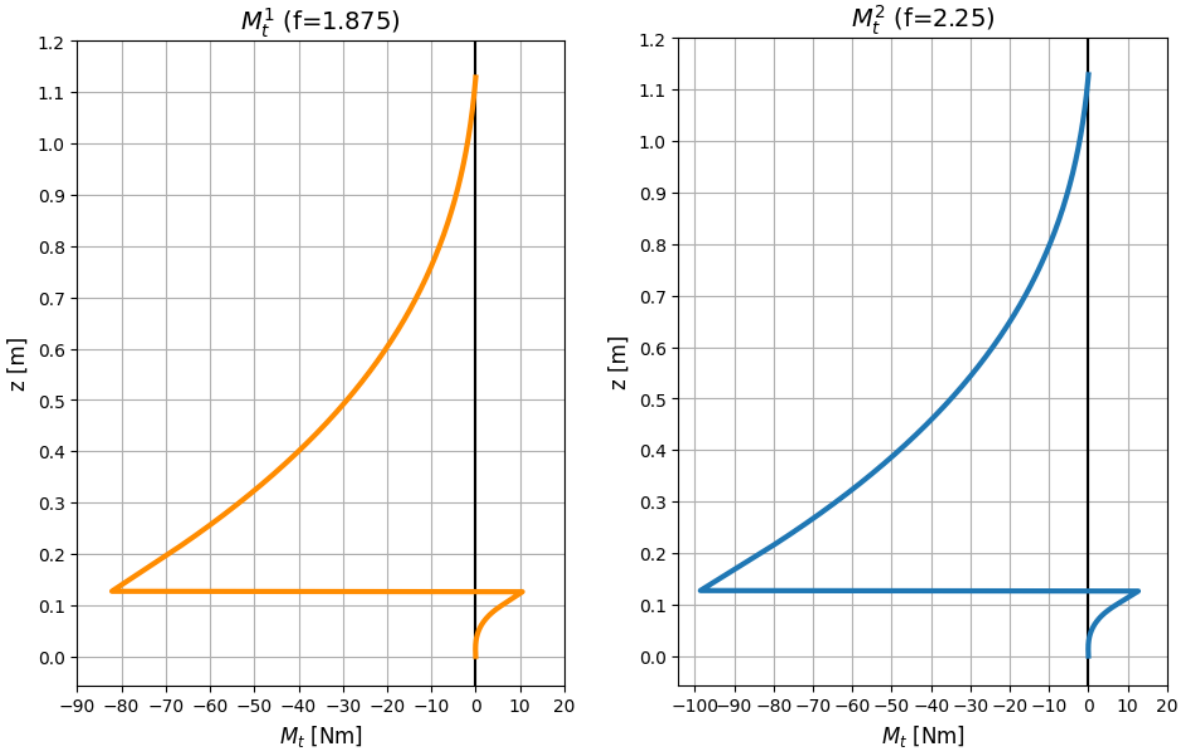

Figure 37: Torsional moment distribution relative to the rudder's rotational axis

6.2 Stress Resultants from Ground Loads

In this section, we determine the stress resultants for the three ground load cases. The angle between the aircraft's longitudinal axis and the ground is 15°. The ground loads are resolved into vertical and horizontal components to simplify further calculations. The position of the tail wheel and the point of contact with the ground in reference to the expected position of the spar and hinges are illustrated in Figure 38. Bending moments in the xz-plane are not calculated because of the high area moment of inertia, resulting in low stresses, and also to simplify the calculations.

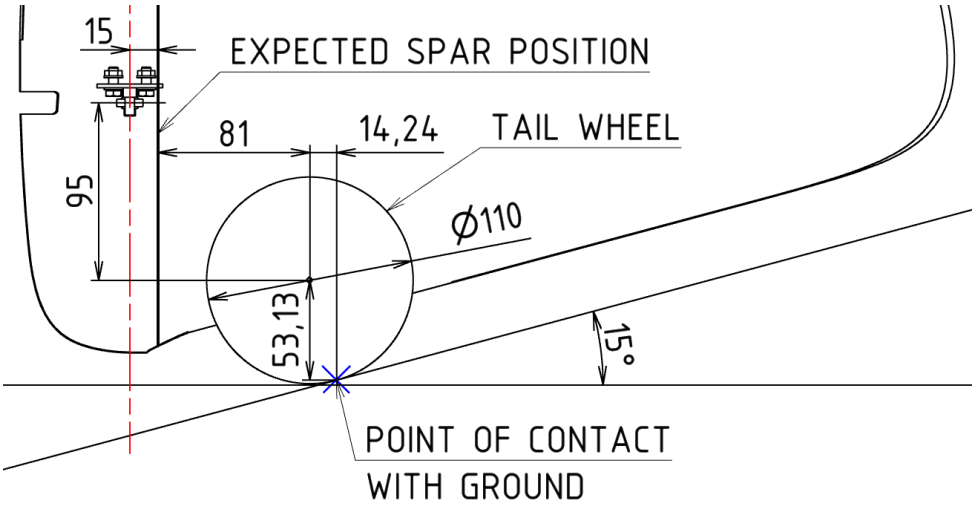

Figure 38: Tail wheel position

6.2.1 Tail-down Landing

The reactions from the tail-down landing are shown in Figure 39. The reactions can be moved to the tail wheel's center where the tail wheel is attached to the rudder as the moments caused by the reactions are in equilibrium in reference to the tail wheel's center.

The ultimate loads for the tail-down landing are the following:

$$\begin{aligned} F_{T1}^{1} &= 1.875 \cdot F_T = 1.875 \cdot 2424.197 = 4545.369\ N\ , \\ F_{T1}^{2} &= 2.25 \cdot F_T = 2.25 \cdot 2424.197 = 5454.443\ N\ . \end{aligned} \tag{6.9}$$

The vertical and horizontal components are calculated:

$$\begin{aligned} F_{T1}^{vert\ 1,2} &= F_{T1}^{1,2} \cdot \cos 15^\circ\ , \\ F_{T1}^{hor\ 1,2} &= F_{T1}^{1,2} \cdot \sin 15^\circ\ , \end{aligned} \tag{6.10}$$

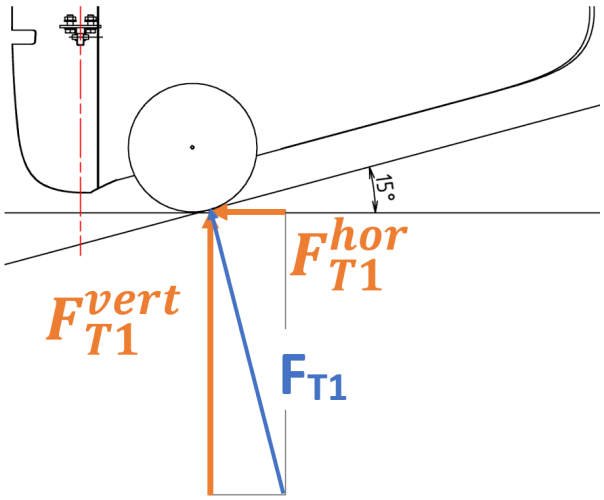

Figure 39: Tail-down landing reactions

$$F_{T1}^{vert\ 1} = 4390.49\ N\ ;\ F_{T1}^{hor\ 1} = 1176.428\ N\ ,$$
$$F_{T1}^{vert\ 2} = 5268.588\ N\ ;\ F_{T1}^{hor\ 2} = 1411.714\ N\ .$$

The reactions in the hinges can be calculated using Equation 6.11. The orientation of the reactions and necessary dimensions are shown in Figure 40.

$$\begin{aligned} R_{h1}^{hor\ 1,2} &= F_{T1}^{hor\ 1,2} + F_{T1}^{hor\ 1,2} \cdot \frac{v}{l} - F_{T1}^{vert\ 1,2} \cdot \frac{h}{l} \\ R_{h2}^{hor\ 1,2} &= -F_{T1}^{hor\ 1,2} \cdot \frac{v}{l} + F_{T1}^{vert\ 1,2} \cdot \frac{h}{l} \\ R_{h1}^{ver\ 1,2} &= F_{T1}^{vert\ 1,2} \end{aligned} \tag{6.11}$$

The distribution of shear force acting in the x-direction is shown in Figure 41 and the reactions in the hinges are:

$$R_{h1}^{hor\ 1} = 832.288\ N\ ;\ R_{h2}^{hor\ 1} = 344.14\ N\ ;\ R_{h1}^{ver\ 1} = 4390.49\ N\ ,$$
$$R_{h1}^{hor\ 2} = 998.745\ N\ ;\ R_{h2}^{hor\ 2} = 412.968\ N\ ;\ R_{h1}^{ver\ 2} = 5268.588\ N\ .$$

6.2.2 Obstruction Load

The principle of calculations is the same as for the tail-down landing case. The total ultimate load is identical to the ultimate load for the tail-down landing case. The load direction is depicted in Figure 42, where it is evident that the load direction is at a 60° angle from the horizontal.

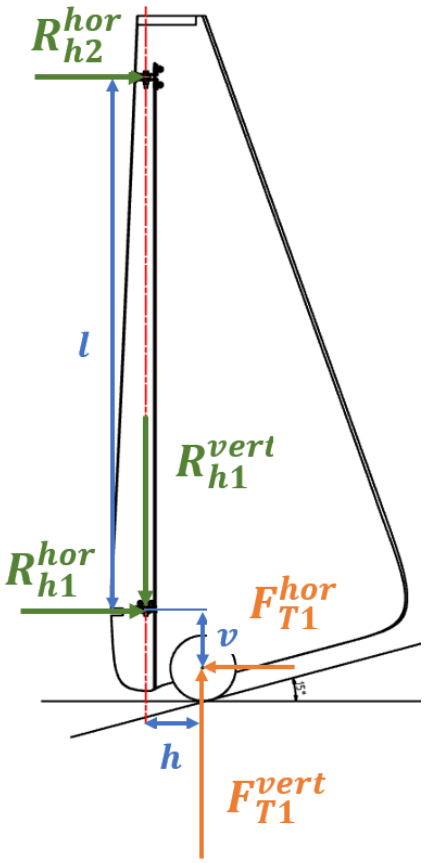

Figure 40: Hinge reactions

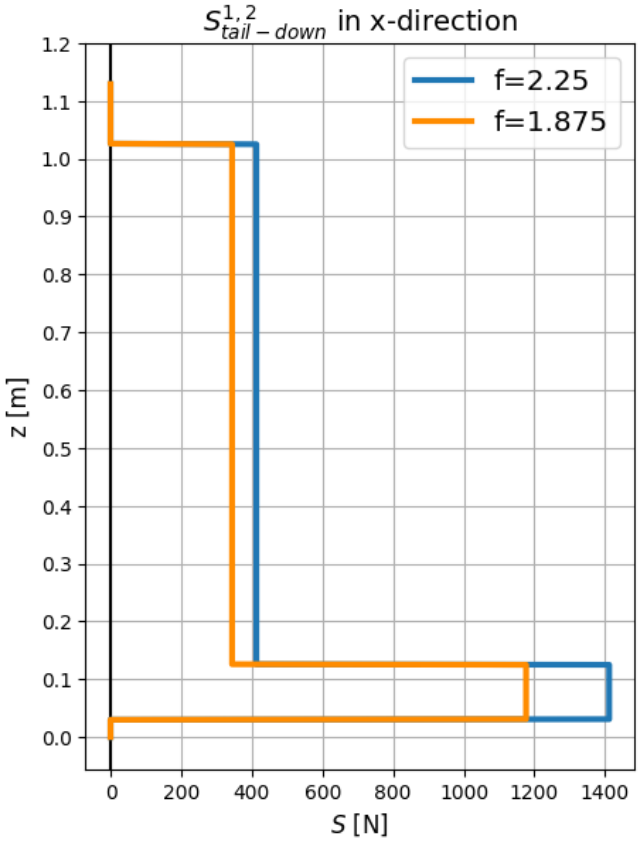

Figure 41: Shear force distribution for tail-down landing

The vertical and horizontal components are calculated, and the horizontal reaction is multiplied by -1 to stay consistent with the reference frame defined in Figure 40:

$$\begin{aligned} F_{T2}^{vert\ 1,2} &= F_{T1}^{1,2} \cdot \sin 60^\circ \ , \\ F_{T2}^{hor\ 1,2} &= -F_{T1}^{1,2} \cdot \cos 60^\circ \ , \end{aligned} \tag{6.12}$$

$$\begin{aligned} F_{T2}^{vert\ 1} &= 3936.405\ N\ ;\ F_{T2}^{hor\ 1} = -2272.685\ N\ , \\ F_{T2}^{vert\ 2} &= 4723.686\ N\ ;\ F_{T2}^{hor\ 2} = -2727.222\ N\ . \end{aligned}$$

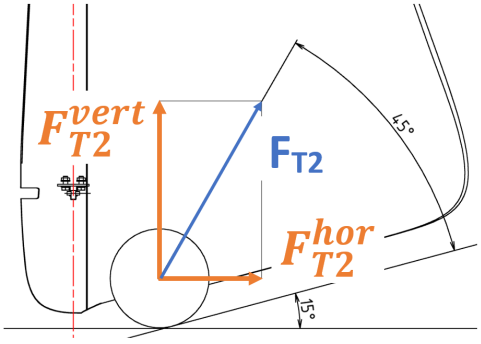

Figure 42: Obstruction load reactions

The reactions in the hinges are calculated analogously to Equation 6.11. The shear force distribution is shown in Figure 43 and the reactions in the hinges are:

$$R_{h1}^{hor\ 1} = -2932.462\ N\ ;\ R_{h2}^{hor\ 1} = 659.778\ N\ ;\ R_{h1}^{ver\ 1} = 3936.405\ N\ ,$$
$$R_{h1}^{hor\ 2} = -3518.955\ N\ ;\ R_{h2}^{hor\ 2} = 791.733\ N\ ;\ R_{h1}^{ver\ 2} = 4723.686\ N\ .$$

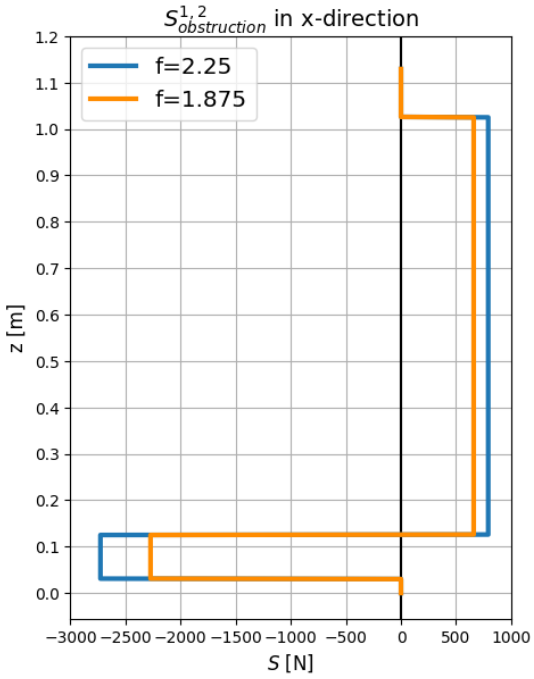

Figure 43: Shear force distribution for the obstruction case

6.2.3 Side Load

For the side load case, a lateral reaction is present in addition to the vertical and horizontal reactions as shown in Figure 44. The ultimate static load is the following:

$$\begin{aligned} P_{st}^{1} &= 1.875 \cdot P_{st} = 1.875 \cdot 733.766 = 1375.932\ N\ , \\ P_{st}^{2} &= 2.25 \cdot P_{st} = 2.25 \cdot 733.766 = 1594.718\ N\ . \end{aligned} \tag{6.13}$$

$$\begin{aligned} P_{st}^{vert\ 1,2} &= P_{st}^{1,2} \cdot \cos 15^{\circ}\ , \\ P_{st}^{hor\ 1,2} &= P_{st}^{1,2} \cdot \sin 15^{\circ}\ , \end{aligned} \tag{6.14}$$

$$P_{st}^{vert\ 1} = 1328.932\ N\ ;\ P_{st}^{hor\ 1} = 356.086\ N\ ,$$
$$P_{st}^{vert\ 2} = 1540.718\ N\ ;\ P_{st}^{hor\ 2} = 427.303\ N\ .$$

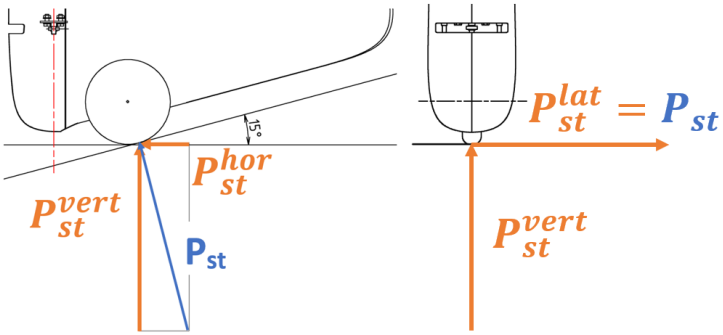

Figure 44: Side load reactions

The load in the side load case acts both in x and y directions, so the reactions in the hinges also have two components:

$$
\begin{aligned}
&R_{h1}^{hor-x\ 1} = 252.85\ N\ ;\ R_{h1}^{hor-y\ 1} = 1520.39\ N\ ;\ R_{h1}^{ver\ 1} = 1328.93\ N\ ,\\
&R_{h2}^{hor-x\ 1} = 103.24\ N\ ;\ R_{h2}^{hor-y\ 1} = -144.46\ N\ ,\\
&R_{h1}^{hor-x\ 2} = -303.41\ N\ ;\ R_{h1}^{hor-y\ 2} = 1762.15\ N\ ;\ R_{h1}^{ver\ 2} = 1540.72\ N\ ,\\
&R_{h2}^{hor-x\ 2} = -123.89\ N\ ;\ R_{h2}^{hor-y\ 2} = -167.43\ N\ .
\end{aligned}
$$

The torsional moment is calculated by multiplying the lateral load by the perpendicular distance to the axis of rotation:

$$M_t^{1,2} = P_{st}^{1,2} \cdot 0.015 + 0.081 + 0.01424\ , \tag{6.15}$$

$$
\begin{aligned}
M_t^1 &= 151.669\ Nm\ ,\\
M_t^2 &= 182.003\ Nm\ .
\end{aligned}
$$

This torsional moment acts in the area between the wheel attachment and hinge 1 where the control horn is located (Figure 45). The reaction on the control horn (cable attachment) is calculated by dividing the moment around the rotational axis by the arm of the control horn:

$$R_t^{1,2} = M_t^{1,2}/0.035\ , \tag{6.16}$$

$$
\begin{aligned}
R_t^1 &= 4333.412\ N\ ,\\
R_t^2 &= 5200.095\ N\ .
\end{aligned}
$$

The shear forces and bending moment for the side load case are calculated analogously to the previous sections. The shear forces are graphed in Figure 46 and the bending moment is shown in Figure 45.

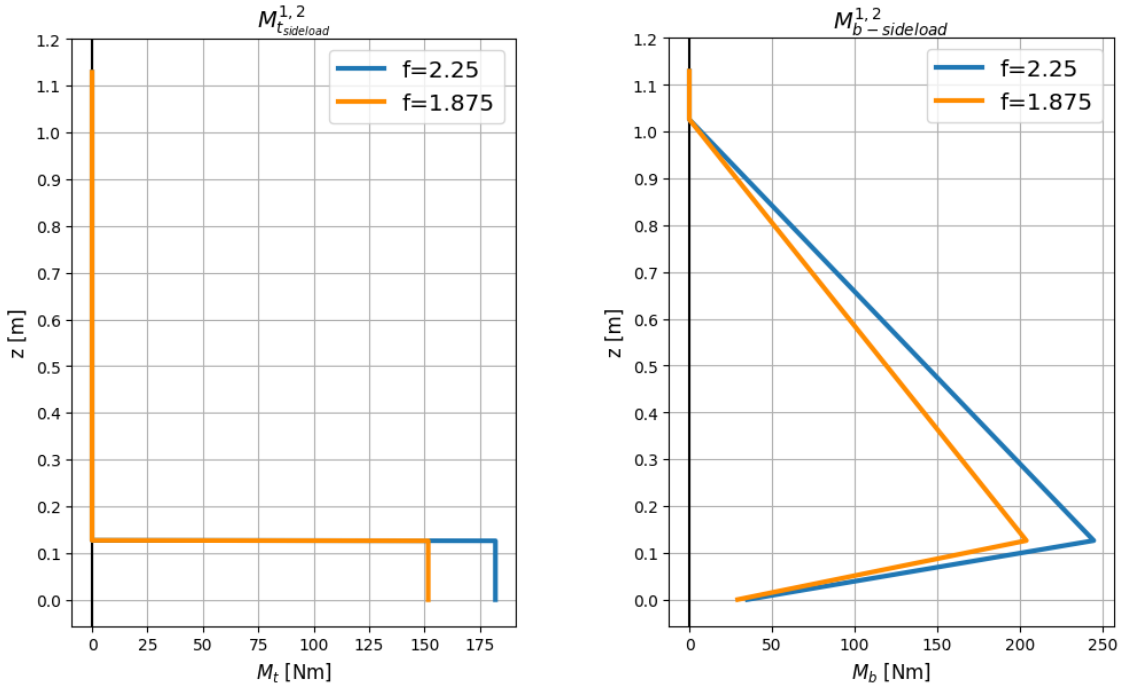

Figure 45: Torsional and bending moment distribution for the side load case

The lateral force causes a moment which is then transferred to the wheel attachment by a force couple. Figure 47 shows the forces acting on the wheel attachment. The distance between the points where the wheel axle is attached to the attachment (marked as x) influences the magnitude of forces of the force couple. The value of x can be found so the force acting on the more loaded side of the attachment equals the force acting in the tail-down and obstruction cases. This can be put into an equation:

$$\frac{P_{st}^{1,2}}{2} + \frac{P_{st}^{1,2} \cdot v_{lat}}{x} = \frac{F_{T1}^{1,2}}{2} \ . \tag{6.17}$$

The x can be expressed as:

$$x = \frac{P_{st}^{1,2} \cdot v_{lat}}{\frac{F_{T1}^{1,2}}{2} - \frac{P_{st}^{1,2}}{2}} = 0.04612 \ m \ . \tag{6.18}$$

Therefore, the wheel attachment is designed such that the distance x is equal to or greater than 46.12 mm.

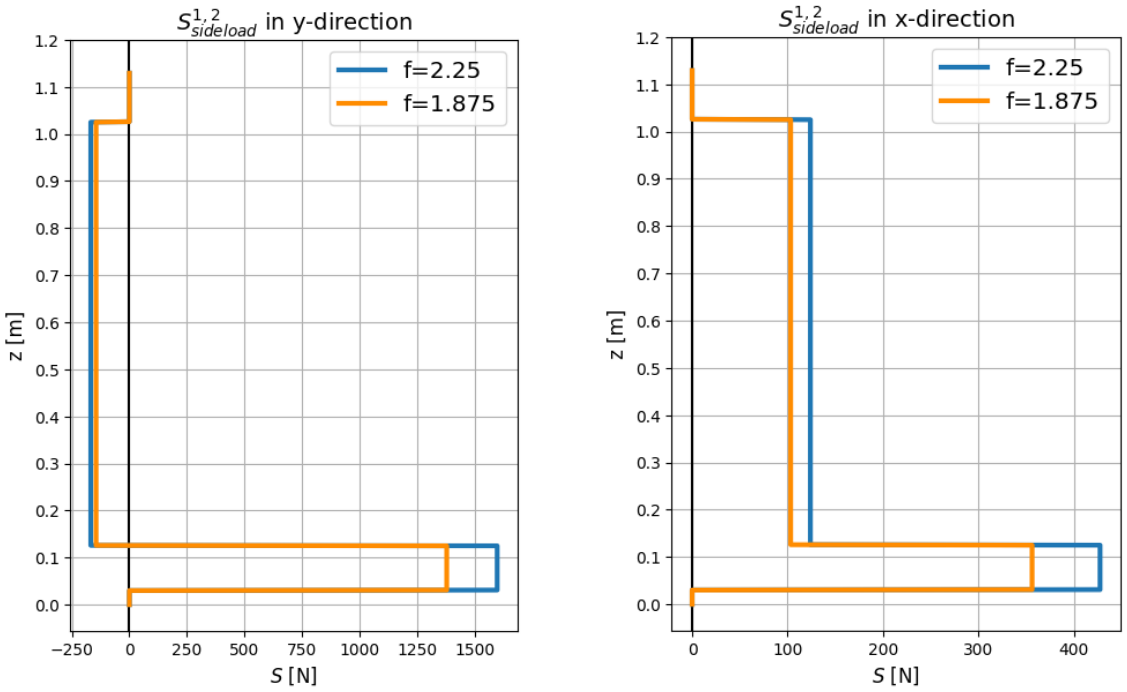

Figure 46: Shear force distribution for the side load case

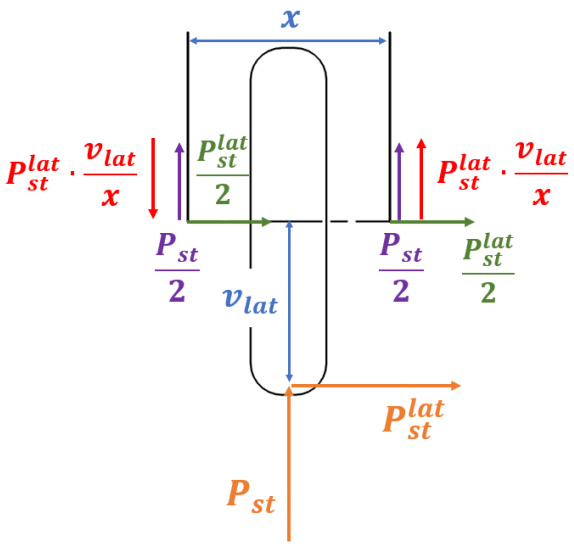

Figure 47: Forces acting on the wheel attachment

6.3 Design of Spar and Skin

The layup of the spar and skin is determined in this subsection using the Classical Laminate Theory (CLT). The layups are checked for intralaminar failures using the previously mentioned Tsai-Hill and Tsai-Wu criteria and for buckling failure. A sandwich structure is used which results in the necessity to consider two additional failure modes - wrinkling and crimping. The majority of formulas used in this section are taken from the book 'Design and Analysis of Composite Structures with Applications to Aerospace Structures' by Christos Kassapoglou [16]. When using formulas from other sources, the appropriate attribution is provided. All calculations were performed using Python code developed specifically for this application. The code's basic functionality is validated by comparing results with the eLAMX^2 software.

6.3.1 Overview of Classical Laminate Theory

"Classical laminate theory defines the response of a laminate with the following assumptions:

- *For two-dimensional plane stress analysis, the strain is constant through the thickness.*
- *For bending, the strain varies linearly through the thickness.*
- *The laminate is thin compared with its in-plane dimensions.*
- *Each layer is quasi-homogeneous and orthotropic.*
- *Displacements are small compared with the thickness.*
- *The behavior remains linear.*

With these assumptions satisfied, the laminate theory allows the response of a laminate to be calculated, engineering constants to be determined to substitute into standard formulas for stresses and deflections, and material properties of the laminate to be defined." [10]

The laminate is defined by its stacking sequence (layup). The stacking sequence is defined by the orientation of each ply which is given by angle θ relative to a reference axis $(-90° < \theta \leq +90°)$, as shown in Figure 48, and by the material type T used for the ply which is given in parentheses after the angle θ. The stacking sequence then is:

$$[\theta_1(T_1), \theta_2(T_2), \theta_3(T_3)...] \ ,$$

where θ_1, θ_2 and θ_3 are the angles of successive plies starting from the top of the laminate, and T_1, T_2 and T_3 are the material types of these plies. When fabric materials are used, the two fiber orientations in each ply can be given in parentheses, e.g. $[(0/90), (\pm 45)...]$. If there are successive plies with the same orientation and from the same material or if there are repetitive sections of the stacking sequence, the stacking sequence can be shortened by using subscript

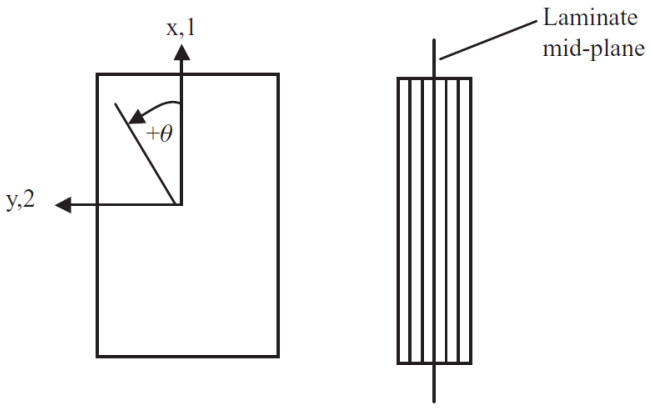

Figure 48: Definition of laminate axis and positive θ orientation [16]

which gives the number of the repetitive sections or plies. Subscript "s" is used when the layup is symmetric, if the number of plies is odd and half of the middle ply lies on one side of the midplane and half on the other, the middle ply is denoted with an overbar. Therefore: [16]

$$[0, 90, 30_3, \overline{45}]_S \text{ is the same as } [0, 90, 30, 30, 30, 45, 30, 30, 30, 90, 0] \ .$$

The constitutive equations are given only in two dimensions, as the out-of-plane stresses are negligible compared to the in-plane stresses of thin structures. [16] The process of calculating the properties of a laminate and stresses in each ply is described further.

The stiffness matrix in a principal coordinate system (coordinate system of the individual ply where the direction "1" is aligned with the main fiber direction) for each ply must be created first:

$$\mathbf{Q} = \begin{bmatrix} Q_{11} & Q_{12} & 0 \\ Q_{21} & Q_{22} & 0 \\ 0 & 0 & Q_{66} \end{bmatrix} = \begin{bmatrix} E_1 Q^{-1} & \nu_{12} E_2 Q^{-1} & 0 \\ \nu_{21} E_1 Q^{-1} & E_2 Q^{-1} & 0 \\ 0 & 0 & G_{12} \end{bmatrix} , \tag{6.19}$$

where:

$E_1, E_2, G_{12}, \nu_{12}$ *are elastic properties of material used for the ply* ,
$\nu_{21} = \nu_{12} \frac{E_2}{E_1}$,
$Q = 1 - \nu_{12}\nu_{21}$.

This stiffness matrix $\mathbf{Q}$ must be transformed into the global coordinates using transformational matrices $\mathbf{T}_\sigma$ and $\mathbf{T}_\varepsilon$ which constituents are dependent on angle θ of each ply:

$$\mathbf{T}_\sigma = \begin{bmatrix} m^2 & n^2 & 2mn \\ n^2 & m^2 & -2mn \\ -mn & mn & m^2 - n^2 \end{bmatrix} , \tag{6.20}$$

$$\mathbf{T}_{\varepsilon} = \begin{bmatrix} m^2 & n^2 & mn \\ n^2 & m^2 & -mn \\ -2mn & 2mn & m^2 - n^2 \end{bmatrix} , \tag{6.21}$$

where:

$m = \cos\theta$,
$n = \sin\theta$.

The stiffness matrix in the global coordinate system is defined as follows:

$$\mathbf{Q}' = \begin{bmatrix} Q_{xx} & Q_{xy} & Q_{xs} \\ Q_{yx} & Q_{yy} & Q_{ys} \\ Q_{sx} & Q_{sy} & Q_{ss} \end{bmatrix} = \mathbf{T}_{\sigma}^{-1}\mathbf{Q}\mathbf{T}_{\varepsilon} . \tag{6.22}$$

When the stiffness matrices in the global coordinate system are calculated for all plies of the laminate, the elements of the ABD matrix are determined:

$$\begin{aligned} A_{ij} &= \sum_{k=1}^{n} Q_{ij}^{\prime(k)} \left(z_k - z_{k-1}\right) , \\ B_{ij} &= \frac{1}{2}\sum_{k=1}^{n} Q_{ij}^{\prime(k)} \left(z_k^2 - z_{k-1}^2\right) , \\ D_{ij} &= \frac{1}{3}\sum_{k=1}^{n} Q_{ij}^{\prime(k)} \left(z_k^3 - z_{k-1}^3\right) , \end{aligned} \tag{6.23}$$

where:

$i, j = x, y, s$,
$k =$ *index of ply* ,
$n =$ *number of plies in the laminate* ,
$z =$ *z-coordinate of ply face as per Figure 49* .

The A_{ij} terms create the extensional stiffness matrix, B_{ij} terms create the coupling stiffness matrix, and D_{ij} terms create the flexural stiffness matrix. [16]

The ABD matrix is created by combining the three matrices:

$$\mathbf{ABD} = \begin{bmatrix} \mathbf{A} & \mathbf{B} \\ \mathbf{B} & \mathbf{D} \end{bmatrix} = \begin{bmatrix} A_{xx} & A_{xy} & A_{xs} & B_{xx} & B_{xy} & B_{xs} \\ A_{xy} & A_{yy} & A_{ys} & B_{xy} & B_{yy} & B_{ys} \\ A_{xs} & A_{ys} & A_{ss} & B_{xs} & B_{ys} & B_{ss} \\ B_{xx} & B_{xy} & B_{xs} & D_{xx} & D_{xy} & D_{xs} \\ B_{xy} & B_{yy} & B_{ys} & D_{xy} & D_{yy} & D_{ys} \\ B_{xs} & B_{ys} & B_{ss} & D_{xs} & D_{ys} & D_{ss} \end{bmatrix} . \tag{6.24}$$

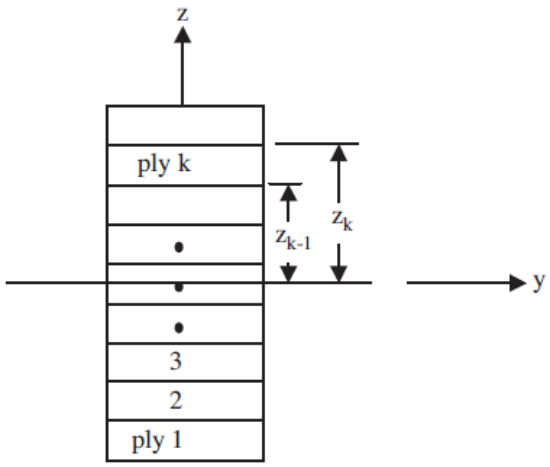

Figure 49: Ply numbering and z-coordinate system [16]

The engineering constants are determined from the ABD matrix. The equations are valid both for symmetrical and unsymmetrical laminates:

$$\begin{aligned}
E_{x_m} &= \frac{1}{h(\mathbf{ABD}^{-1})_{11}} \quad ; \quad E_{x_b} = \frac{12}{h^3(\mathbf{ABD}^{-1})_{44}} \,, \\
E_{y_m} &= \frac{1}{h(\mathbf{ABD}^{-1})_{22}} \quad ; \quad E_{y_b} = \frac{12}{h^3(\mathbf{ABD}^{-1})_{55}} \,, \\
G_{xy_m} &= \frac{1}{h(\mathbf{ABD}^{-1})_{33}} \quad ; \quad G_{xy_b} = \frac{12}{h^3(\mathbf{ABD}^{-1})_{66}} \,, \\
\nu_{xy_m} &= -\frac{(\mathbf{ABD}^{-1})_{12}}{(\mathbf{ABD}^{-1})_{11}} \quad ; \quad \nu_{xy_b} = -\frac{(\mathbf{ABD}^{-1})_{45}}{(\mathbf{ABD}^{-1})_{44}} \,, \\
\nu_{yx_m} &= -\frac{(\mathbf{ABD}^{-1})_{12}}{(\mathbf{ABD}^{-1})_{22}} \quad ; \quad \nu_{yx_b} = -\frac{(\mathbf{ABD}^{-1})_{45}}{(\mathbf{ABD}^{-1})_{55}} \,,
\end{aligned} \tag{6.25}$$

where:

$m =$ *membrane (in-plane) properties* ,

$b =$ *bending (flexural) properties* .

When the force and moment resultants acting on the laminate are known, membrane strains ($\varepsilon_x^0, \varepsilon_y^0, \varepsilon_s^0$) and curvatures ($\kappa_x, \kappa_y, \kappa_s$) of the laminate may be calculated using Equation 6.26. The force and moment resultants inputted into the equation are force per unit width and moment per unit width and their positive directions are shown in Figure 50.

$$\begin{Bmatrix} \varepsilon_x^0 \\ \varepsilon_y^0 \\ \varepsilon_s^0 \\ \kappa_x \\ \kappa_y \\ \kappa_s \end{Bmatrix} = \begin{bmatrix} A_{xx} & A_{xy} & A_{xs} & B_{xx} & B_{xy} & B_{xs} \\ A_{xy} & A_{yy} & A_{ys} & B_{xy} & B_{yy} & B_{ys} \\ A_{xs} & A_{ys} & A_{ss} & B_{xs} & B_{ys} & B_{ss} \\ B_{xx} & B_{xy} & B_{xs} & D_{xx} & D_{xy} & D_{xs} \\ B_{xy} & B_{yy} & B_{ys} & D_{xy} & D_{yy} & D_{ys} \\ B_{xs} & B_{ys} & B_{ss} & D_{xs} & D_{ys} & D_{ss} \end{bmatrix} \begin{Bmatrix} N_x \\ N_y \\ N_s \\ M_x \\ M_y \\ M_s \end{Bmatrix} \tag{6.26}$$

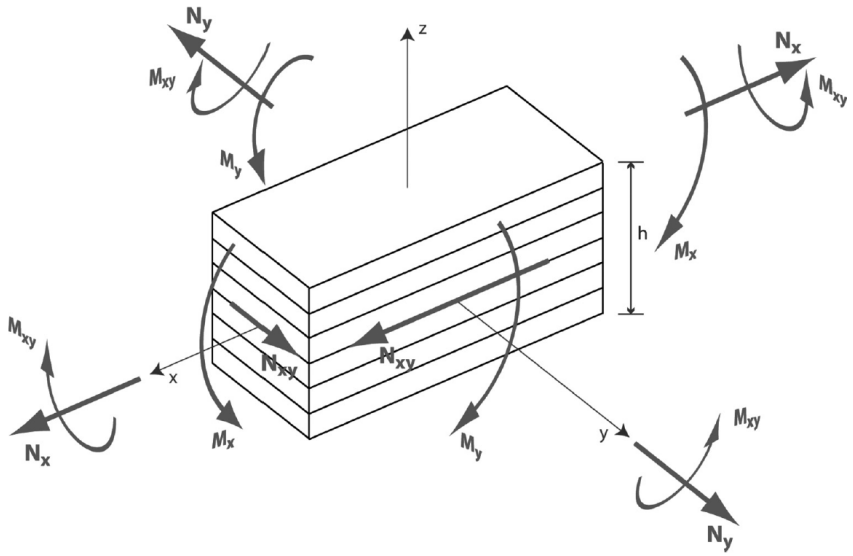

Figure 50: Force and moment resultants for CLT [16]

The stresses in the global coordinate system are calculated by multiplying the stiffness matrix with the total strain, computed by a superposition of the membrane strains and curvatures as per Equation 6.27. The stresses must be evaluated for both ply faces because the strains, and therefore the stresses may differ due to the curvature of the laminate.

$$\begin{Bmatrix} \sigma_x \\ \sigma_y \\ \sigma_s \end{Bmatrix}^k = \begin{bmatrix} Q_{xx} & Q_{xy} & Q_{xs} \\ Q_{yx} & Q_{yy} & Q_{ys} \\ Q_{sx} & Q_{sy} & Q_{ss} \end{bmatrix}^k \left[\begin{Bmatrix} \varepsilon_x^0 \\ \varepsilon_y^0 \\ \varepsilon_s^0 \end{Bmatrix} + z \begin{Bmatrix} \kappa_x \\ \kappa_y \\ \kappa_s \end{Bmatrix} \right] \tag{6.27}$$

The obtained stresses are in the global coordinate system and they must be transformed to the principal coordinate system first using the following equation:

$$\begin{Bmatrix} \sigma_1 \\ \sigma_2 \\ \sigma_6 \end{Bmatrix}^k = \mathbf{T}_\sigma^k \begin{Bmatrix} \sigma_x \\ \sigma_y \\ \sigma_s \end{Bmatrix}^k . \tag{6.28}$$

The stresses in the principal coordinate system can then be inputted into the chosen failure theories to evaluate if any plies of the laminate fail.

6.3.2 Shear Flow Calculation

The torsional moments in sections 6.1 and 6.2.3 were calculated in reference to the rotational axis of the rudder to asses the loads that will be acting on the control horn. The torsional moment about the elastic axis (shear center) must be computed for the skin and spar design. The rudder is assumed to have one closed cell behind the spar which transfers the torsional moment via shear flow as shown in Figure 51. The position of the elastic axis is calculated using Equation 6.29 [39] and it is dependent on the spanwise coordinate z.

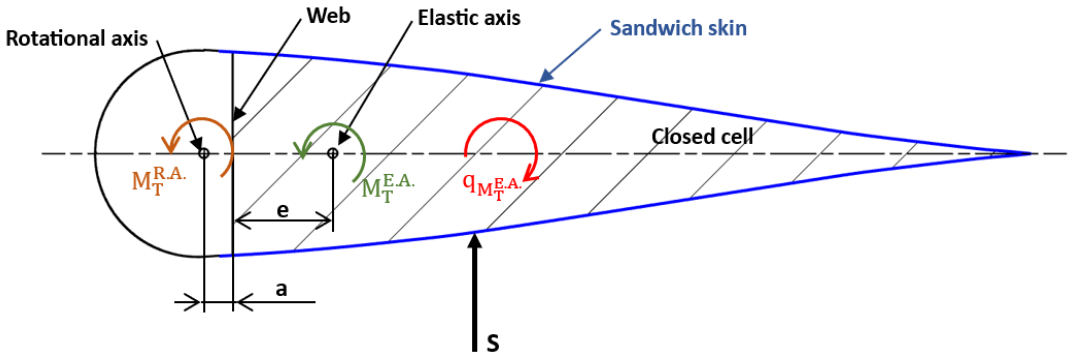

Figure 51: One cell rudder section

$$e(z) = \frac{2A_c(z)}{l_w(z)} \frac{1}{1 + \frac{l_s(z) \cdot h_w(z) \cdot G_w(z)}{l_w(z) \cdot h_s(z) \cdot G_s(z)}}, \tag{6.29}$$

where:

A_c = *area of the cell* ,

h_s, h_w = *thickness of skin and web* ,

l_s, l_w = *perimeter length of skin and web* ,

G_s, G_w = *Shear modulus of skin and web* .

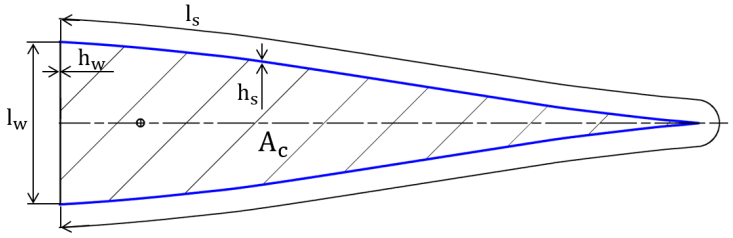

Figure 52: Cell dimensions

The torsional moment around the elastic axis is calculated using Equation 6.30 and the resulting shear flow is calculated using Equation 6.31. [39]

$$M_T^{E.A.}(z) = M_T^{R.A.}(z) - S(z) \cdot (a + e(z)) \tag{6.30}$$

$$q_{M_T^{E.A.}}(z) = \frac{M_T^{E.A.}(z)}{2A_c(z)} \tag{6.31}$$

6.3.3 Effective Skin Width

Thanks to relatively low loads, the skin should be able to transfer both the shear flow and the tension/compression caused by the bending moment, leading to no need for a unidirectional carbon fiber flange. The skin can not transfer higher loads than the buckling load which causes the loss of stability. The skin and web are designed as sandwich structures with foam cores, so the wrinkling and crimping failure modes must be considered.

The buckling load is computed using an equation for a simply supported rectangular plate. The rudder's span is used as the plate's length and the diameter of the inscribed circle of the rudder (Figure 53) is used as the plate's width.

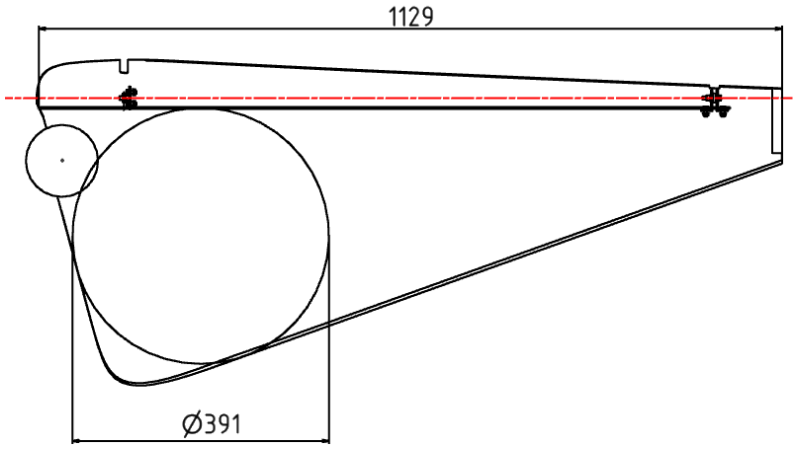

Figure 53: Dimensions for stability calculations

The following equation gives the buckling load of a simply supported plate under compression:

$$N_{bc} = \frac{\pi^2}{a^2}\left[D_{xx}m^2 + 2\left(D_{xy} + 2D_{ss}\right)(AR)^2 + D_{yy}\frac{(AR)^4}{m^2}\right] , \tag{6.32}$$

where:

$a =$ *length of the plate* ,
$AR = length/width$ *of the plate* ,
$m =$ *number of half-waves in the length direction* .

The number of half-waves m that minimizes the buckling load must be found and used for the computation. The buckling load prediction is non-conservative for sandwich structures and transverse shear effects must be accounted for. The buckling load with the transverse shear effect follows on the next page:

$$N_{xcrit} = \frac{N_{bc}}{1 + \dfrac{N_{bc}}{t_c G_c}} \ , \tag{6.33}$$

where:

$t_c =$ *core thickness* ,

$G_c =$ *shear modulus of the core* .

The following equation gives the buckling load of a simply supported plate under shear when $0.5 < length/width < 2$:

$$N_{bs}^{0.5-2} = \frac{\dfrac{\pi^4 b}{a^3}}{\sqrt{\dfrac{14.28}{D1^2} + \dfrac{40.96}{D1^{D2}} + \dfrac{40.96}{D1D3}}} \ , \tag{6.34}$$

where:

$$D1 = D_{xx} + D_{yy}\left(\frac{a}{b}\right)^4 + 2\left(D_{xy} + 2D_{ss}\right)\left(\frac{a}{b}\right)^2 \ ,$$

$$D2 = D_{xx} + 81D_{yy}\left(\frac{a}{b}\right)^4 + 18\left(D_{xy} + 2D_{ss}\right)\left(\frac{a}{b}\right)^2 \ ,$$

$$D3 = 81D_{xx} + D_{yy}\left(\frac{a}{b}\right)^4 + 18\left(D_{xy} + 2D_{ss}\right)\left(\frac{a}{b}\right)^2 \ ,$$

$b =$ *plate's width* .

The buckling load of a long rectangular plate (with aspect ratio $a/b = 0$ under shear (see Figure 54) can be calculated using Equation 6.35. It's important to note that b represents the longer dimension for the calculations involving the long plate.

$$N_{bs}^{0} = \frac{\pi^2}{2AR^2 a^2 \tan\alpha}\left[\begin{array}{l} D_{xx}\left(1 + 6AR^2\tan^2\alpha + AR^4\tan^4\alpha\right) \\ +2\left(D_{xy} + 2D_{ss}\right)\left(AR^2 + AR^4\tan^2\alpha\right) + D_{yy}AR^4 \end{array}\right] \tag{6.35}$$

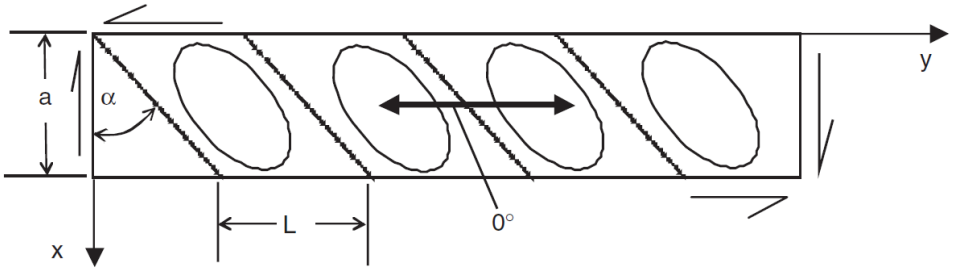

Figure 54: Buckling pattern in a long rectangular plate under shear [16]

The buckling load in Equation 6.35 is a function of angle α and aspect ratio AR. The values of $\tan\alpha$ and AR which minimize the right side of Equation 6.35 must be found. Differentiation gives us the following equations:

$$AR = \left[\frac{D_{xx}}{D_{xx}\tan^4\alpha + 2\left(D_{xy}+2D_{ss}\right)\tan^2\alpha + D_{yy}}\right]^{1/4} , \tag{6.36}$$

$$\begin{aligned} &3D_{xx}AR^4\tan^4\alpha + \left(6D_{xx}AR^2 + 2\left(D_{xy}+2D_{ss}\right)AR^4\right)\tan^2\alpha \\ &-\left(D_{xx} + 2\left(D_{xy}+2D_{ss}\right)AR^2 + D_{yy}AR^4\right) = 0 . \end{aligned} \tag{6.37}$$

Equations 6.38 and 6.37 are solved simultaneously and the results are then inputted into the Equation 6.35.

For plates with a/b ratios between $a/b = 0$ and $a/b = 0.5$ the buckling load is obtained by linearly interpolating between the result for those two ratios:

$$N_{bs} = \frac{N_{bs}^{0.5-2} - N_{bs}^{0}}{0.5}\frac{a}{b} + N_{bs}^{0} , \tag{6.38}$$

where:

$$\frac{a}{b} = \frac{width}{length} = \frac{391}{1129} = 0.346 .$$

The transverse shear effects must be accounted for in the same way as for the compression buckling. The buckling load of a sandwich composite plate under shear is therefore:

$$N_{xycrit} = \frac{N_{bs}}{1 + \dfrac{N_{bs}}{t_c G_c}} . \tag{6.39}$$

If the plate is subjected to both the compression and shear loads, the buckling failure envelope is given by Equation 6.40.

$$\frac{N_x}{N_{xcrit}} + \left(\frac{N_{xy}}{N_{xycrit}}\right)^2 = 1 \tag{6.40}$$

Wrinkling (depicted in Figure 55) is a local buckling phenomenon specific to sandwich plates which can occur under compression, shear, or combined loads. Critical load for the symmetric wrinkling under compression is assessed first. The portion of the core which deforms together with the facesheet z_c is:

$$z_c = 0.91 \cdot t_f \left(\frac{E_c E_f}{{G_c}^2}\right)^{1/3} , \tag{6.41}$$

where:

properties denoted by c are core properties and by f facesheet properties .

The critical symmetric wrinkling load of the sandwich depends on the core thickness:
if $z_c < \frac{t_c}{2}$:

$$N^s_{xwr} = 2 \cdot 0.43 \cdot t_f \left(E_c E_f G_c\right)^{1/3} \ , \tag{6.42}$$

if $z_c \geq \frac{t_c}{2}$:

$$N^s_{xwr} = 2 \cdot \frac{43}{91} \cdot \left(0.816 \sqrt{\frac{E_c E_f {t_f}^3}{t_c}} + G_c \frac{t_c}{6}\right) \ . \tag{6.43}$$

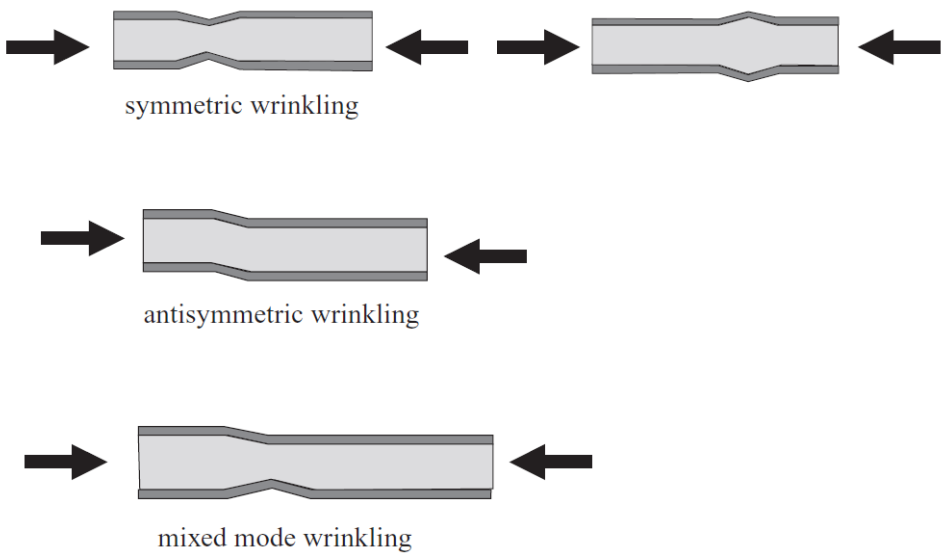

Figure 55: Wrinkling modes [16]

Determination of the critical load for the anti-symmetric wrinkling under compression follows:

$$z_c = \frac{3}{2} t_f \left(\frac{E_c E_f}{{G_c}^2}\right)^{1/3} \ , \tag{6.44}$$

if $z_c < \frac{t_c}{2}$:

$$N^a_{xwr} = 2 \cdot \frac{33}{51} \cdot \left(0.51 \cdot t_f \left(E_c E_f G_c\right)^{1/3} + G_c \frac{t_c}{3}\right) \ , \tag{6.45}$$

if $z_c \geq \frac{t_c}{2}$:

$$N^a_{xwr} = 2 \cdot \frac{33}{51} \cdot \left(0.59 \cdot \sqrt{\frac{E_c E_f}{t_c}} + 0.378 \cdot G_c t_c\right) \ . \tag{6.46}$$

The formulas used for the critical wrinkling loads differ from the ones used in the book [16].

The formulas given in the book are multiplied by 2 to get the critical wrinkling load of the whole sandwich rather than of only one facesheet and by a knockdown factor to account for possible core waviness, which value was given in lectures by Christos Kassapoglou [40].

The critical wrinkling load under compression N_{xwr} is given by the lower value between the symmetric and anti-symmetric cases. Determination of the critical wrinkling load under shear is identical to the compression wrinkling determination with the difference that the stacking sequence is rotated by 45° to align the sandwich with the compression portion of the shear load. For the wrinkling under combined compression and shear load, the failure envelope is determined analogously to Equation 6.40 to which the critical wrinkling loads are substituted. [16]

The last failure mode to be considered is sandwich crimping which occurs mainly in sandwich structures when a core with low shear stiffness is used. For isotropic core, the critical crimping loads under shear and compression are identical:

$$N_{xcrim} = N_{xycrim} = t_c G_c \ . \tag{6.47}$$

The failure envelope for combined crimping is again determined analogously to Equation 6.40.

The effective skin width must be determined to assess the load distribution between the skin and the web for some of the load cases. The maximal compressive load the skin can transfer without stability failure is the lowest of the compressive buckling, wrinkling, and crimping loads when the skin is also subjected to the shear flow, which can be derived from Equation 6.40:

$$\begin{aligned}
N_x^{max1}(z) &= \left(1 - \left(\frac{q_{M_T^{E.A.}}(z)}{N_{xycrit}}\right)^2\right) N_{xcrit} \ , \\
N_x^{max2}(z) &= \left(1 - \left(\frac{q_{M_T^{E.A.}}(z)}{N_{xywr}}\right)^2\right) N_{xwr} \ , \\
N_x^{max3}(z) &= \left(1 - \left(\frac{q_{M_T^{E.A.}}(z)}{N_{xycrim}}\right)^2\right) N_{xcrim} \ , \\
N_x^{max}(z) &= \min\left(N_x^{max1}(z); N_x^{max2}(z); N_x^{max3}(z)\right) \ .
\end{aligned} \tag{6.48}$$

The effective skin width is then given by the following equation:

$$b_{ef}(z) = \frac{N_x^{max}(z)}{N_{ult}^{comp}} \cdot b \ , \tag{6.49}$$

where:
N_{ult}^{comp} = *ultimate compressive strength of layup* ,
$b = 0.391$ *(width of plate for stability calculations)* .

The effective height h_{ef} of the spar created by the skin and the web (in Figure 56) and the width of the web b_{web} are calculated as follows:

$$\begin{aligned} h_{ef}(z) &= l_w(z) - b_{ef}(z)\sin 5^\circ - h_s(z) \ , \\ b_{web}(z) &= l_w(z) - 2 \cdot h_s(z) \ . \end{aligned} \tag{6.50}$$

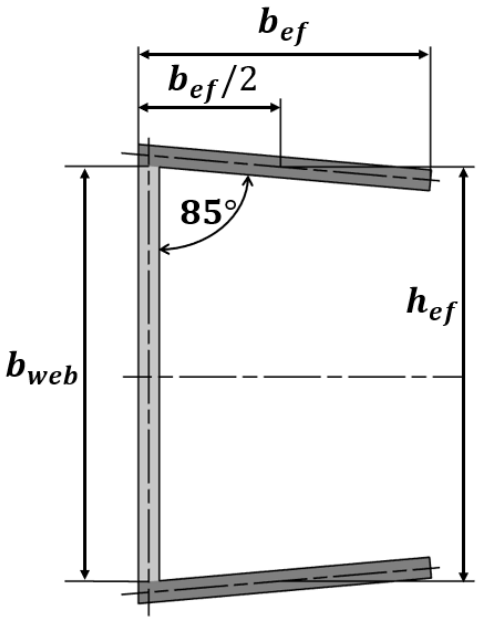

Figure 56: Cross section of the spar

6.3.4 Load Distribution

The load distribution between the skin and the web can now be worked out. The moment resultants in the CLT equations are equal to zero as bending moments are assumed to be transferred by compressive force on one side of the skin and tensile force on the other. It is assumed that the skin carries shear loads resulting from torsional moments, shear loads in the x-direction (as shown in Figure 23) due to ground loads, bending moments, and a portion of the compressive loads resulting from the vertical force component of the ground loads. The web carries the shear loads resulting from torsional moments, shear loads in the y-direction (as shown in Figure 23) due to ground loads, and a portion of the compressive loads resulting from the vertical force component of the ground loads.

The portions of the vertical load V which the skin (V_s) and web (V_w) carry are determined by their stiffness:

$$V_s = \frac{E_{x_m s} \cdot b_{ef} \cdot h_s}{2 \cdot E_{x_m s} \cdot b_{ef} \cdot h_s + E_{x_m w} \cdot b_{web} \cdot h_w} \cdot V \ ,$$
$$V_w = \frac{E_{x_m w} \cdot b_{web} \cdot h_w}{2 \cdot E_{x_m s} \cdot b_{ef} \cdot h_s + E_{x_m w} \cdot b_{web} \cdot h_w} \cdot V \ , \tag{6.51}$$

where:

$V = F_{T1}^{vert}$ *for the tail-down landing case* ,
$V = F_{T2}^{vert}$ *for the obstruction load case* ,
$V = P_{st}^{vert}$ *for the side-load case* .

The skin lies in the xz plane (as per Figure 23) and the reference axis of the skin, from which the angle θ is given, corresponds to the z-axis. Thus the loads acting in the z-direction in Figure 23 are inputted to force resultant N_x and the loads acting in the x-direction are inputted as N_y. The web lies in the yz plane with the reference axis also corresponding to the z-axis. Therefore, the loads acting in the z-direction are inputted as N_x and loads acting in the y-direction are inputted as N_y. The force resultants differ for $z \in \langle 0; hinge1 \rangle$ and $z \in \langle hinge1; end \rangle$ as the vertical loads are transferred to the vertical stabilizer by hinge 1 and are therefore not present above the hinge. That is why there are two tables with force resultants for the CLT - Tables 15 and 16.

			Aerodynamic load	**Tail-down landing**	**Obstruction load**	**Side load**
Skin	N_x	$[N/m]$	$\frac{\pm M_b}{h_{ef} \cdot b_{ef}}$	$-\frac{V_s}{b_{ef}}$	$-\frac{V_s}{b_{ef}}$	$-\frac{V_s}{b_{ef}} + \frac{\pm M_{b-sideload}}{h_{ef} \cdot b_{ef}}$
	N_y	$[N/m]$	0	0	0	0
	N_{xy}	$[N/m]$	$q^A_{M_T^{E.A.}}$	$\frac{S_{tail-down}}{l_s}$	$\frac{S_{obstruction}}{l_s}$	$\frac{S_{sideload-x}}{l_s} + q^{sideload}_{M_T^{E.A.}}$
Web	N_x	$[N/m]$	0	$-\frac{V_w}{h_{ef}}$	$-\frac{V_w}{h_{ef}}$	$-\frac{V_w}{h_{ef}}$
	N_y	$[N/m]$	0	0	0	0
	N_{xy}	$[N/m]$	$\frac{S}{b_{web}} - q^A_{M_T^{E.A.}}$	0	0	$\frac{S_{sideload-y}}{b_{web}} - q^{sideload}_{M_T^{E.A.}}$

Table 15: Load distribution for $z \in \langle 0; hinge1 \rangle$

		Aerodynamic load	Tail-down landing	Obstruction load	Side load
Skin	$N_x \quad [N/m]$	$\frac{\pm M_b}{h_{ef} \cdot b_{ef}}$	0	0	$\frac{\pm M_{b-sideload}}{h_{ef} \cdot b_{ef}}$
	$N_y \quad [N/m]$	0	0	0	0
	$N_{xy} \quad [N/m]$	$q^A_{M_T^{E.A.}}$	$\frac{S_{tail-down}}{l_s}$	$\frac{S_{obstruction}}{l_s}$	$\frac{S_{sideload-x}}{l_s} + q^{sideload}_{M_T^{E.A.}}$
Web	$N_x \quad [N/m]$	0	0	0	0
	$N_y \quad [N/m]$	0	0	0	0
	$N_{xy} \quad [N/m]$	$\frac{S}{b_{web}} - q^A_{M_T^{E.A.}}$	0	0	$\frac{S_{sideload-y}}{b_{web}} - q^{sideload}_{M_T^{E.A.}}$

Table 16: Load distribution for $z \in (hinge1; end\rangle$

6.3.5 Designed Layups and Their Comparison

Analytically determined layups for the skin and web are detailed in Table 17 for the prepreg design and Table 18 for the hand-wetted design. The materials are specified in the brackets following the ply angle. For example, 'Fab88' indicates a ply made from fabric with a reinforcement areal weight of 88 g/m^2, and 'C3' indicates a ply made of a 3 mm thick foam core. The web was checked for stability failures using the same equations used for the skin in Section 6.3.3.

	Prepreg	
	Skin	**Web**
Layup for $z \in \langle 0; hinge1\rangle$	$[(\pm 45)(Fab88)_2, \overline{0(C3)}]_s$	$[(\pm 45)(Fab88)_2, \overline{0(C3)}]_s$
Layup for $z \in (hinge1; end\rangle$	$[(\pm 45)(Fab88), \overline{0(C3)}]_s$	$[(\pm 45)(Fab88)_2, \overline{0(C3)}]_s$
Weight	$613.35\ g$	

Table 17: Layup for Prepreg design

	Hand-Wetted	
	Skin	**Web**
Layup for $z \in \langle 0; hinge1\rangle$	$[(\pm 45)(Fab93)_2, \overline{0(C\_3)}]_s$	$[(\pm 45)(Fab120), \overline{0(C\_3)}]_s$
Layup for $z \in (hinge1; end\rangle$	$[(\pm 45)(Fab93), \overline{0(C\_3)}]_s$	$[(\pm 45)(Fab120), \overline{0(C\_3)}]_s$
Weight	$619.78\ g$	

Table 18: Layup for Hand-Wetted design

The weight in the tables is the weight of the cell hatched in Figure 51 and it already accounts for the adhesive needed for bonding the core to the facesheets. The extra plies in

the skin layup should be dropped at $z \approx 200\ mm$ so the ply drop is not in close vicinity to the heavily loaded area around the hinge. The hand-wetted design is only a few grams heavier thanks to the variety of available materials. Hence, the hand-wetted design is used for the skin and web as the lower manufacturing cost outweighs the weight penalty. However, the prepreg materials are still considered for the hinges and tail wheel attachment and will be used if there is a potential for a significant weight reduction.

6.4 Design of the Hinges

This section presents a preliminary design of the hinges and the control horn, where hinge 1 is integrated into one piece with the control horn.

Magnitudes and angles (orientation shown in Figure 57) of ultimate load reactions acting on the control horn and hinges are shown in Table 19. The reactions differ from those stated earlier, as the effect of control reactions wasn't previously considered. The ratio of ultimate to yield tensile strength of AISI 4140 means it is sufficient to do calculations only for the ultimate load even for metal parts of the hinges. Despite the safety factor for metals generally being 1.5, metal parts must also be designed for a safety factor of 2.25 so they don't fail during the rudder strength tests. For the last case, where the pilot exerts a force of 90 daN on both pedals, the ultimate load is given for both safety factors of 1.875 and 2.25 as the load cancels out in the hinge and doesn't transfer to the surrounding structure, so if the hinge ends up being made from prepreg material, the lower safety factor can be used.

Ultimate load	**Control horn**		**Hinge 1**			**Hinge 2**	
	$R_t[N]$	$\alpha_{R_t}[^\circ]$	$R_{h1}^{hor}[N]$	$\alpha_{R_{h1}^{hor}}[^\circ]$	$R_{h1}^{ver}[N]$	$R_{h2}^{hor}[N]$	$\alpha_{R_{h2}^{hor}}[^\circ]$
Aerodynamic load	3460.14	337	3224.75	171	0	512.28	270
Tail-down landing	0	-	998.75	180	5268.58	412.97	180
Obstruction load	0	-	3518.96	0	4723.69	791.73	180
Side load	5200.10	0	5798.03	161.66	1650.98	211.78	234.2
125% Hinge moment	4325.18	337	4325.18	157	0	0	-
90 daN rudder pedals (f=1.875)	2x 6041.63	0	12083.25	180	0	0	-
90 daN rudder pedals (f=2.25)	2x 7249.95	0	14499.9	180	0	0	-

Table 19: Ultimate load reactions in hinges

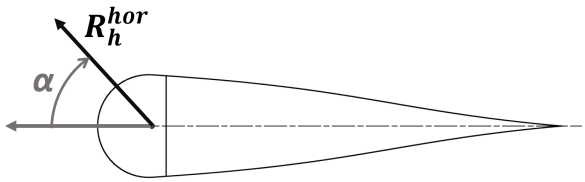

Figure 57: Orientation of α

6.4.1 Hinge 1 with control horn

Hinge 1 transfers the horizontal load, vertical load, and control load. The conceptual design of the hinge is shown in Figure 58.

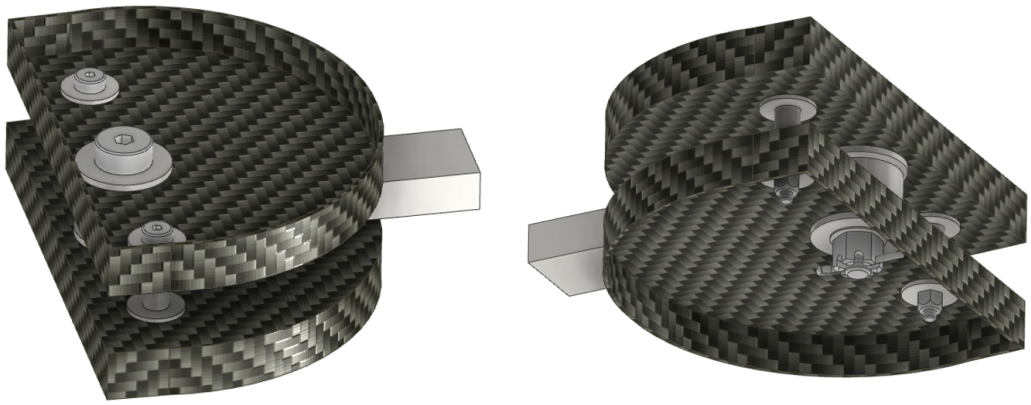

Figure 58: Conceptual design of hinge 1

The hinge consists of two CFRP ribs that will be glued to the web and skin in front of the web, shoulder screws, flanged bushings, inserts, spacers, washers, and hexagon castle nuts with pins. The cross section of the hinge is shown in Figure 59. The middle main joint connects the rudder to the vertical stabilizer hinge, and the outer bolts are used for the control cables connection. All the non-standardized metal parts will be made of AISI 4140 steel. The dimensions in Figure 59 are not proportional, and the parts' dimensions are determined further.

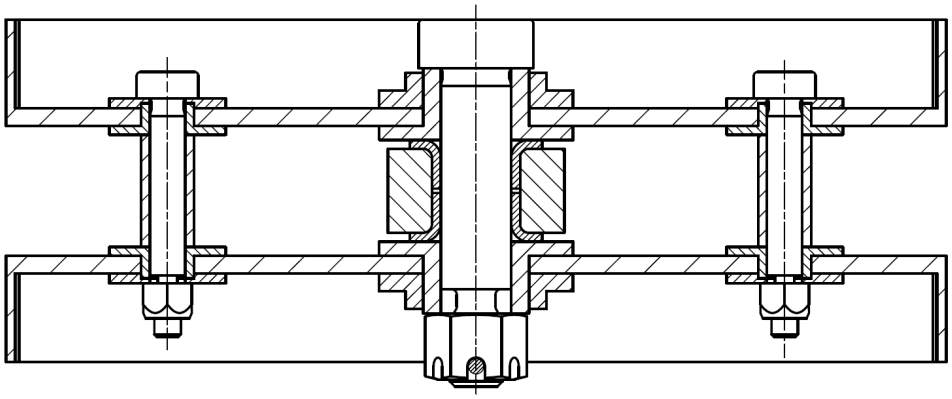

Figure 59: Cross section of the concept of hinge 1

The main joint is designed first. The design of the vertical stabilizer hinge is beyond the scope of this thesis; nonetheless, a preliminary calculation was conducted to determine the required hinge height to withstand the bending moment induced by the vertical reaction. A 20 mm distance between the ribs should guarantee enough design margins if higher-grade steel (like the AISI 4140) is used. The SKF PCMF 081005.5 E flanged bushing is chosen to accommodate the axial and radial loads while maintaining low friction to not highly influence

the control loads that the pilot must exert. Two bushings are used to accommodate axial loads in both directions. Their combined basic static load rating is slightly lower than the highest ultimate horizontal reaction (13900 N vs 14500 N). Nevertheless, the bushing should not disintegrate under the higher load but only offer inferior sliding capabilities, which is acceptable under the ultimate load. [41]

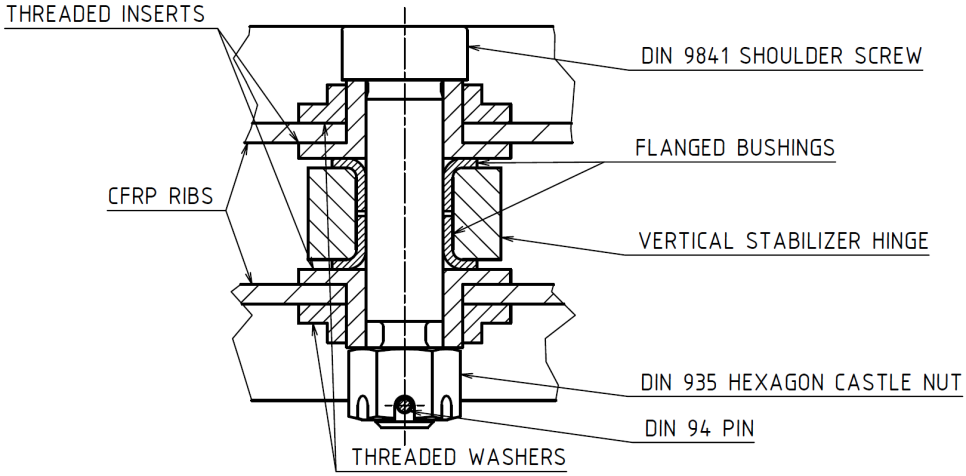

Figure 60: Detail of the main joint of hinge 1

DIN 9841 (equal to ISO 7379) shoulder screw is used to fasten the joint. The shoulder diameter corresponds to the bore diameter of the bushing and therefore is 8 mm whereas the thread is of M6 specification. The grade of the screw is 12.9 meaning the minimum ultimate tensile strength is 1220 MPa and the minimum yield tensile strength is 1100 MPa. [42] The strengths are higher than those of the inserts and bushings and the bearing capacity of the screw therefore doesn't have to be verified, but the shear strength of the screw is checked.

The ultimate shear strength of ductile material can be approximated as $0.577 \cdot \sigma_t^u$ (according to maximum distortion energy criterion) and the screw has two shear planes resulting in the following equation for the maximum shear load:

$$P_s^m = 0.577 \cdot \sigma_t^u \cdot 2 \cdot \frac{\pi \cdot d^2}{4} = 0.577 \cdot 1220 \cdot 2 \cdot \frac{\pi \cdot 8^2}{4} = 70767.77\ N\ . \tag{6.52}$$

The maximum ultimate horizontal reaction is 14499.9 and the screw therefore has an additional 4.9 safety factor.

As stated earlier, the threaded inserts are made of AISI 4140 steel. The bore diameter is 8 mm, the wall thickness is 2 mm (12 mm diameter) to accommodate the thread and the flange diameter will be as large as possible without interfering with the composite rib. The thickness of the insert's flange is 1.6 mm which correlates with the thickness of a standard washer. The CFRP ribs are laterally constrained around the holes by the threaded insert and washer significantly increasing the bearing strength of the laminate. [43]

The insert must be checked for bearing failure. The minimum height of the insert in contact with the screw and with the CFRP rib is calculated. Each insert should carry half of the load, however, an additional safety factor of 1.2 is used to account for possible discrepancies in the load distribution between the inserts. The ultimate bearing strength of AISI 4140 stated in MIL-HDBK-5J is greater than the ultimate tensile strength, but the values are given only for edge distance-to-fastener diameter ratio greater than 1.5 whereas the inserts are a thin-walled structure. [44] Therefore, the ultimate tensile strength is used as the ultimate bearing strength. The necessary height of the insert h_{min}, when assuming that the bearing stress has a rectangular distribution over the area $A = d \cdot h_{min}$, is:

$$h_{min} = \frac{0.6 \cdot R_{h1}^{hor,ult}}{\sigma_t^u \cdot d} \ . \tag{6.53}$$

So the resulting minimum height of the insert in contact with the screw is:
for $f = 1.875$:

$$h_{min}^{sc} = \frac{0.6 \cdot 12083.25}{1000 \cdot 8} = 0.91 \ mm \ , \tag{6.54}$$

for $f = 2.25$:

$$h_{min}^{sc} = \frac{0.6 \cdot 14499.9}{1000 \cdot 8} = 1.09 \ mm \ , \tag{6.55}$$

And the resulting minimum height of the insert in contact with the rib is:
for $f = 1.875$:

$$h_{min}^{rib} = \frac{0.6 \cdot 12083.25}{1000 \cdot 12} = 0.61 \ mm \ , \tag{6.56}$$

for $f = 2.25$:

$$h_{min}^{rib} = \frac{0.6 \cdot 14499.9}{1000 \cdot 12} = 0.73 \ mm \ . \tag{6.57}$$

The design of the control cable connection differs from the main joint's design. The inserts and washers are not threaded and there is a spacer tube between the inserts. The constraint of the CFRP rib is done by the axial load introduced by torquing the nut. The nuts in Figure 59 are prevailing torque hex lock nuts, but hexagon castle nuts with pins will be used instead. The bending of the spacer and screw must be taken into account, the maximum bending moment occurs when the control cable is in the middle of the spacer. The minimum outside diameter of the spacer was calculated using a bending stress calculator (https://www.omnicalculator.com/construction/bending-stress) to be 7 mm without any stress reserve. Therefore, an 8 mm diameter was chosen because the weight increase is negligible, and it provides a significant safety improvement by ensuring that the bending stress remains lower than the yield stress of the bolt and spacer. The spacer tube is remodeled to ensure the position of the control cable as the movement of the cable toward one of the ribs would cause a shift in load distribution and additional moments. The shoulder

screw with a 5 mm shoulder diameter is used meaning the spacer's wall thickness is 1.5 mm. The thickness of the inserts' flanges and walls is designed to be 1 mm and the outside flange diameter is 14 mm corresponding to a standardized washer diameter for a 7 mm hole. The thickness of the washers depends on the needed insert's contact surface with the screw as the shoulder neck fillet decreases the contact surface with the insert and the outside diameter is the same as the insert's flange diameter. Figure 61 shows the redesigned control cable connection.

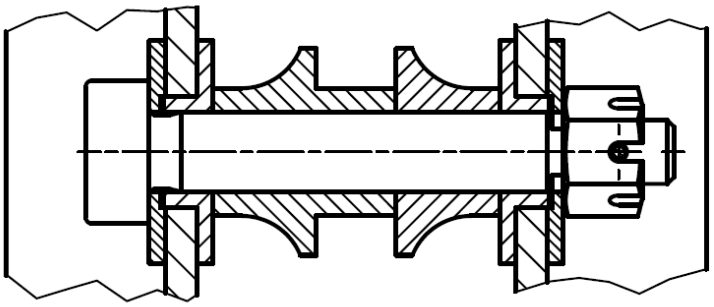

Figure 61: Redesigned control cable connection (view rotated by 90°)

The maximum shear load the shoulder screw in the control cable connection can withstand is:

$$P_s^m = 0.577 \cdot \sigma_t^u \cdot 2 \cdot \frac{\pi \cdot d^2}{4} = 0.577 \cdot 1220 \cdot 2 \cdot \frac{\pi \cdot 5^2}{4} = 27643.66\ N\ . \tag{6.58}$$

resulting in an additional 3.81 safety factor for screw shear failure.

The minimum height of the bearing surface is calculated using Equation 6.53: The resulting minimum height of the insert in contact with the screw is:
for $f = 1.875$:

$$h_{min}^{sc} = \frac{0.6 \cdot 6041.63}{1000 \cdot 5} = 0.73\ mm\ , \tag{6.59}$$

for $f = 2.25$:

$$h_{min}^{sc} = \frac{0.6 \cdot 7249.95}{1000 \cdot 5} = 0.87\ mm\ , \tag{6.60}$$

And the resulting minimum height of the insert in contact with the rib is:
for $f = 1.875$:

$$h_{min}^{rib} = \frac{0.6 \cdot 6041.63}{1000 \cdot 7} = 0.52\ mm\ , \tag{6.61}$$

for $f = 2.25$:

$$h_{min}^{rib} = \frac{0.6 \cdot 7249.95}{1000 \cdot 7} = 0.63\ mm\ . \tag{6.62}$$

The last step of the design of hinge 1 is to design the layup of the ribs. The rib is designed to bear the load from the bolted joints. The ribs are subjected to a vertical load introduced

by the ground load cases. An analytical solution of the stress state of the rib caused by this load would be too laborious with uncertain results, hereby the proposed layup is later checked by finite element analysis.

There are five most common failure modes in composite bolted joints: local bearing, net tension, wedge-type splitting, shear-out, and tension with shear-out. The laminate is being designed to resist these five failure modes (shown in Figure 62), the best layup, according to tests, for composites in bolted joints is $1/3$ of fibers in $0°$ direction and $2/3$ of fibers in $\pm 45°$ direction, where the $0°$ corresponds to the load's direction. The ribs lie in the xy plane as defined in Figure 23 and the reference axis of the ribs corresponds to the x-axis. The load direction is not the same for all the load cases, however, the maximum load lies in the reference direction and the maximum deviation in the load's direction is only 23° so the previously mentioned ratio of fiber directions should work well for the ribs and was used for first iteration. [43, 45]

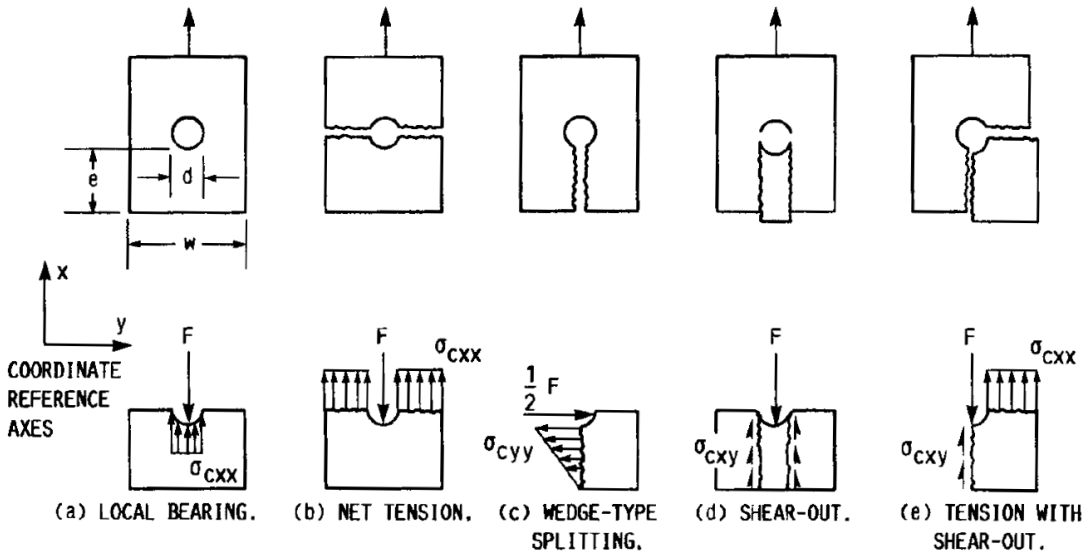

Figure 62: Failure modes in composite bolted joints [45]

Each of the two ribs is designed to withstand 0.6 multiple of the total load, which equals an additional safety factor of 1.2 that was also used to design the metal inserts. The rib's bearing capacity is checked for both the main hinge joint and the control connection joint. Laminate compressive strength parallel to the bolt force σ^u_{xc}, laminate tensile strength parallel to the bolt force σ^u_{xt}, laminate transverse tensile strength σ^u_{yt}, and laminate shear strength σ^u_{xy} must be determined before further calculations. This is being done using the CLT and Tsai-Hill and Tsai-Wu criteria for all the angles of the reactions. The designation of dimension variables of the joint is shown in Figure 63, an additional variable k is introduced in wedge-type splitting failure determination and it denotes the expected height of the rib's flange in the spar's vicinity. The numerical values of the variables are showcased in Table 20.

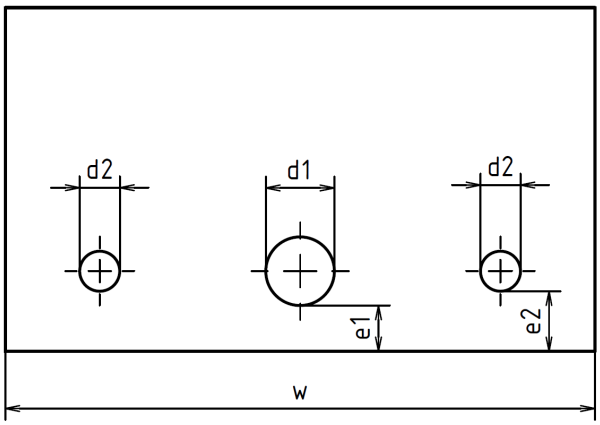

Figure 63: Designation of joint dimensions

$d1 =$	$12\,mm$
$d2 =$	$7\,mm$
$w =$	$103\,mm$
$e =$	$8\,mm$
$k =$	$20\,mm$

Table 20: Joint's dimensions

To calculate the local bearing stress for the main joint, the following equation is used:

$$\sigma_{bearing}^{mj} = \frac{F}{d1 \cdot h}\ , \tag{6.63}$$

where:

$F = 0.6 \cdot R_{h1}^{hor}$,

$h =$ *laminate thickness* .

For the control connection joint modified formula is used:

$$\sigma_{bearing}^{ccj} = \frac{F_c}{d2 \cdot h}\ , \tag{6.64}$$

where:

$F_c = 0.6 \cdot R_t$.

Laminate compressive strength parallel to the bolt force σ_{xc}^{u} must be greater than the computed local bearing stresses.

The net tension stress, which has to be lower than the laminate tensile strength parallel to the bolt force σ_{xt}^{u}, is:

$$\sigma_{net-tension}^{mj} = \frac{F}{(w - d1 - 2 \cdot d2) \cdot h}\ . \tag{6.65}$$

The equation is the same for the control connection joint, except that F_c is used instead of F. For this and the following failure modes, the dimensions needed for the calculation depend on the reaction angle. However, the dimensions provided in Table 20 are used for all cases in the calculations. This approach is conservative because the dimensions for other reaction angles are larger.

The wedge-type splitting stress $\sigma^{mj}_{w-t-splitt}$ (Equation 6.66) must be lower than the laminate transverse tensile strength σ^{u}_{yt}. The flange height is used in the formula as the flange has significant load-carrying capabilities for this failure mode. The wedge-type splitting, shear-out, and tension with shear-out modes are sufficient to be calculated only for the main joint as the reactions in the control connection joint act in the directions where the edge-to-hole distance e is much larger than for the main joint, which gives the certainty that the mentioned failures will not occur.

$$\sigma^{mj}_{w-t-splitt} = \frac{2 \cdot F}{(2 \cdot e - d1 + k) \cdot h} \tag{6.66}$$

The shear-out stress is:

$$\sigma^{mj}_{shear-out} = \frac{F}{2 \cdot e \cdot h} \ . \tag{6.67}$$

This stress must be lower than the laminate shear strength σ^{u}_{xy}.

For the tension with shear-out failure mode, the maximum load is calculated instead of the stress:

$$F_{max} = \frac{h \cdot (w - d1 - 2 \cdot d2) \cdot \sigma^{u}_{xc} + 2 \cdot e \cdot \sigma^{u}_{xy}}{2} \ . \tag{6.68}$$

The reactions F must not be bigger than the calculated maximum load F_{max}.

The lightest layup for the prepreg design, capable of withstanding all five failure modes, weighs approximately 35 grams per rib. This calculation assumes a 1 cm high flange, except in the contact area between the rib and spar where a 2 cm flange is used. The laminate is 2.04 mm thick and is composed of the following plies:

$$[(\pm 45)(Fab88), (0/90)(Fab210), (\pm 45)(Fab210)_2, \overline{90(UD300)}]_S \ .$$

The hand-wetted rib design is heavier at 44 grams per rib and noticeably thicker at 2.74 mm. The stacking sequence is as follows:

$$[(0/90)(Fab120), (0/90)(Fab200), (\pm 45)(Fab200)_3, \overline{90(UD125)}]_S \ .$$

Using prepreg ribs would save 18 grams in rib weight and a few grams in metal inserts, as their thickness can be reduced due to the lower laminate thickness. However, the weight savings are not justified by the additional cost of materials and technology associated with prepreg

use. Therefore, it is chosen to pursue the hand-wetted design further. The rib thickness meets the minimum bearing surface requirement for the inserts, so there is no need to change their dimensions.

The last thing to be analytically determined in the ribs design is the height of the flange needed for the load transfer through the adhesive to the rudder's skin and spar. Permabond ET5429 thixotropic adhesive is assumed to be used. The shear strength of the cured adhesive for CFRP bonding is higher than 25 MPa, the exact strength could not be determined as the bonded substrate failed first during tests. At 54 °C (temperature for white-painted surfaces and vertical sunlight [37]), the adhesive attains 90% of its room temperature strength [46]. Assuming each of the ribs has to carry 0.6 times the maximum vertical reaction, the needed adhesive surface is:

$$S_A^{min} = \frac{0.6 \cdot 5268.58}{25 \cdot 0.9} = 140.5\ mm^2\ . \tag{6.69}$$

With the circumference of the rib being approximately 300 mm, the needed flange height is under 0.5 mm. Nevertheless, a height of 10 mm is used around the rib-skin bond line to guarantee better stress redistribution and a 20 mm high flange is used for the rib-spar bond line as assumed for the bolted joint calculations.

6.4.2 Hinge 2

The upper hinge (Figure 64), which transfers only horizontal loads, consists of a single CFRP rib, washer nut, and pin which transfers the loads to the vertical stabilizer upper hinge via an SKF GE 5 E radial sphere bearing [47]. The washer nut and pin are glued to the rib so they don't have to be additionally secured.

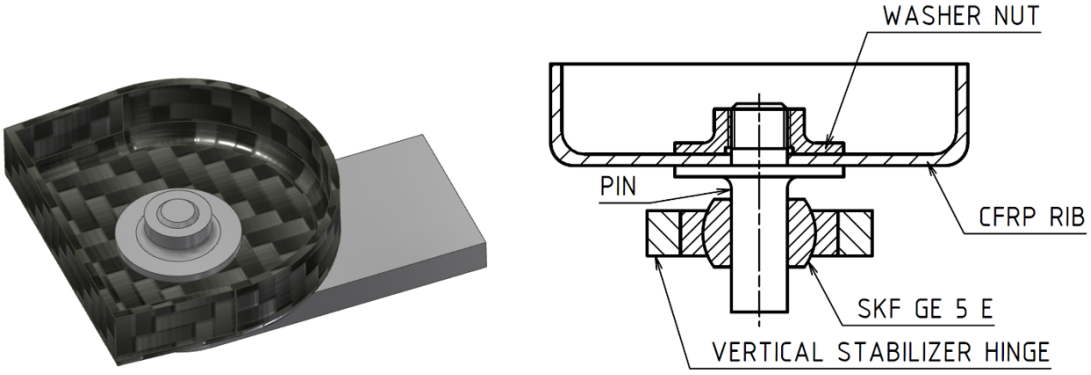

Figure 64: Design of hinge 2

The hinge was designed similarly to hinge 1. The 5 mm diameter pin was analyzed for shear, bearing, and bending stresses. The minimum thickness of the rib's laminate to prevent pin failure in bearing is determined to be 0.16 mm. The rib's layup is designed to withstand the five failure modes typically observed in bolted joints. Additionally, misalignment between

the rib's web and the stabilizer hinge introduces additional moments on the rib, necessitating careful consideration in finite element analysis. Due to the small size of the rib and minimal potential weight savings, only the hand-wetted design was pursued, featuring a 10 mm flange resulting in a weight of less than 5 grams. The designed layup is as follows:

$$[(0/90)(Fab120), \overline{(\pm 45)(Fab93)}]_S \ .$$

6.5 Design of the Tail Wheel Attachment

When searching for a tail wheel with 150 mm as originally intended in the airplane's design, it was found that such wheels usually weigh more than 500 grams. It was therefore decided to use a 110 mm wheel originally used for freestyle scooters as its weight is 220 grams, bearing included. The load capacity of the wheel is not disclosed, but it has to survive high dynamic loads when mounted on a scooter, so it is assumed it should be strong enough to be used as a tail wheel. The wheel width is 24 mm and the inner diameter of the bearing is 8 mm. [48] The tail wheel attachment (shown in Figure 65) is constructed using carbon fiber composite and is bonded to the rudder's skin and spar. Additionally, it is designed to serve as a wheel well to prevent debris from entering the inside of the rudder. The design is developed specifically for the hand-wetted variant, consistent with the approach used for other components.

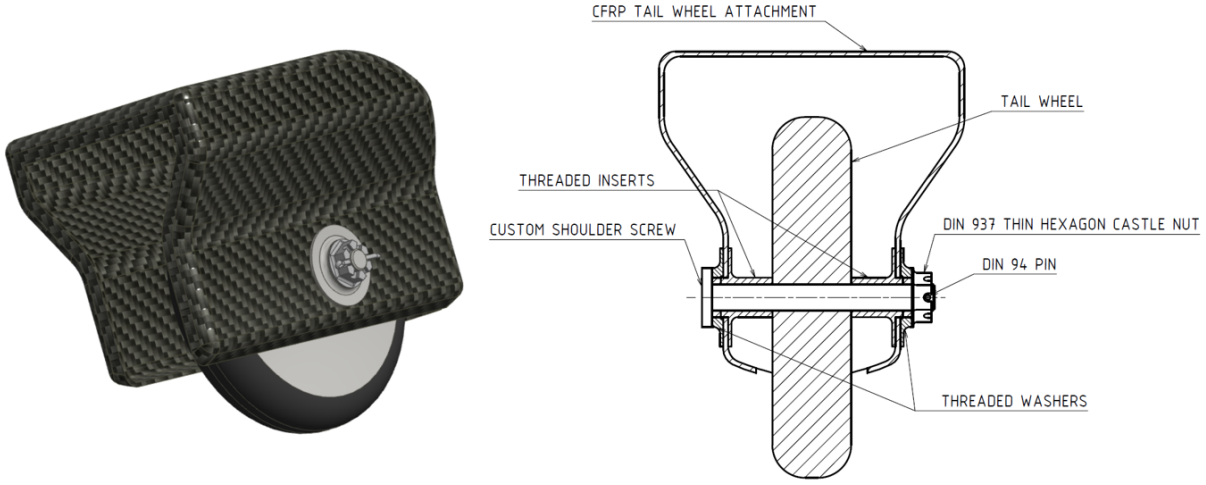

Figure 65: Conceptual design of the tail wheel attachment

The metal (AISI 4140) inserts and threaded washers create a lateral constraint of the CFRP attachment to increase the bearing strength. The thickness of the insert walls is 2 mm to ensure the shoulder screw doesn't fail in bending, which was checked using the online bending stress calculator mentioned in the section about the design of hinge 1. The shoulder screw has to be made bespoke, as the standardized screw would not fit without protruding

out of the skin. Holes will be made in the skin to enable easy wheel change, those holes can then be taped up for flight. The insert's contact surface with the screw is large, resulting in low bearing stress. The laminate used for the attachment will surely have lower bearing strength than AISI 4140, which eliminates the need for bearing stress checks of metal parts. Additionally, the shear stress acting on the bolt is significantly lower compared to hinge 1 and therefore does not need to be computed.

The CFRP attachment is analytically calculated only for the local bearing case, as there is enough material around the hole in the load directions to be sure no other failure mode for the bolted joints is possible. The adhesion surface of the attachment is larger than 6000 mm^2 (including the attachment-to-spar joint) so there is no doubt about the sufficient strength of bonded joint.

The distance between the points where the wheel axle is attached to the attachment is larger than the minimum distance x calculated in Section 6.2.3, hence only the tail-down landing load and obstruction load may be considered for the local bearing failure. The ultimate load for these cases is 5454.443 N. As previously assumed for the hinge 1, each side of the attachment is expected to transfer 0.6 times the ultimate load, which applies to both cases except for the direction of the load. The layup orientation is given regarding the rudder's z-axis (as in Figure 23) as a reference axis. The lightest laminate to withstand the local bearing is:

$$[(-75/15)(Fab160), (-30/60)(Fab160)]_S \ .$$

The thickness of the laminate is 0.88 mm, and the unusual ply angles are employed to align the fibers with the load directions.

This marks the end of the preliminary design using analytical methods. In the following section, the rudder as a whole is subjected to finite element analysis to verify the design's structural integrity.

7 Finite Element Analysis

"In mechanical structural simulation, the finite element method is the numerical method used to solve problems to predict the behavior of a structure. To solve a problem, the finite element method subdivides a large problem into smaller, simpler parts called finite elements. The simple equations that model these finite elements are then assembled into a larger system of equations that models the entire problem. The mathematical formulation of the problem results in a system of algebraic equations, and advanced algorithms compute the approximate values of unknowns at a discrete number of points across the domain. During a structural simulation, the finite element method permits the engineers to compute the stiffness and strength of the analyzed structure and visualize the displacement and distribution of stresses and strains within it." [49]

7.1 Element Type Selection, Meshing

The rudder can be considered a thin-walled structure, and it is therefore preferable to use 2D elements to avoid shear locking. The 2D mesh is easier to create, allows for simple layup change without the need for re-meshing, and the solution requires less computational power than for 3D elements. Linear thin shell elements are used for the mesh. Each node of the element has 5 degrees of freedom - three translations $[u_x, u_y, u_z]$ and two rotations $[\theta_x, \theta_y]$ as shown in Figure 66, and they have no stiffness for the remaining θ_z degree of freedom. Both membrane and bending effects can be extracted from the shell element. Linear element performs well for flat surfaces and double-curved structures assuming a sufficient mesh refinement. Quadrilateral elements are preferably used in the mesh as triangular elements have excessive stiffness but are sometimes needed for a mesh transition. [49]

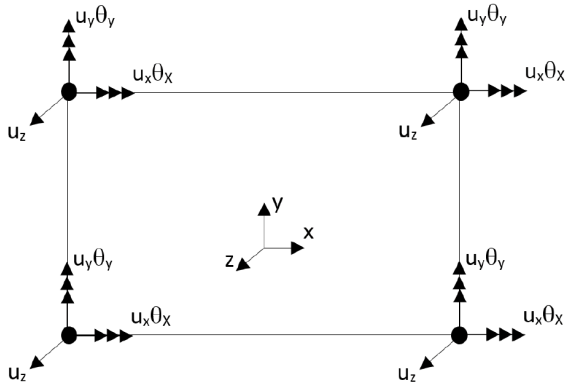

Figure 66: Thin shell element [49]

The pre- and post-processing of the analysis is done using Siemens NX (version 2212) software. An idealized surface model (cross section shown in Figure 67) was created where

some details, like radii on edges of composite parts, are omitted as they would add unnecessary complexity to the model.

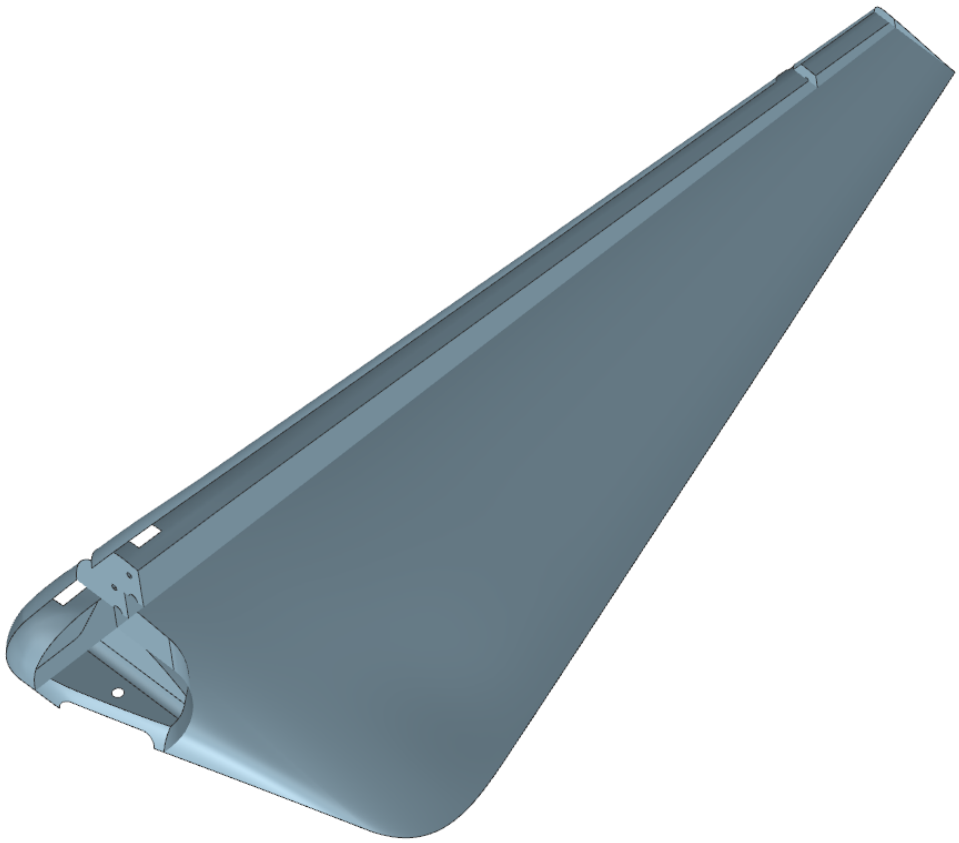

Figure 67: Cross section of idealized surface model

Relatively fine mesh is used for the analysis as the shell elements don't require much computational power. The mesh consists of multiple sub-meshes so the different layups can be defined for parts of the rudder. Detail of the mesh is shown in Figure 68.

The following conditions must be met to ensure the mesh's usability:

- No free edges at polygon interfaces
- No duplicate elements or nodes in the mesh
- Majority of elements have acceptable shapes
- Consistent direction of elements' normals
- Consistent material orientation in the elements

Out of 77455 elements, 119 failed the shape quality check using predefined values in NX. This is acceptable as the failed elements are not close together and most are not in a critical region, so the negative influence on the quality of results is negligible.

The layups of different sections are assigned as a physical property to a mesh. The

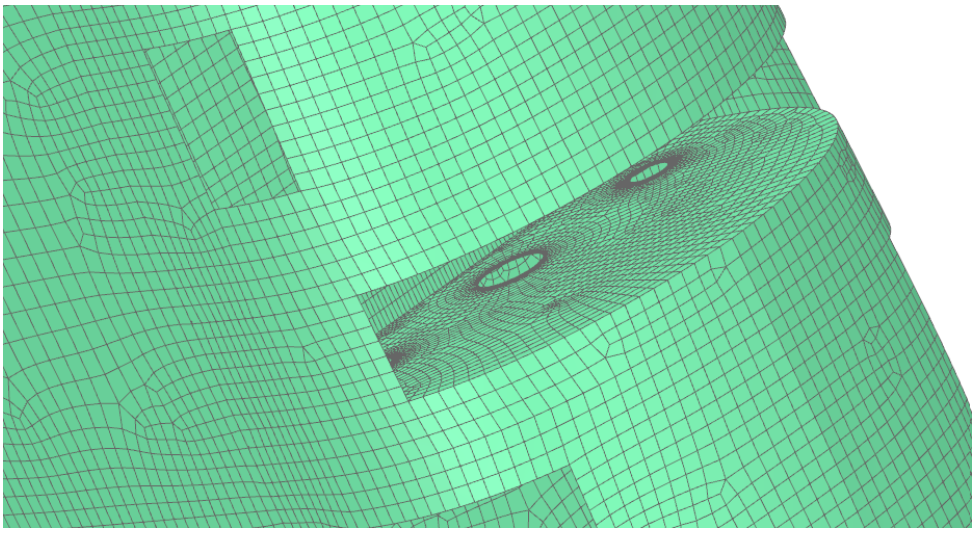

Figure 68: Meshed idealized model

Tsai-Hill and Tsai-Wu ply failure theories are used and transverse shear failure theory is used for interlaminar failures. The interlaminar shear strength of CFRP used for the analysis is 54.3 MPa [50].

1D RBAR elements are used to simulate the bolts, inserts, and washers (Figure 69). RBAR elements are infinitely stiff, so they add artificial stiffness to the model, but inserts and bolts also have relatively high stiffness, meaning the stiffness of RBAR elements should not significantly affect the results as the bolts are designed not to yield. Another consequence of RBAR elements use is that the radial reactions from the bolts are distributed both by compression on one side of the hole, and tension on the other. While this may appear to be an oversimplification, the inserts and washers are bonded to composite parts or are constrained by bolt preload, allowing a portion of the load to be transferred by tension. Analytical checks were also performed on bearing failures, minimizing the significance of inaccurate stress distribution around the holes. The infinite stiffness of the metal part creates a significant stiffness step on the ribs, resulting in a stress peak and conservative rib design.

7.2 Constraints and Loads

The analysis is performed for 6 cases - the three ground load cases, the aerodynamic load case, the 125% hinge load case, and the 90 daN force on both pedals case. Constraints and loads differ case by case. The coordinate system for the analysis differs from the one used previously, and is shown in Figure 70.

The constraint used for hinge 2 is the same for all the cases. The RBAR elements simulating the pin and washer nut are connected to a single node (Figure 71). The node's displacement is constrained in x and z directions, all other degrees of freedom are free. This

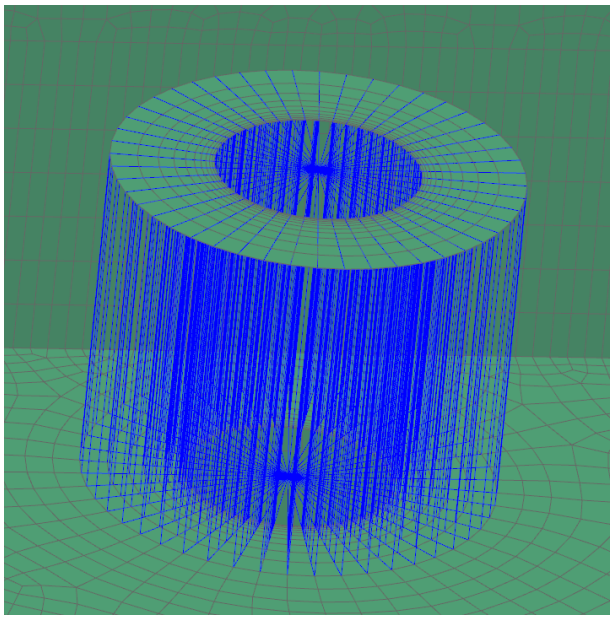

Figure 69: Bolt connection substitution by RBAR elements

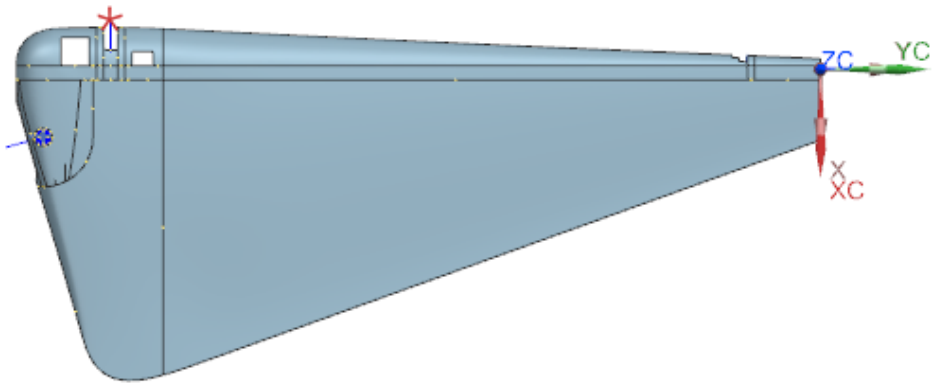

Figure 70: Coordinate system for the analysis

simulates that the pin can move vertically and the radial sphere bearing can rotate around all the axes (in a limited manner)

The main joint in hinge 1, where the rudder connects to the vertical stabilizer is simulated by constraining one RBAR element connecting the middle of the bolt holes to only be able to rotate around the y-axis. This constraint is used for all the load cases, except for the load from pedals, where all the degrees of freedom of the element are constrained. The rotation of the rudder about the y-axis is constrained by simulating the control cable by an RBAR element which is deflected by 23 degrees to reproduce the rudder's full deflection. This element is connected to an RBAR element connecting the middle of the bolt holes of the control cable's connection. For the 125% hinge moment case, the rotation is constrained by fixing the displacement of skin in the z-direction, as this case aims at testing the control system and its parts and not the rudder as a whole.

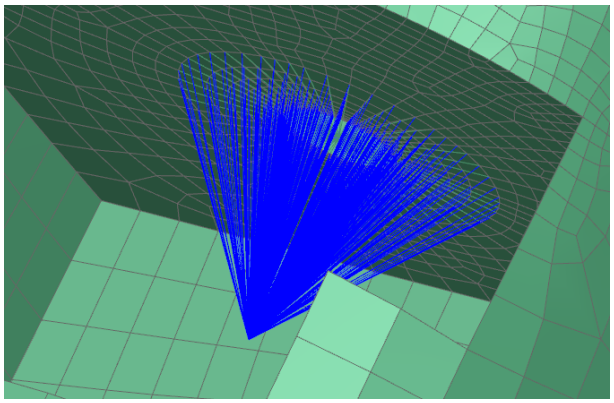

Figure 71: Hinge 2 RBAR connection to node

The tail-down landing and obstruction loads are entered as a force acting in the center of the tail wheel. For the side load case, the point of action of the force is on a node that is located in a place of the tail wheel's ground contact. The node is connected to the center of the wheel by an RBAR element as a tail wheel substitution (Figure 72). For 90 daN force on both pedals case, the control reactions are applied to the 1D elements simulating the bolts. The pressure field with chordwise distribution pictured in Figure 24 is defined and serves as a load for the aerodynamic case.

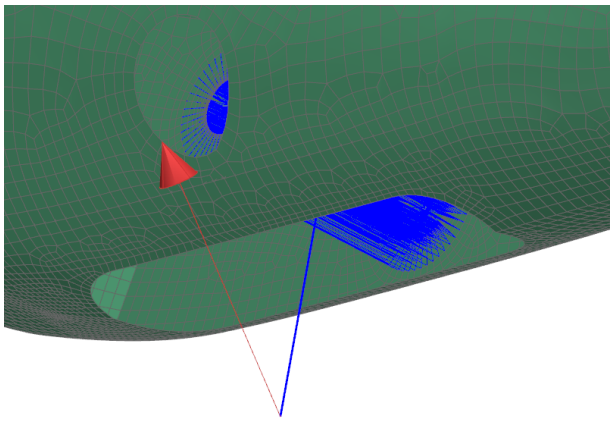

Figure 72: Side load force

7.3 Static Linear Analysis

The first type of analysis that is used is a linear static analysis. This analysis is usable when small deformations are expected, the material properties are elastic, Hooke's law applies, and the external loads and constraints are not time-dependent. [49] The analysis is solved by Simcenter Nastran as a SOL 101 Linear Statics solution type.

The two most important parameters to check when analyzing composite structures are the ply and bond failure indexes. The maximum indexes throughout all plies and all the cases

are shown in Figures 73 and 74, failure occurs once an index is higher than 1. The figures show that there are no skin failures expected.

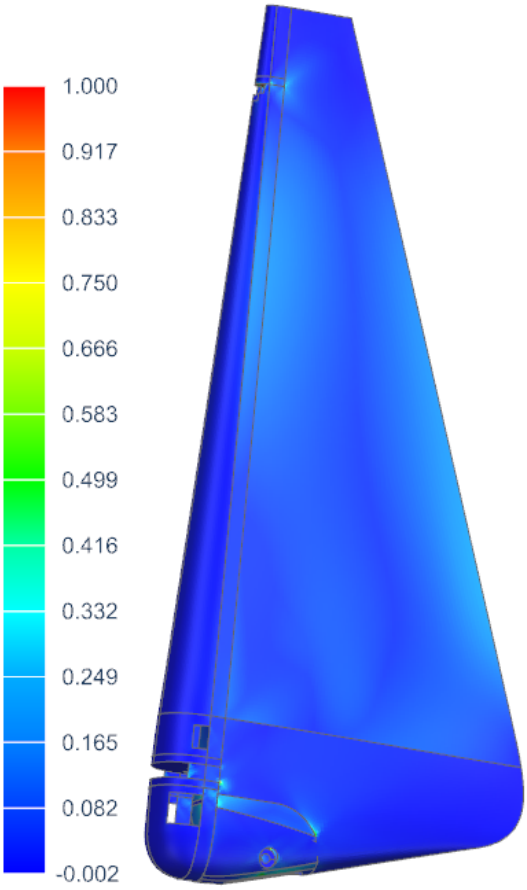

Figure 73: Maximums of ply failure index

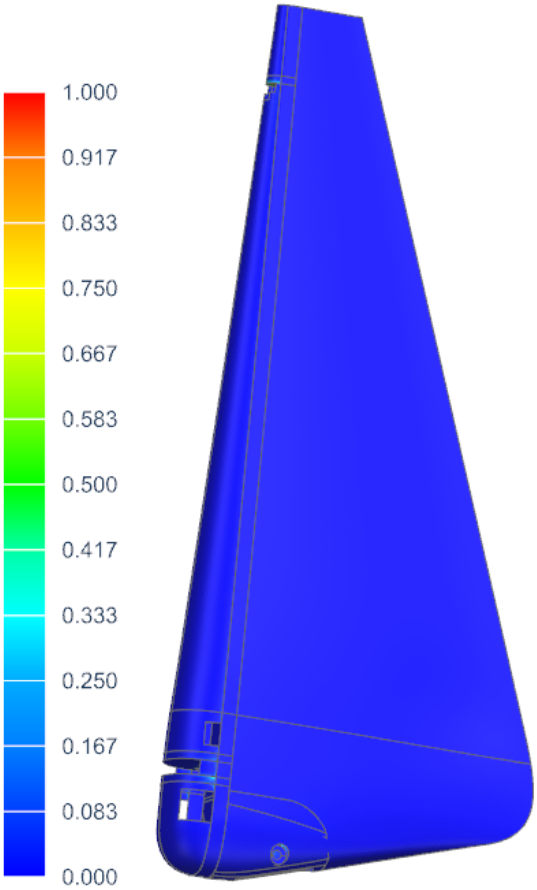

Figure 74: Maximums of bond failure index

When examining the results in more detail, the rib of hinge 2 would fail as both the ply and bond failure index are higher than 1. This is shown in Figures 75 and 76, where the maximum value of the color bar is set to 1 to make the failure regions easily visible as the maximum failure indexes are significantly higher (this was also applied to Figures 73, 74, 77, and 78). In Figures 77 and 78 the bond failure index for ribs of hinge 1 and wheel attachment is shown, indicating failure of these parts. Henceforth the layup of all three ribs and the tail wheel attachment must be redesigned to achieve failure indexes lower than 1.

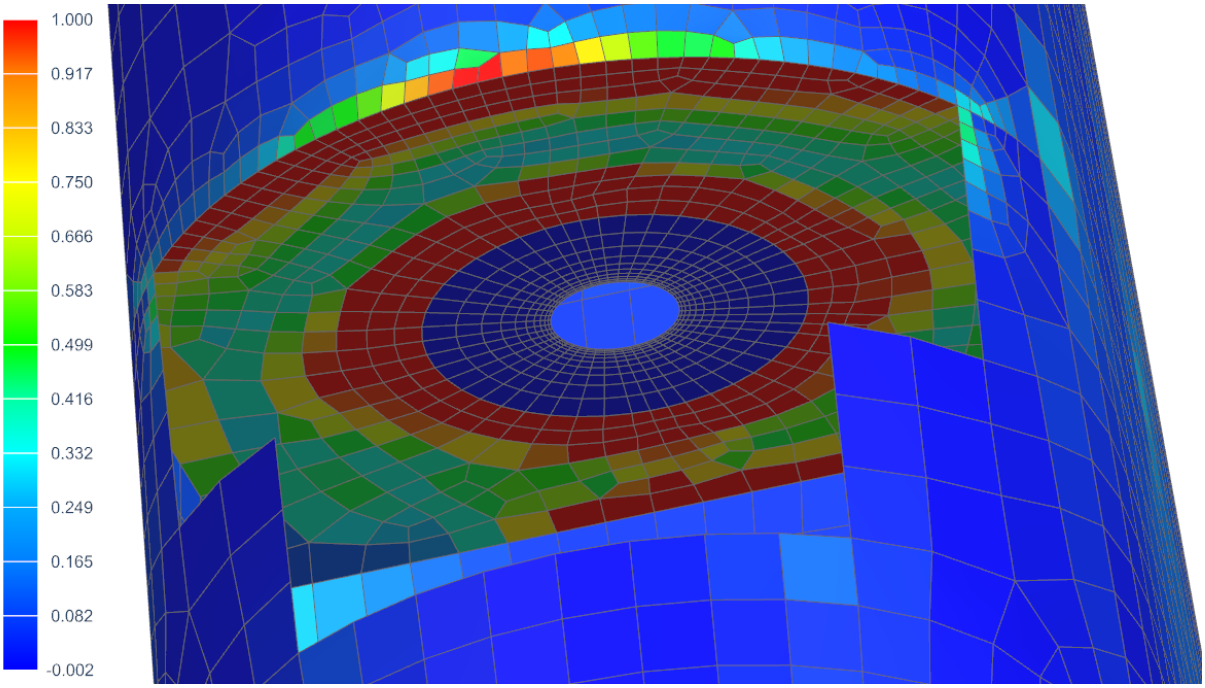

Figure 75: Maximum ply failure index of rib in hinge 2

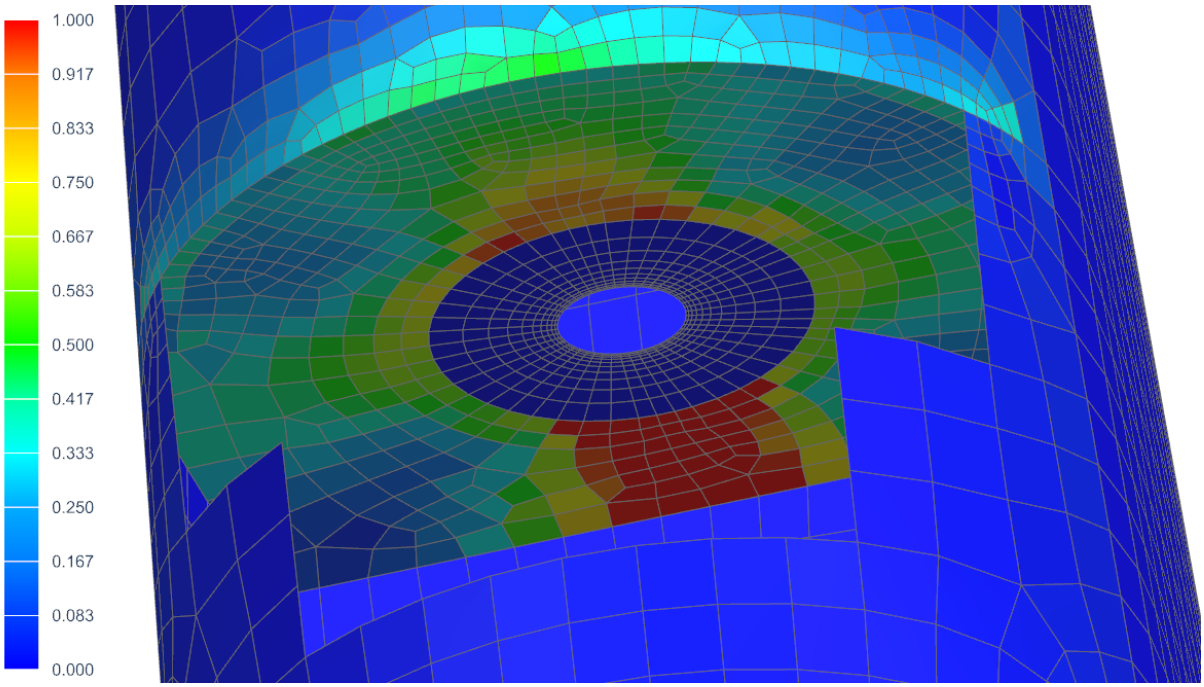

Figure 76: Maximum bond failure index of rib in hinge 2

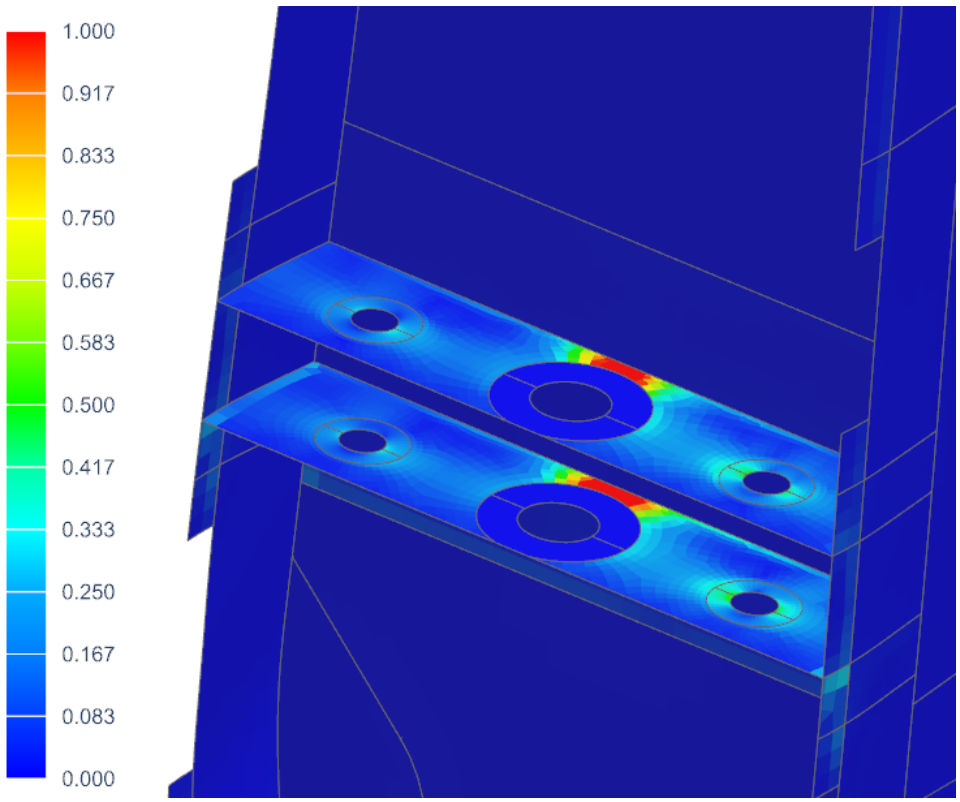

Figure 77: Maximum bond failure index of ribs in hinge 1

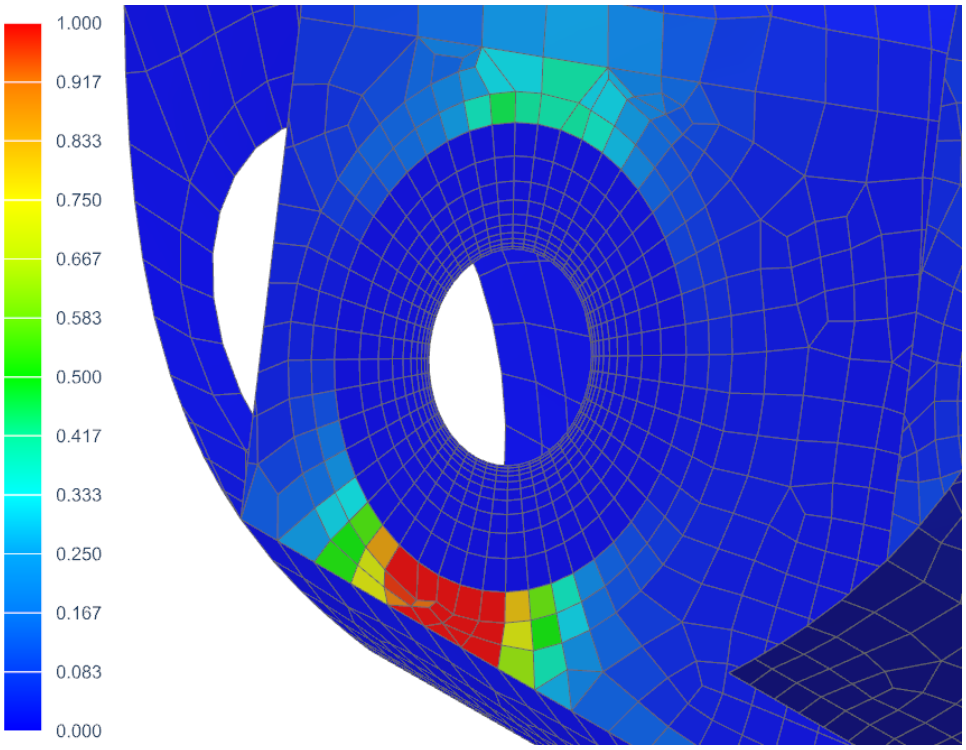

Figure 78: Maximum bond failure index of tail wheel attachment

7.4 Linear Buckling Analysis

After layup modifications, the maximum ply failure and bond failure indexes were under one even in the critical regions. The linear buckling analysis is now employed to assess the stability of the structure. The assumptions of only small deflections and only elastic stresses in the structure are made. Those are valid assumptions as the maximum displacement throughout all the cases is 9.621 mm displacement of the skin for the aerodynamic case (Figure 80), composite materials don't exhibit yielding, and stress in the metal parts should be under their yielding strength. [49]

The outputs of the linear buckling analysis are an eigenvalue and a deformed shape of the structure. The eigenvalue directly gives the load factor of the applied loads that will cause buckling. Thus the smallest eigenvalue throughout all the cases must be higher than 1 to ensure sufficient structure stability. [49]

For the side load case, eigenvalues for four modes are lower than 1 pointing to a buckling failure. All four buckling modes are located around the cutout for the tail wheel, the shape of mode 1 is shown in Figure 79. The layup in this location must be further adjusted to eliminate the buckling modes.

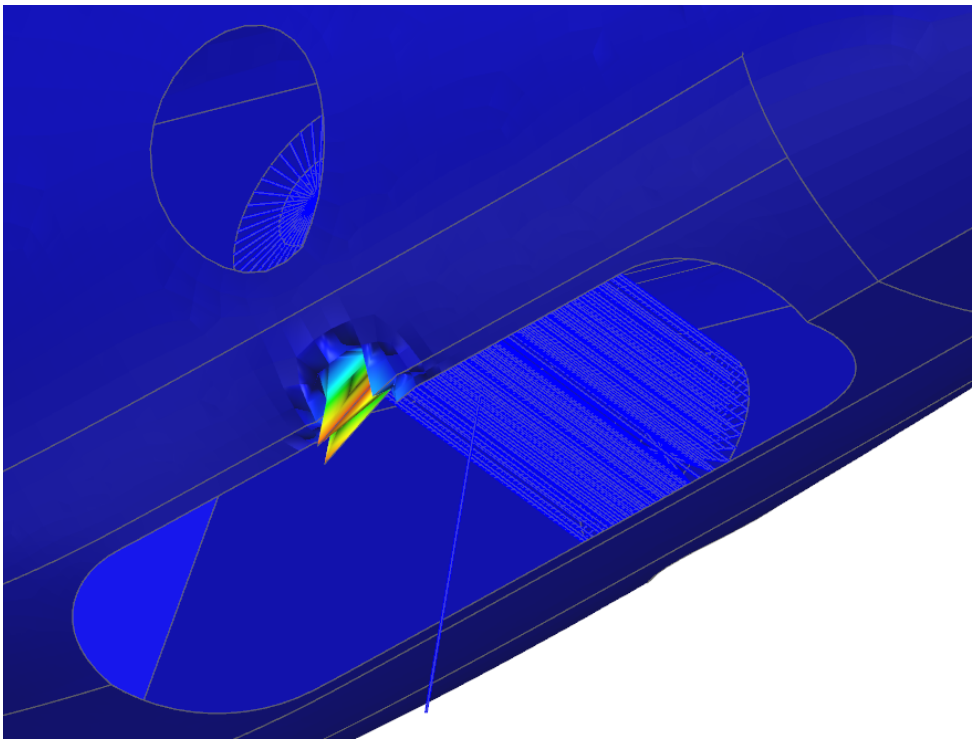

Figure 79: Shape of buckling mode 1 for the side load case

7.5 Overview of Final Layups

The definitive layups are listed in Table 21, which can be found on the following page. Those layups pass the linear static and linear buckling analyses without failure indication, the maximum ply failure index is 0.869, the maximum bond failure index is 0.904 and the minimum buckling eigenvalue is 1.31.

The use of a thinner core and/or fewer plies for the bottom part of the skin was tested to reduce weight. This endeavor was unsuccessful as either strength or buckling failures occurred under the ultimate loads.

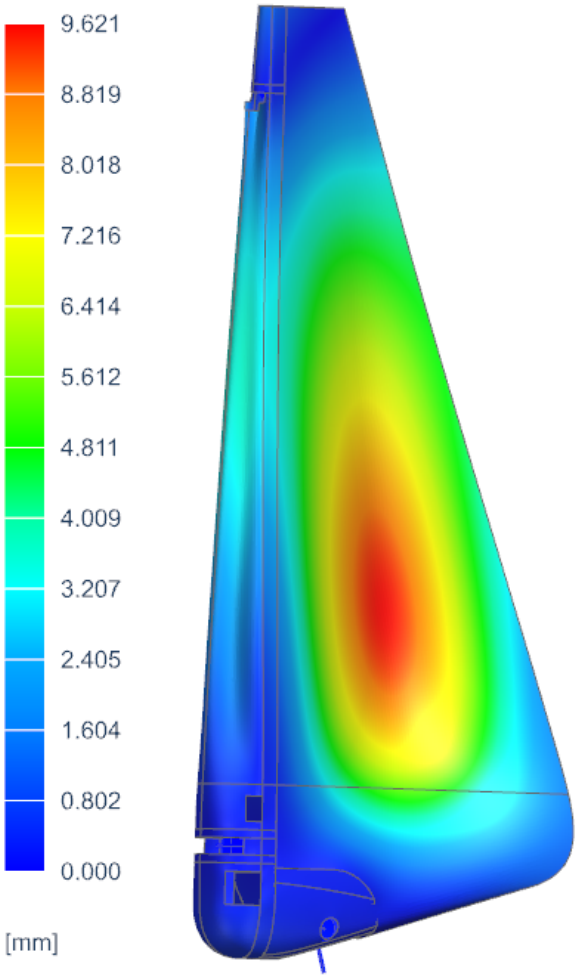

Figure 80: Maximum deformation of the rudder

Component	Region of component		Layup
Skin	Behind spar	$z \in \langle 0; 200 \rangle \ mm$	$[(\pm 45)(Fab93)_2, \overline{0(C3)}]_s$
		$z \in \langle 200; 1129 \rangle \ mm$	$[(\pm 45)(Fab93), \overline{0(C3)}]_s$
	Ahead of spar	$z \in \langle 0; 200 \rangle \ mm$	$[(\pm 45)(Fab93)_4]$
		$z \in \langle 200; 1129 \rangle \ mm$	$[(\pm 45)(Fab93)_2]$
Spar	Whole		$[(\pm 45)(Fab120), \overline{0(C3)}]_s$
Ribs of Hinge 1	Web + back flange		$[(0/90)(Fab120), 0(UD200), (0/90)(Fab200)_2, (\pm 45)(Fab200)_3, \overline{90(UD125)}]_S$
	Rest of flange		$[(0/90)(Fab120), (0/90)(Fab200), (\pm 45)(Fab200)_3, \overline{90(UD125)}]_S$
Rib of Hinge 2	Whole		$[(0/90)(Fab120), 0(UD200), \overline{(\pm 45)(Fab93)}]_S$
Tail wheel attachment	Sides		$[(\pm 45)(Fab160), (-75/15)(Fab160), (-30/60)(Fab160), \overline{(0/90)(Fab160)}]_S$
	Rest		$[(\pm 45)(Fab160), \overline{(0/90)(Fab160)}]_S$

Table 21: Definitive layups

8 3D Model

After design's verification by FEA, 3D model is created in Siemens NX. Fully assembled rudder, including the tail wheel and all parts of the hinges is visualized in Figure 81. Detail of hinge 2 is shown in Figure 82 followed by the detail of hinge 1 and the tail wheel attachment in Figure 83.

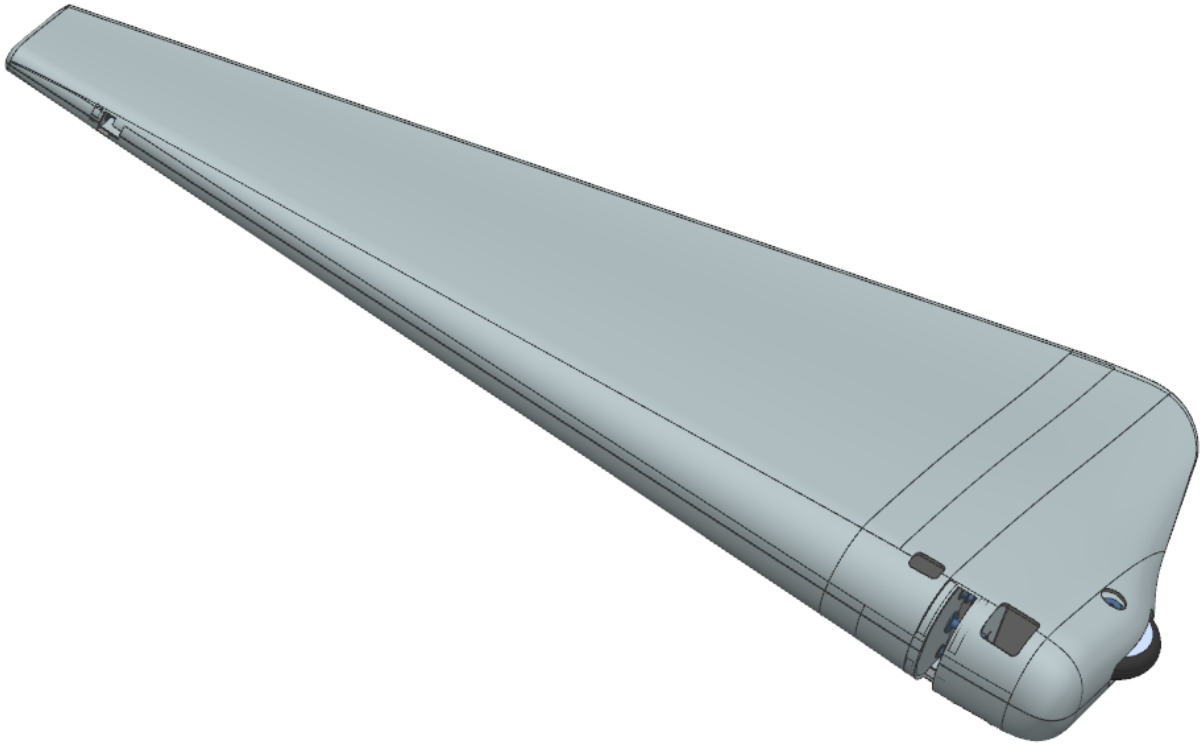

Figure 81: 3D model of rudder

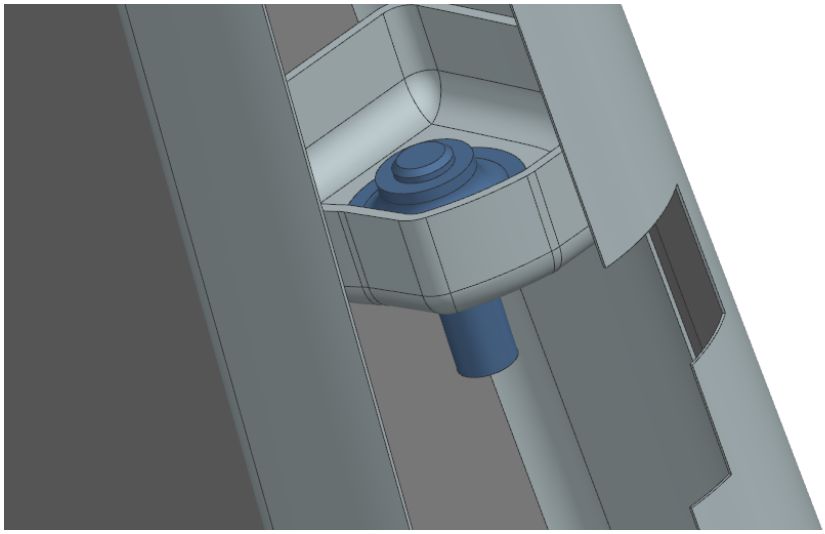

Figure 82: Detail of Hinge 2

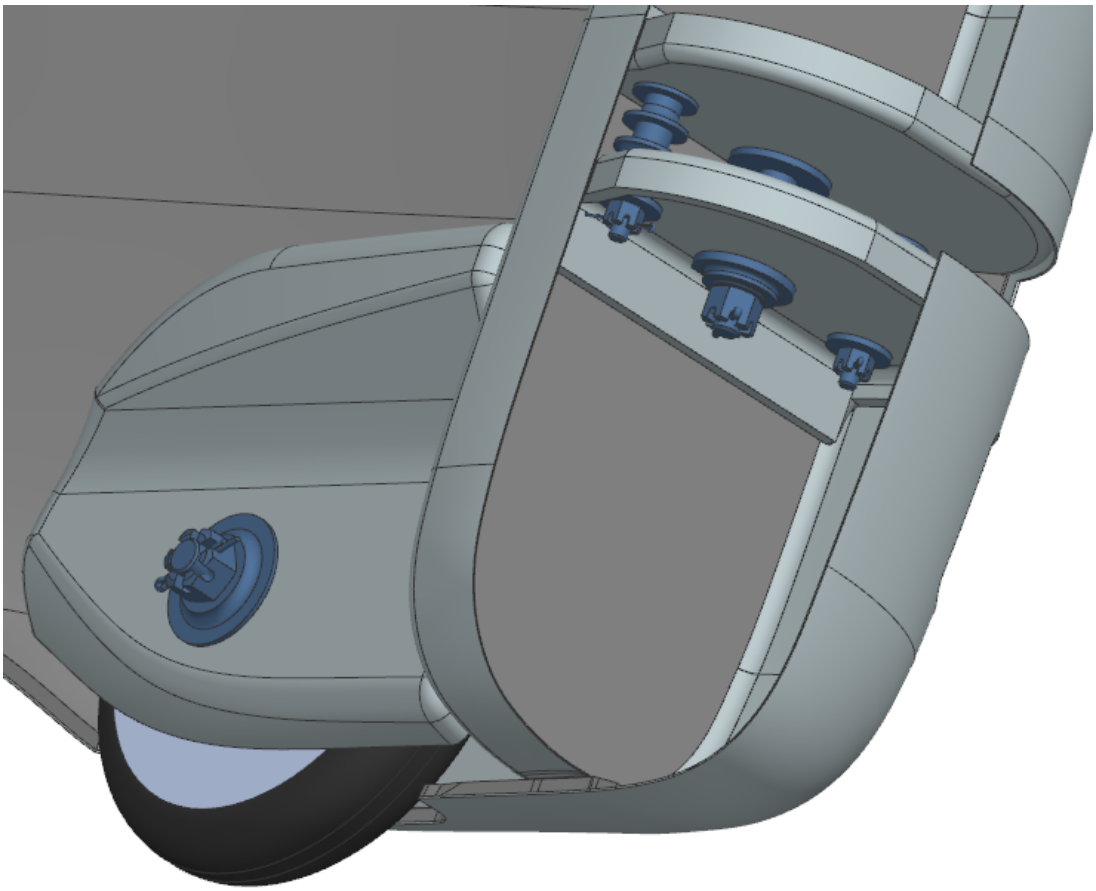

Figure 83: Detail of hinge 1 and tail wheel attachment

9 Production Process and Technology

In this section, a run-through of the production process is presented. The process begins with the manufacturing of composite parts and the machining of steel components, followed by the adhesive joining of the inner structure's parts. Subsequently, the rudder's structure is enclosed with the second half of the skin and cured. Finally, the rudder is removed from the mold, and the necessary openings are cut into the skin.

9.1 Composite Parts' Fabrication

All composite parts will be manufactured by vacuum bag molding using female molds. Renshape® Epoxy BM 5050 block material is ideal for the molds when assuming only one piece or a very small series of the rudders will be produced. It is easily machinable, thermally stable up to 110°C, has a low thermal expansion coefficient, and a fine surface structure. [51] The mold surface must be polished and a release agent must be applied before layup. Exact layups are not given for the parts as they are given in Table 21

9.1.1 Skin's Fabrication

The skin is divided into two parts along the plane of symmetry, with each part made in a separate mold. The mold for one of the parts will need to have a detachable section to create a lap joint surface, ensuring a reliable bond when the two halves are joined together later. A layer of gelcoat or car lacquer must be applied to the mold, which has been treated with a release agent, to form a UV protective layer for the carbon fiber skin. Gelcoat is easier to apply but has a relatively high areal weight of around 200 g/m^2 [52], whereas a thin layer of car lacquer can achieve approximately 50 g/m^2, although its application is more labor-intensive.

After applying the protective layer, the layup of the carbon fiber fabric can begin. The fabric is pre-cut and layered into the mold, with careful attention to laying the fabric at a 45° angle from a reference direction (the rudder's vertical axis, shown in Figure 84 along with the first ply). A ply covering the entire skin surface is laid first, followed by a second reinforcing layer in the lower part of the skin (highlighted in orange in Figure 85). The fabric must be impregnated with a proper amount of carefully mixed resin, accounting for an additional 150 g/m^2 needed for proper foam core bonding.

The 3 mm thick Rohacell foam core must be cut to the correct size, thermoformed to conform to the skin's shape, and its edges must be chamfered to limit a step in stiffness. The core is depicted in Figure 86 in a darker shade of gray. Next, the core is covered by the fabric plies, which are laid in reverse order, with the smaller reinforcing ply laid first, followed by the resin impregnation.

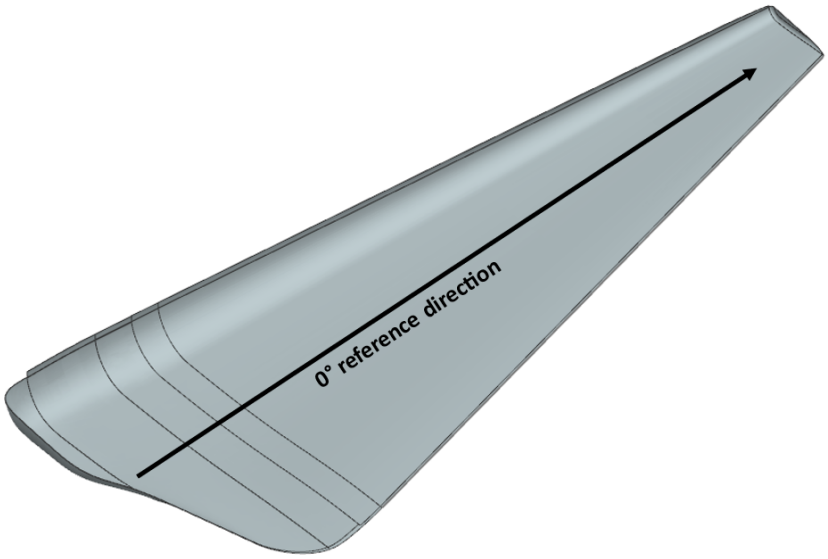

Figure 84: Skin's first ply and reference direction

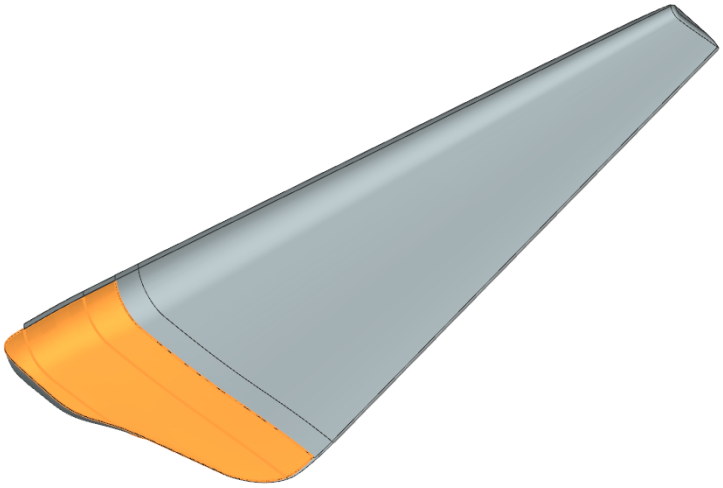

Figure 85: Second skin ply

The layup is then covered with a peel ply, porous release film, and bleeder fabric. A vacuum bag covers all these layers and is sealed to the mold body. Pressure on the molded part is created by pumping the air out of the bag through a valve. This pressure ensures the resin distributes evenly throughout the part, removes air bubbles from within the plies, and allows excess resin to soak into the bleeder fabric. This part of the process is the same for all carbon fiber components and will not be described for other parts. All parts should also be cured at room temperature for at least 24 hours. The assembled rudder will undergo post-curing, which is mentioned later on.

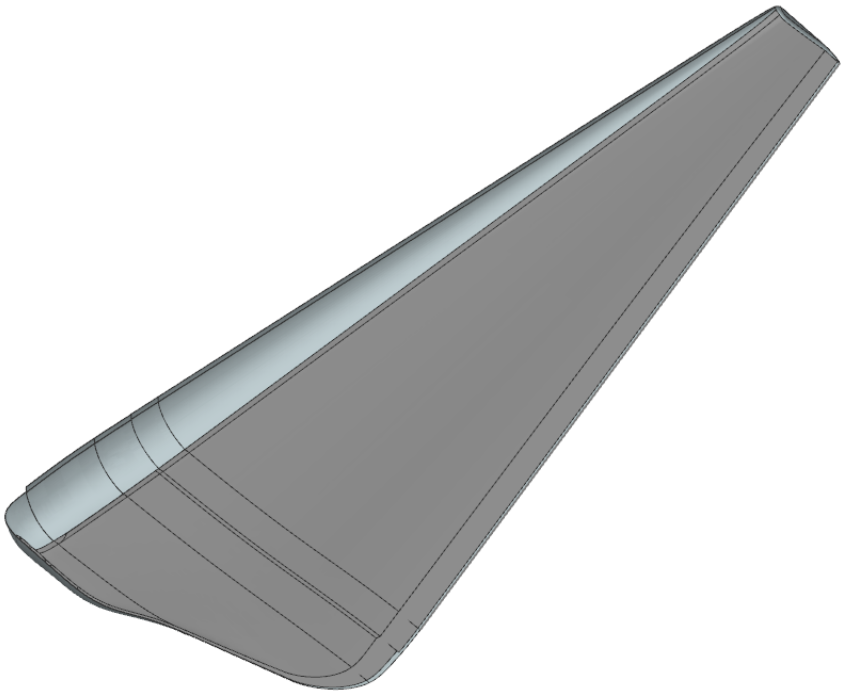

Figure 86: Skin with foam core

9.1.2 Spar's Fabrication

The layup process for the spar is essentially identical to that for the skin, except for the UV protective layer and peel ply between the mold and laminate. The protective layer is not necessary as the spar is not directly subjected to sunlight and the additional peel ply is necessary to create a rough surface needed for a strong bonded connection with the skin. The spar is made up of two carbon fiber fabric plies at a 45° angle from a reference direction and a 3 mm core between them. The spar is visualized in Figure 87 with the reference direction. The darker part (spar's web) is the foam core.

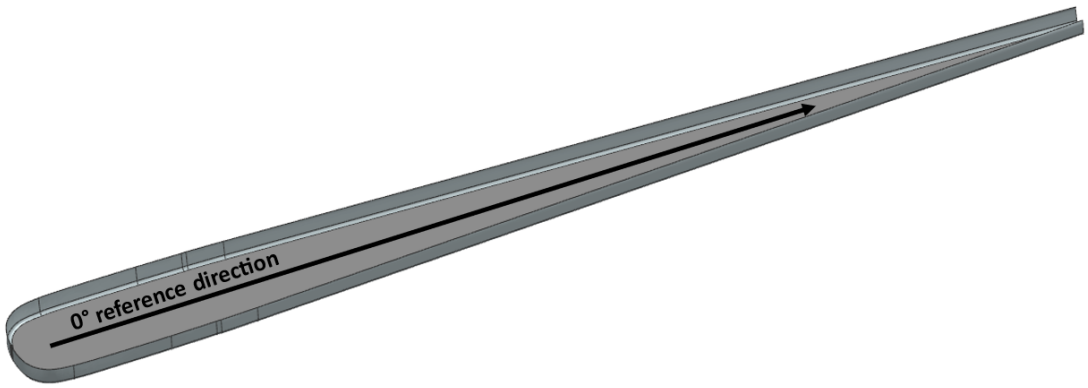

Figure 87: Spar

9.1.3 Ribs' Fabrication

Like the spar, ribs are not directly subjected to sunlight so UV protection is not necessary. Peel ply between the mold and the ribs' laminate is also required as they are bonded to the spar and skin. The ribs are not a sandwich structure, so there is no core. Two ribs of hinge 1 can be produced consecutively in the same mold as the cross sections of the rudder in the ribs locations are similar and production time is not a critical factor. This will result in slightly thicker bond lines between the ribs and the skin, but it decreases the manufacturing cost as production of only one mold is needed. The rib is shown in Figure 88 where the rib's web and back flange (where two additional unidirectional plies are used) are highlighted in orange.

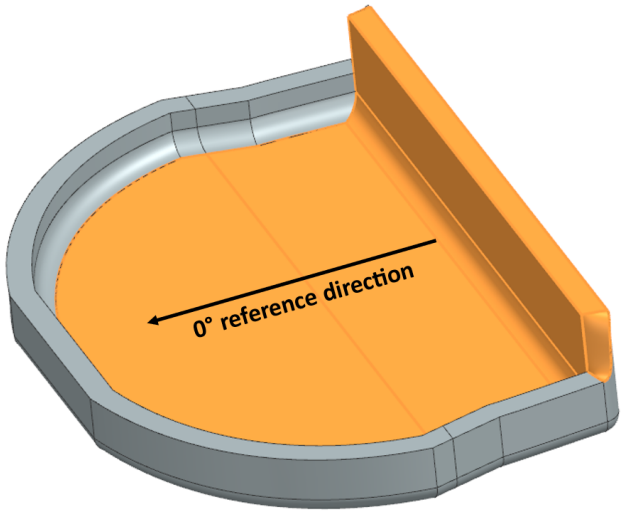

Figure 88: Hinge 1 rib

The angle between the web and flange of the hinge 2 rib (Figure 89) should ideally be acute to match the shape of the skin. This would require a two-part mold, as the rib could not be extracted from a one-part mold. Due to the small size of the rib (33 mm), it was decided to make the flange perpendicular to the web (or at a slightly obtuse angle to facilitate mold extraction) at the cost of a thicker bond line, to allow for the use of a single-part mold.

9.1.4 Wheel Attachment's Fabrication

Once again, the UV protective layer is not necessary to be applied to the tail wheel attachment, and a peel ply between the mold and the laminate is required. Opposed to the hinge 2 rib two-part mold is needed for the attachment, the split plane is visualized in Figure 90. The layup is different on the sides of the attachment that transfer the loads from the tail wheel and the wheel well, which only prevents debris from entering inside the ruder. The reference directions for both parts are shown in Figure 91 and the ply sequence is in Table 21. The outer plies and the middle ply are the same for both the sides and the wheel well, allowing

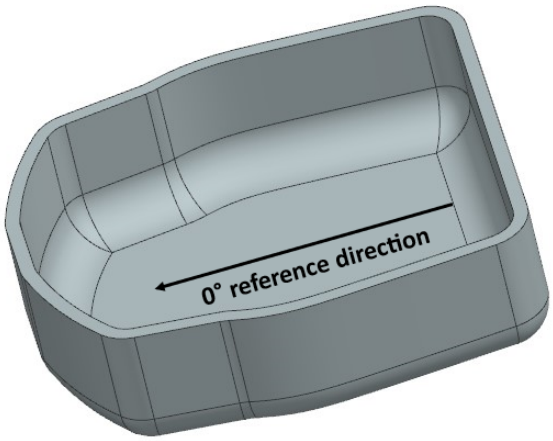

Figure 89: Hinge 2 rib

these plies to be continuous and avoid external ply drops that could cause delamination. The additional plies of the attachment sides should overlap with the wheel well to ensure there are no ply drops in the more heavily loaded areas.

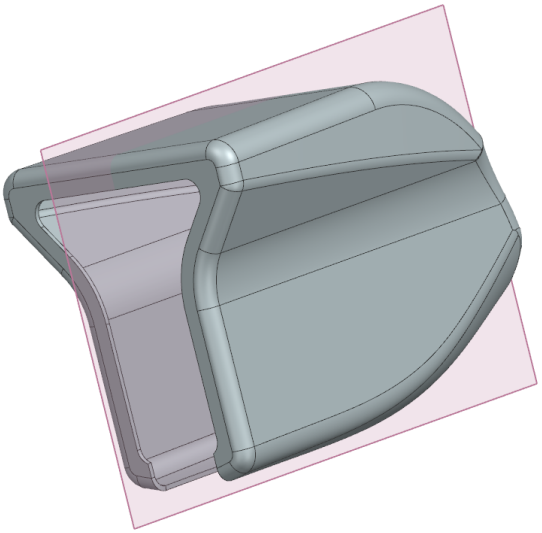

Figure 90: Splitting plane of attachment mold

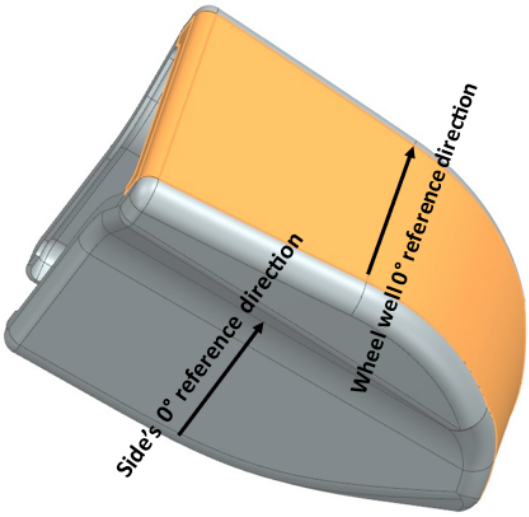

Figure 91: Attachment's reference directions

9.2 Rudder's Assembly

To prepare the parts for assembly holes for metal inserts must be drilled into the ribs and wheel attachment. The diameter of those holes should be about 1 mm larger than the diameter of the corresponding insert. This clearance is necessary as a thin ply of glass fiber fabric must be used in and around holes to separate the metal inserts from the carbon fiber to prevent galvanic corrosion and to allow for the inserts' alignment. The glass fiber fabric's surface must be roughened after cure to provide good bonding adhesion. The metal parts must be machined and the surfaces that will be bonded must also be roughened and degreased.

Both halves of the skin are kept in molds throughout the assembly process. The long handling time of the Permabond adhesive allows for more complicated assembly procedures without the risk of its hardening. Because the spar's flange is oriented forward, it would be impossible to first bond the spar to the skin a then bond the ribs afterward. The process of bonding the spar and ribs to half of the skin is as follows, a step-by-step explanation used for clarity:

1. Check if the two parts of the skin can be closed together when the spar and ribs are fitted
2. Apply adhesive to the metal inserts and washers for the ribs and pin of hinge 2
3. Put the metal parts together with the ribs, slightly torque the threaded inserts and washers so they stay together but can move freely in the hole
4. Apply adhesive to surfaces of spar and ribs to be bonded to the skin
5. Put the spar and ribs in the correct position on the skin
6. Use jigs to ensure the correct position of the parts and concentricity of bolt holes
7. Torque the threaded inserts and washers to 22 Nm
8. Check if a sufficient amount of adhesive is used, fill eventual voids

The jigs mentioned in the list must be designed specifically for the rudder and will be attached to the mold. Their job is to delimit the correct position of parts needed for the rudder's assembly and subsequent connection to the vertical stabilizer and control cables.

Once all the mentioned steps are completed, the tail wheel attachment can be glued to the spar and skin. The assembly steps are similar to those for bonding the ribs and spar, but the threaded inserts and washers must be torqued before bonding the attachment to the spar and skin, as they are not accessible later. The torquing must be done when the attachment is already fastened to a jig. Figure 92 shows the ribs, spar, and attachment bonded to the skin.

Assuming the bonding is done at 23°C, the jigs can be removed after 24 hours when the adhesive reaches its working strength. [46] When the jigs and the detachable section to create a lap joint surface are removed from the mold, it can be again tested if the two parts of the skin fit together. Afterward, the Permabond ET5429 epoxy glue is applied to the contact surfaces of the ribs, spar, attachment, and skin which will be in contact with the second part of the skin. The rudder is then closed by the second half of the skin. The two parts of the skin mold must be aligned perfectly and no shift between the two parts during cure must be ensured. This can be done by one part of the mold having protruding alignment pins and the other part having holes for these pins. The molds also have to be pressed together to ensure the bond quality.

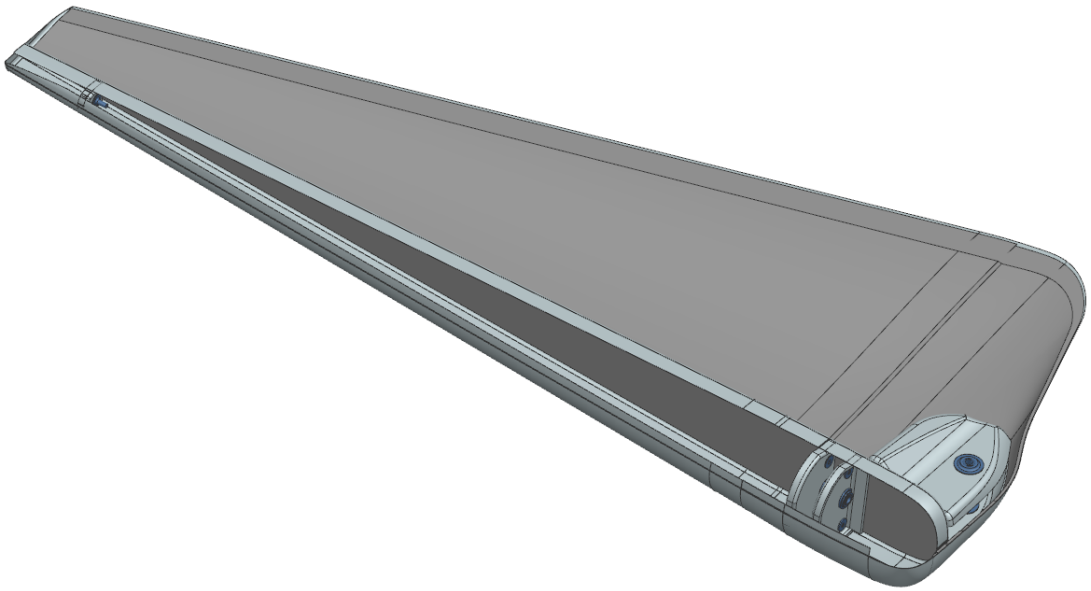

Figure 92: Rudder's inner structure bonded to skin

To achieve the desired mechanical properties of the composite, the rudder enclosed in the molds should be cured at 60°C for at least 15 hours. When the molds cool down after the cure, the rudder can be extracted from the mold. Openings must be cut into the skin to allow for connection to the vertical stabilizer, control cables, and the mounting of the tail wheel. Some of these openings are cut into the sandwich parts of the rudder. The periphery of these openings must be covered with thickened epoxy to ensure humidity does not reach the foam core. The completed rudder is shown in Figure 93.

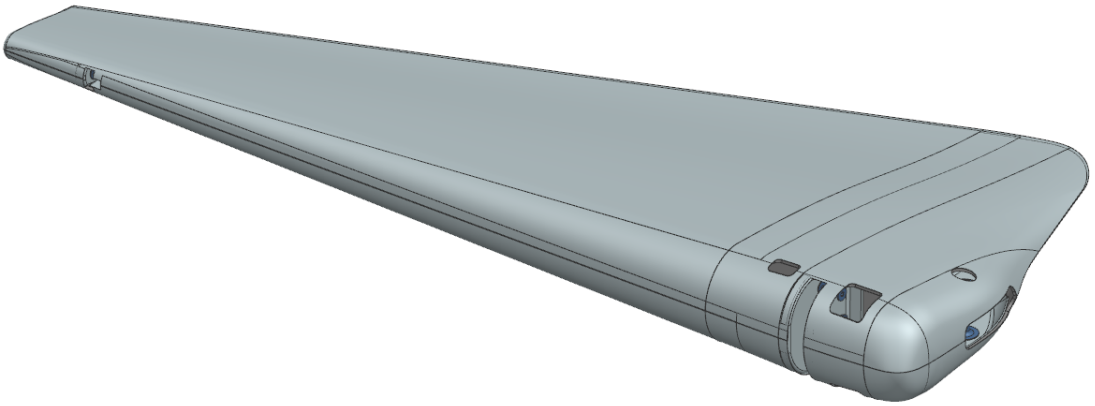

Figure 93: Completed rudder without detachable parts

10 Mass analysis

Mass analysis is performed in this section to determine the expected mass of the rudder. The tail wheel and all connecting components, except for the bearings, are included in the analysis. The mass of all the components is presented in Table 22. The mass of the adhesive is calculated based on the designed bond line thicknesses, which vary between 0.2 and 0.5 mm throughout the parts. It is likely that more adhesive than calculated will be used, but the exact amount is difficult to predict. The total rudder mass should be around 1.5 kg, however, the real weight will largely depend on the manufacturing quality.

Component	**Quantity**	**Unit mass [g/unit]**	**Mass [g]**
Skin	1 pc	686.5	686.5
Spar	1 pc	88.2	88.2
Hinge 1 rib	2 pcs	49.6	99.2
Hinge 2 rib	1 pc	2.4	2.4
Tail wheel attachment	1 pc	85.1	85.1
Tail wheel	1 pc	220	220
Tail wheel screw	1 pc	33.4	33.4
Tail wheel attachment insert	2 pcs	15	30
Tail wheel attachment threaded washer	2 pcs	7.9	15.8
Main joint threaded insert	2 pcs	8.3	16.6
Main joint threaded washer	2 pcs	5.2	10.4
Control connection insert	4 pcs	1.6	6.4
Control connection washer	4 pcs	1.4	5.6
Control connection spacer 1	2 pcs	4.5	9
Control connection spacer 2	2 pcs	3.2	6.4
Hinge 2 pin	1 pc	4.3	4.3
Hinge 2 threaded washer	1 pc	2.1	2.1
DIN 9841-5-M4-30 12.9 shoulder screw	1 pc	7	7
DIN 9841-8-M6-35 12.9 shoulder screw	1 pc	19	19
DIN 935 M4 hexagon castle nut	2 pcs	1.1	2.2
DIN 935 M6 hexagon castle nut	1 pc	3.3	3.3
DIN 937 M8 low hexagon castle nut	1 pc	5.5	5.5
DIN 94 1x10 cotter pin	2 pc	0.1	0.2
DIN 94 1.6x14 cotter pin	1 pc	0.3	0.3
DIN 94 2x16 cotter pin	1 pcs	0.5	0.5
Permabond ET5429 adhesive	25.4 cm^3	1	25.4
Paint coating	0.842 m^2	50	42.1
		Total mass	**1426.9 g**

Table 22: Mass analysis

11 Conclusion

The structural design of the racing airplane's rudder is performed in this thesis. The thesis starts with an overview of composite materials, describing the properties of the most widely used fiber types, fiber architectures, and polymer matrices in the aerospace industry. The most common manufacturing processes of fiber-reinforced thermoset polymers are also discussed, followed by the definition of the most commonly used failure criteria. The Tsai-Hill criterion is chosen to be applied to unidirectional tapes, and the Tsai-Wu criterion is selected to be applied to fabric materials. These two criteria are easy to implement and provide good failure prediction.

The rudder's structure is designed for two manufacturing processes: the vacuum bag molding process using hand-wetted fibers and the bag molding process using prepreg sheets. The prepreg sheets have higher fiber volume content and a lower factor of safety may be used due to their consistent properties. However, both the material and the manufacturing process are more costly, have limited shelf life, and offer a limited range of reinforcements. The range of reinforcements for the hand-wetted process is much wider, although the maximum achievable fiber volume content is lower, and a considerably higher factor of safety must be used. Carbon fiber woven fabrics and unidirectional tape reinforcements, together with epoxy matrices, are used for both designs. Rohacell IG-F foam is used as a core material to ensure sufficient sandwich material for the skin and spar of the rudder. AISI 4140 steel is used for inserts and other metallic parts.

The rudder is subject to aerodynamic, ground, and control system loads. The maneuvering and gust load cases are considered from the aerodynamic loads, tail-down landing, obstruction load, and side load cases are considered from the ground loads. Additionally, the 125% of hinge moment and 90 daN force exerted by the pilot on each pedal cases are considered from the control loads. Subsequently, stress resultants for all the mentioned cases are calculated and they are used as an input for the classical laminate theory, which is explained in the thesis. Composite-specific equations are used for stability calculations, and wrinkling and crimping failure modes are considered for sandwich structures. A Python script was written to perform the calculations, and the lightest possible layups were designed for the skin and the spar. Hinges connecting the rudder to the vertical stabilizer and tail wheel attachment were also designed. The ribs, which are part of the hinges, and the tail wheel attachment include bolted joints, therefore additional checks for failure modes of composite bolted joints are performed.

It is decided to proceed only with the hand-wetted design, as the weight savings weren't significant enough to justify the added cost. Afterward, the designed layups are verified by finite element analysis. The surface model of the rudder is meshed with 2D linear thin shell elements, which are preferable for thin-walled structures to avoid shear locking and reduce

computational time. Static linear and linear buckling analyses are performed to verify both the strength and stability of the designed parts. The linear analyses are sufficient as small deformations are expected, the material properties are elastic, Hooke's law applies, and the external loads and constraints are not time-dependent. The layups of the ribs and the tail wheel attachment are slightly modified as the analytically designed ones would fail.

Subsequently, a run-through of the production process using vacuum bag molding technology is presented, where the manufacturing processes for all the components are briefly described. At the end of the thesis, a mass analysis is performed, determining that the rudder should weigh less than 1.5 kg, including the tail wheel.

The work on the rudder's design can be continued by performing tests of the used materials to verify their properties, and by testing the tail wheel as its load capacity is currently unknown. More detailed FEA analysis could also be conducted, including a comprehensive analysis of bolted and bonded joints. Once the stiffness of the neighboring structure and control cables is determined, an aeroelastic analysis should be performed, particularly considering the airplane's high design speed. Following this, the detailed design of molds and jigs can take place to ensure seamless manufacturing. After manufacturing, the rudder should undergo strength tests simulating all the load cases mentioned in the thesis.

References

[1] Jakub VALENTA. "Koncepční návrh rychlostního letounu". Czech Technical University in Prague, 2019. URL: https://dspace.cvut.cz/handle/10467/84757.

[2] *UL 2 – Část I. Požadavky letové způsobilosti SLZ, Ultralehké letouny řízené aerodynamicky*. Prague: Letecká amatérská asociace ČR, Mar. 2019.

[3] Jiří NĚMEC. "Návrh směrového kormidla malého sportovního letounu". Czech Technical University in Prague, 2020. URL: https://dspace.cvut.cz/handle/10467/90384.

[4] Jan PROCHÁZKA. "Návrh ocasních ploch rychlostního letounu". Czech Technical University in Prague, 2021. URL: https://dspace.cvut.cz/handle/10467/97024.

[5] P. K. MALLICK. *Processing of Polymer Matrix Composites*. Boca Raton: CRC Press, 2018. ISBN: 978-1-4665-7822-7.

[6] Bankim Chandra RAY, Rajesh Kumar PRUSTY and Dinesh Kumar RATHORE. *Fibrous Polymeric Composites. Environmental Degradation and Damage*. Boca Raton: CRC Press, 2018. ISBN: 978-1-4987-8401-6.

[7] P. K. MALLICK. *Fibre Reinforced Composites. Materials, Manufacturing, and Design*. 3rd ed. Boca Raton: CRC Press, 2008. ISBN: 978-0-8493-4205-9.

[8] Daniel STEFANIAK. "Industrial composite manufacturing". Lecture slides (Delft University of Technology). 2022.

[9] Bradley A NEWCOMB. "Processing, structure, and properties of carbon fibers". In: *Composites Part A: Applied Science and Manufacturing* 91 (2016), pp. 262–282. ISSN: 1359-835X.

[10] Alan A. BAKER. *Composite Materials for Aircraft Structures*. 2nd ed. Reston: AIAA, 2004.

[11] V ARUMUGAPRABU et al. *Polymer-Based Composites: Design, Manufacturing, and Applications*. Boca Raton: CRC Press, 2022. ISBN: 978-0-367-64791-9.

[12] Anthony Roland BUNSELL, Sébastien JOANNÈS and Alain THIONNET. *Fundamentals of fibre reinforced composite materials*. Boca Raton: CRC Press, 2021. ISBN: 978-0-367-02373-7.

[13] Senthilkumar KRISHNASAMY et al. *Sandwich Composites: Fabrication and Characterization*. Boca Raton: CRC Press, 2022. ISBN: 978-0-367-69732-7.

[14] Wenguang MA and Russell ELKIN. *Sandwich Structural Composites: Theory and Practice*. Boca Raton: CRC Press, 2021. ISBN: 978-0-367-44172-2.

[15] Sohel RANA and Raul FANGUEIRO. *Advanced composite materials for aerospace engineering: processing, properties and applications*. Woodhead Publishing, 2016. ISBN: 978-0-08-100054-0.

[16] Christos KASSAPOGLOU. *Design and analysis of composite structures: with applications to aerospace structures*. 2nd ed. Chichester: John Wiley & Sons, 2013. ISBN: 978-1-118-40160-6.

[17] *PVDF ACP Sheet Exterior Wall Sandwich Panel Price Aluminum Composite Panel*. Qinhuangdao Taiwen Building Materials Co., Ltd. URL: https://www.taiwenbuilding.com/showroom/pvdf-acp-sheet-exterior-wall-sandwich-panel-price-aluminum-composite-panel.html (visited on 18/02/2024).

[18] Julie TEUWEN et al. "Polymer composite manufacturing". Lecture slides (Delft University of Technology). 2022.

[19] *Cadfil® - Filament Winding Software Technology. The Filament Winding Process*. Crescent Consultants Ltd. URL: https://www.cadfil.com/filamentwindingprocess.html (visited on 22/02/2024).

[20] Alessandro AIROLDI. "Structural analysis of aerospace vehicles". Lecture slides (Politecnico di Milano). 2023.

[21] *Component Prepreg*. Easy Composites Ltd. URL: https://www.easycomposites.eu/component-prepreg (visited on 03/03/2024).

[22] *XC130 Autoclave Cure Component Prepreg System. Technical Datasheet*. Easy Composites Ltd. URL: https://media.easycomposites.eu/datasheets/EC-TDS-XPREG-XC130-Component-Prepreg.pdf (visited on 03/03/2024).

[23] R.E. LAVENGOOD and Michael J. MICHNO. *Composite Shear Strength: Tube Torsion Vs Short Beam Shear*. Monsanto Research Corporation, 1973. URL: https://apps.dtic.mil/sti/tr/pdf/AD0770596.pdf (visited on 03/03/2024).

[24] Vojtěch MALÝ. "Dimenzování trupu letounu UL-39". Czech Technical University in Prague, 2018. URL: https://dspace.cvut.cz/handle/10467/80094.

[25] Michael R. WISNOM and M.I. JONES. "A Comparison between interlaminar and in-plane shear strength of unidirectional glass fibre-epoxy". In: *Advanced Composites Letters* 3.2 (1994). URL: https://journals.sagepub.com/doi/pdf/10.1177/096369359400300205 (visited on 03/03/2024).

[26] *ESHOP*. Havel Composites. URL: https://www.havel-composites.com/cs/kategorie/ (visited on 06/03/2024).

[27] Friedrich HÖRSCH Ing. "Gewebe aus Aramid- und Kohlefasern, deren Eigenschaften im Verbundwerkstoff und Anwendung" (Interglas Textil GmbH).

[28] *EPIKOTE™ Resin MGS® LR285, EPIKURE™ Curing Agent MGS® LH285-287. Technical Information*. Momentive Specialty Chemicals. URL: https://www.havel-composites.com/uploads/files/products/7/7ffa24e1b8dd6d125df91520e23ca92918e3a1c9.pdf (visited on 10/03/2024).

[29] *ROHACELL® IG-F. Product Information*. Evonik Industries AG. URL: https://products.evonik.com/assets/35/34/ROHACELL_IG_F_2022_April_EN_243534.pdf (visited on 03/03/2024).

[30] *AISI 4140 Chrome-Molybdenum High Tensile Steel*. AZoNetwork UK Ltd. URL: https://www.azom.com/article.aspx?ArticleID=6116 (visited on 23/04/2024).

[31] *Přehled vlastností oceli 42CrMo4*. Bohdan Bolzano, s.r.o. URL: https://bbolzano.cz/cz/technicka-podpora/technicka-prirucka/tycove-oceli-uhlikove-konstrukcni-a-legovane/oceli-k-zuslechtovani-podle-en-10083-1/prehled-vlastnosti-oceli-42crmo4 (visited on 23/04/2024).

[32] *42CrMo4. Material data sheet*. Ovako AB. URL: https://steelnavigator.ovako.com/steel-grades/42crmo4/ (visited on 24/04/2024).

[33] Filip TOMÁŠ. "Návrh křídla rychlostního letounu". Czech Technical University in Prague, 2020. URL: https://dspace.cvut.cz/handle/10467/96313.

[34] Ira H ABBOT, Albert E. VON DOENHOFF and Louis S. Jr. STIVERS. *NACA Report No. 824 Summary of Airfoil Data*. 1945. URL: https://engineering.purdue.edu/~aerodyn/AAE514/Spring%202011/naca-report-824.pdf (visited on 18/01/2024).

[35] Snorri GUDMUNDSSON. *General Aviation Aircraft Design: Applied methods and procedures*. Oxford: Butterworth-Heinemann, 2020. ISBN: 978-0-12-818465-3.

[36] Richard ŠIROKÝ. "Návrh přistávacího zařízení rychlostního letounu". Czech Technical University in Prague, 2022. URL: https://dspace.cvut.cz/handle/10467/99281.

[37] European Aviation Safety Agency. *Easy Access Rules for Very Light Aeroplanes. (CS-VLA) (Amendment 1)*. Nov. 2018.

[38] Daniel VYSOCKÝ. "Návrh primárního řízení sportovního letounu". Czech Technical University in Prague, 2021. URL: https://dspace.cvut.cz/handle/10467/96039.

[39] Jaromír ŠPUNDA. *Pevnost leteckých konstrukcí: Nosná soustava - křídla letounů*. Vojenská akademie Antonína Zápotockého, 1955.

[40] Christos KASSAPOGLOU. "Design and Analysis of Composite Structures II". Lecture slides (Delft University of Technology). 2022.

[41] *PCMF 081005.5 E. PTFE composite flanged bushing*. AB SKF. URL: https://www.skf.com/group/products/plain-bearings/bushings-thrust-washers-strips/bushings/productid-PCMF%20081005.5%20E (visited on 24/04/2024).

[42] *ISO 7379. Lícované šrouby*. ELESA+GANTER CZ S.R.O. URL: https://www.elesa-ganter.cz/cs/cze/Strojni-prvky--Licovane-%C5%A1rouby--ISO7379?gad_source=1&gclid=Cj0KCQjwiYOxBhC5ARIsAIvdH52BCxJBfWSQIzP4wN9If19Y2yLUM_qahinIxbNlQT3eUIRXBFDs71QaAoEQEALw_wcB&err=second (visited on 24/04/2024).

[43] T.A. COLLINGS. *The Strength of Bolted Joints in Multi-Directional CFRP Laminates. C.P. No. 1380*. Aeronautical Research Council, Ministry of Defence, 1977.

[44] MIL-HDBK-5J. *Metallic materials and elements for aerospace vehicle structures*. Department of Defense Washington, DC, 2003.

[45] Christos C. CHAMIS. "Simplified Procedures for Designing Composite Bolted Joints. NASA Technical Memorandum 100281". In: 43rd Annual Conference of the Society of the Plastics Industry (Cincinnati, Ohio, 1st–5th Feb. 1988). Cleveland, Ohio: Lewis Research Center, 1988.

[46] *PERMABOND® ET5429. Two-Part Epoxy Technical Datasheet*. Permabond Engineering Adhesives Ltd. URL: https://media.easycomposites.co.uk/datasheets/ET5429_TDS.pdf (visited on 16/05/2024).

[47] *GE 5 E. Radial spherical plain bearing, requiring maintenance, metric sizes*. AB SKF. URL: https://www.skf.com/group/products/plain-bearings/spherical-plain-bearings-rod-ends/radial/productid-GE%205%20E (visited on 29/04/2024).

[48] *Root Air Black Pro Scooter Wheels 2-pack 110mm - Red*. Spineo.cz. URL: https://spineo.cz/root-air-black-pro-scooter-wheels-2-pack-110mm?barva=18476 (visited on 30/04/2024).

[49] Dominique MADIER. *Practical Finite Element Analysis for Mechanical Engineers*. Canada: FEA Academy, 2020. ISBN: 978-1-9990475-2-8.

[50] Kirill GUSEINOV et al. "Determination of interlaminar shear properties of fibre-reinforced composites under biaxial loading: A new experimental approach". In: *Polymers* 14.13 (2022).

[51] *RenShape® BM 5050. Technical Data Sheet*. OBO-Werke GmbH. URL: https://skolil.cz/images/stories/RenShape_BM_5050_technical_data.pdf (visited on 18/05/2024).

[52] *Vorgelat T30 / T35 / T35SH MGS (HEXION) polyesterové gelcoaty. Technický list, instrukce k použití*. Havel Composites. URL: https://www.havel-composites.com/uploads/files/products/3051/d1a6785a3fd90bdbc5503a789d9abaf858906ab5.pdf (visited on 18/05/2024).